In compliance with the
Canadian Privacy Legislation
some supporting forms
may have been removed from
this dissertation.

While these forms may be included
in the document page count,
their removal does not represent
any loss of content from the dissertation.

University of Alberta

Realistic Head Volume Conductor Modeling for EEG Source Localization

by

Lora A. Neilson

A thesis submitted to the Faculty of Graduate Studies and Research in partial fulfillment
of the
requirements for the degree of Master of Science

Department of Electrical and Computer Engineering
Department of Biomedical Engineering

Edmonton, Alberta
Fall 2003

National Library of Canada
Acquisitions and Bibliographic Services
395 Wellington Street
Ottawa ON K1A 0N4
Canada

Bibliothèque nationale du Canada
Acquisisitons et services bibliographiques
395, rue Wellington
Ottawa ON K1A 0N4
Canada

Your file Votre référence
ISBN: 0-612-87848-1
Our file Notre référence
ISBN: 0-612-87848-1

The author has granted a non-exclusive licence allowing the National Library of Canada to reproduce, loan, distribute or sell copies of this thesis in microform, paper or electronic formats.

The author retains ownership of the copyright in this thesis. Neither the thesis nor substantial extracts from it may be printed or otherwise reproduced without the author's permission.

L'auteur a accordé une licence non exclusive permettant à la Bibliothèque nationale du Canada de reproduire, prêter, distribuer ou vendre des copies de cette thèse sous la forme de microfiche/film, de reproduction sur papier ou sur format électronique.

L'auteur conserve la propriété du droit d'auteur qui protège cette thèse. Ni la thèse ni des extraits substantiels de celle-ci ne doivent être imprimés ou aturement reproduits sans son autorisation.

Canada

University of Alberta

Library Release Form

Name of Author: Lora A. Neilson

Title of Thesis: Realistic Head Volume Conductor Modeling for EEG Source Localization

Degree: Master of Science

Year this Degree Granted: 2003

Permission is hereby granted to the University of Alberta Library to reproduce single copies of this thesis and to lend or sell such copies for private, scholarly or scientific research purposes only.

The author reserves all other publication and other rights in association with the copyright in the thesis, and except as herein before provided, neither the thesis nor any substantial portion thereof may be printed or otherwise reproduced in any material form whatever without the author's prior written permission.

August 28, 2003

University of Alberta

Faculty of Graduate Studies and Research

The undersigned certify that they have read, and recommend to the Faculty of Graduate Studies and Research for acceptance, a thesis entitled "Realistic Head Volume Conductor Modeling for EEG Source Localization" submitted by Lora A. Neilson in partial fulfillment of the requirements for the degree of Master of Science.

Dr. Z. J. Koles

Dr. C. Beaulieu

Dr. K. E. Jones

Dr. A. M. Knight

August 28, 2003
Date approved by committee

Abstract

An accurate computer model of realistic biological volume conductors has been developed using the Finite Volume Method for solution of the forward problem in EEG. Based on simulated scalp potentials calculated by a "gold-standard" analytic equation, single dipole current sources localized within a numerical three-shelled spherical model verify the accuracy of the method. Further experiments performed on a very high resolution numerical head model of realistic geometry demonstrate that this modeling technique is an excellent candidate for use in clinical EEG source localization. The Finite Volume Method has been expanded to incorporate generalized tissue anisotropy and exhibits excellent agreement with a known analytic solution to Laplace's equation. A realistic head model including anisotropic conductivity, created using quantitative tensor data, is compared to isotropic versions of the same head model through single dipole estimation experiments. An integrated algorithm that combines polynomial preconditioning with the Conjugate Gradient Method makes it possible to solve the large sparse linear systems of equations in a reasonable amount of time for clinical application. Optimization of polynomial preconditioning input parameters has been explored in detail.

Preface

This thesis is a collection of three studies related to numerical modeling of the conductive properties of realistic head volumes using the Finite Volume Method. The results of these works were originally documented in separate, as yet unpublished papers and are contained herein as three distinct chapters. Chapter 1 focuses on the basics of the Finite Volume Method, its verification against an analytic equation, and its application to EEG source localization by lead field analysis. Chapter 2 details an expansion of the Finite Volume Method to incorporate tissues of generalized anisotropic conductivity, its verification, and an assessment of the utility of that method. Chapter 3 is an in-depth examination of an efficient iterative method for solving the systems of linear equations that arise from the Finite Volume Method – the Conjugate Gradient Method with preconditioning by Chebyshev polynomials. Each segment contains its own list of references, including referrals to other chapters within this thesis.

Acknowledgements

I would like to gratefully acknowledge the enthusiastic supervision of Dr. Zoltan Koles throughout this work. My appreciation is also extended to Dan Withey and Nora O'Neill for technical and moral support, as well as Mustafa Hirji and Michael Cook for their meticulous labour in translating the polynomial preconditioned Conjugate Gradient solver program into C. I thank Dr. Christian Beaulieu and Yusuf Bhagat for acquisition and interpretation of the diffusion tensor MR data used in my study of anisotropic volume conductor modeling.

I appreciate my family, Andrea, Celina, Jesse, Roy, Hollie, Mom, Dad, and little Curtis for putting up with my intermittent crankiness and for their exuberant recognition of my periodic success throughout my years of studentship.

Finally, I express my everlasting gratitude to Danny Major who has nurtured my fondness of learning through intellectual stimulation and who continually shows me, by example, how to strive for excellence in all endeavours.

This research was supported by the Natural Sciences and Engineering Research Council of Canada (NSERC) and by the Alberta Informatics Circle of Research Excellence (ICORE).

Table of Contents

INTRODUCTION 1

CHAPTER 1 - FINITE VOLUME HEAD MODEL 3

I. Introduction 3

A. Motivation 3

B. Equivalent Dipole Source Model 4

C. Current Density Distribution 5

D. Analytical Conductor Models 5

E. Boundary Element Method 6

F. Finite Element Method 7

II. Methods 8

A. Finite Volume Method 8

B. Lead Field Analysis Using Reciprocity 10

C. Verification of the Model 11

D. Realistic Head Geometry 12

E. Model Preparation 13

1) Finite Volume Decomposition 13

2) Finite Difference System of Equations 14

F. Solving the Forward Problem 16

1) The Conjugate Gradient Method 16

2) Matrix Deflation 17

3) Preconditioning 18

G. The Inverse Problem 21

1) Localization Method 21

2) Collection of Lead Field Data 23

H. Verification 26

1) Source Localization Accuracy 26

2) Error Measurements 28

3) Importance of Realistic Head Geometry 29

III. Results 31

A. 3-Shelled Sphere 31

B. Realistic Head Geometry 37

IV. Analysis of Results 40

V. Future Directions 42

References 44

CHAPTER 2 - ANISOTROPIC EXPANSION OF THE FINITE VOLUME METHOD AND QUANTITIFYING TISSUE CONDUCTIVITIES BY DIFFUSION TENSOR IMAGING.....49

I. Introduction 49

A. EEG Source Localization 49

B. The Finite Volume Method 50

C. Anisotropic Conductivity 55

II. Methods 58

A. Development of the Expanded Finite Volume Method 58

B. Volume Decomposition Algorithm 81

C. Reciprocity and the Lead Field Matrix 82

D. Solving the Forward Problem 83

1) The Conjugate Gradient Method 83

2) Preconditioning 85

E. Verification Experiments 86

1) Comparison to Analytical Solution 86

2) Realistic Model Comparison 87

a) Lead Field Calculations 90

b) Simulated EEG 91

c) Dipole Localization 92

III. Results 93

A. Forward Solution Details 93

B. Verification Experiments 95

1) Comparison to Analytical Solution 95

2) Realistic Model Comparison 96

a) Lead Field Calculations 96

b) Simulated EEG 97

c) Dipole Localization 98

IV. Discussion 101

V. Conclusions 103

References 104

Appendix A: Positive Semidefiniteness of the EFVM Coefficient Matrix 107

Appendix B: Vectorized EFVM Decomposition Algorithm Flowchart 122

CHAPTER 3 - ACCELERATED FORWARD SOLUTION BY CHEBYSHEV POLYNOMIAL PRECONDITIONING 129

I. Introduction 129

A. Volume Conductor Models 129

B. Source Models 130

C. Finite Volume Method 130

II. Methods 131

A. Model Preparation 131

B. Solving the Linear System 133

1) The Conjugate Gradient Method 133

2) Matrix Deflation 135

3) Preconditioning 136

a) Jacobi Preconditioning 137

b) Polynomial Preconditioning with Chebyshev Polynomials 138

C. Timing and Optimization Experiments 140

1) Polynomial Degree 142

2) Spectral Bound Parameters 143

3) To Deflate or Not to Deflate 143

III. Results 144

A. Jacobi Preconditioning 144

B. Polynomial Preconditioning 145

1) Polynomial Degree 145

2) Spectral Bound Parameters 147

3) To Deflate or Not to Deflate 148

IV. Discussion 151

V. Conclusions 152

References 154

SUMMARY 157

List of Tables

CHAPTER 1

1-1 24-LEAD ELECTRODE MONTAGE 28

1-2 LOCALIZATION ERRORS FOR EACH TEST DIPOLE 34

1-3 SCALP POTENTIAL ERROR NORMS FOR EACH TEST DIPOLE 37

1-4 DISPLACEMENT ERRORS OF ESTIMATED DIPOLES IN THE REALISTIC HEAD MODEL 38

CHAPTER 2

2-1 CHARACTERISTIC CONDUCTIVITIES 89

2-2 ERROR NORMS OF ISOTROPIC ELECTRODE POTENTIAL VECTORS 98

2-3 DIPOLE LOCALIZATION ERRORS 99

List of Figures

CHAPTER 1

1-1 A set of adjacent voxels modeled as nodes in a 3D mesh circuit 13

1-2 A visual depiction of the finite difference system of equations 16

1-3 Vectorized Finite Volume decomposition algorithm flowchart 20

1-4 A visual description of the LFM 21

1-5 Linear network reciprocity illustrated 24

1-6 A visual description of a lead field matrix obtained by reciprocity 25

1-7 Estimation of radial dipoles in a 3-shelled sphere with 1.84 mm resolution 32

1-8 Estimation of tangential dipoles in a 3-shelled sphere with 1.84 mm resolution 32

1-9 Estimation of radial dipoles in a 3-shelled sphere with 0.92 mm resolution 33

1-10 Estimation of tangential dipoles in a 3-shelled sphere with 0.92 mm resolution 33

1-11 Example Goodness of Fit profile, $-\log(J_i)$, at eccentricity 0.6 radially oriented on the negative y axis (sagittal slice through centre of sphere in a 200^3 grid) 35

1-12 Example Goodness of Fit profile, $-\log(J_i)$, at eccentricity 0.8 tangentially oriented on the positive x axis (coronal slice through centre of sphere in a 200^3 grid) 36

1-13 Axial view of radial source localization in a realistic head model with 1.21 mm resolution (200^3 grid) 39

1-14 Coronal view of tangential source localization in a realistic head model with 1.21 mm resolution (200^3 grid) 39

1-15 Sagittal view of radial source localization in a realistic head model with 1.21 mm resolution (200^3 grid) 40

CHAPTER 2

2-1 Orthonormal cell face area vectors 52

2-2 Primary and secondary cell configuration 60

2-3 Two nodes and four internodes to calculate flux through a voxel face 64

2-4 Discrete potentials for calculating total source current inside a voxel 65

2-5 Four voxels and *xy* intervoxel 67

2-6 Nodes and internodes to calculate flux through an active intervoxel face 71

2-7 Flux through voxel discontinuity 73

2-8 Flux over intervoxel discontinuity 76

2-9 Intersection of orthogonal cell faces 80

2-10 Conductive anisotropy ellipses 90

2-11 Seven electrode leads and 24 cortical dipoles 92

2-12 Polynomial preconditioned CGM convergence statistics 95

2-13 Error measures of EFVM versus analytical solution to Laplace's equation 96

2-14 Isopotential contours and lines of current flow from lead 3 97

2-15 Dipole localization results 100

2-A1 System of potential variable relative indexing used for voxel equations 108

2-A2 System of potential variable relative indexing used for intervoxel equations 110

2-A3 Face 2 of voxel *i* (shaded vertical) intersects with face 4 of *xy* intervoxel *j* 112

2-A4 Face 4 of *xy* intervoxel *i* (shaded vertical) intersects with face 6 of *xz* intervoxel *j* 113

2-A5 An *xy* voxel plane 118

CHAPTER 3

3-1 A set of adjacent voxels modeled as nodes in a 3D mesh circuit 132

3-2 A visual depiction of the finite difference system of equations 134

3-3 Total time for solution convergence for two head model sizes 146

3-4 Number of iterations and average time per iteration 147

3-5 Total time for solution convergence for deflated and undeflated systems 150

INTRODUCTION

Electroencephalographic (EEG) source localization is the process of identifying the spatial origin of particular electrical activity in the brain based on electrical field measurements recorded from a patient's scalp. This is also known as the inverse problem in EEG, whereas the forward problem constitutes the opposite procedure – calculation of the electric field induced on the patient's scalp by a known configuration of excited brain cells. Modeling conductive properties of the head volume can provide an answer to the forward problem, which is a prerequisite for solution of the underdetermined inverse problem. This research focuses on a numerical approach to modeling realistic head volumes for the purpose of EEG source localization.

Chapter 1 describes a numerical volume conductor model based on the Finite Volume Method (FVM), using lead field analysis to solve the inverse problem in EEG. The finite volume approach to the forward problem provides an estimation of the electric fields in the brain that is applicable to any type of EEG inverse solution with focal or distributed source configurations. To verify the modeling technique, single dipole localization experiments are performed on an inhomogeneous (3-shelled) spherical conductor model. Similar source estimation techniques are applied to a realistic FVM head model built from medical images of a human subject to confirm that head geometry has a significant effect on the accuracy of EEG source localization, and must be considered for practical application.

In Chapter 2, the FVM is expanded to incorporate generalized tissue anisotropy. Properties of the resulting system of equations are investigated in detail, and the newly developed Expanded Finite Volume Method (EFVM) is verified against a known analytic

solution to Laplace's equation. Diffusion weighted MRI is used to quantify diffusion tensors throughout the head. These measurements can be approximately linearly related to the conductivity tensor of each voxel in a patient-specific head model. In this way, a two-dimensional anisotropic conductor is modeled using diffusion tensor data acquired from a human subject. Two other isotropic conductor models of the same head are generated using tensor trace and tissue-type segmentation techniques. Simulated potentials from the scalp of the anisotropic head model are used to localize the dipole sources within the simplified isotropic versions. This is done in order to demonstrate the importance, with respect to EEG source localization, of accounting for tissue anisotropy in biological volume conductors.

In Chapter 3, a very high spatial resolution realistic FVM model of the human head is implemented to examine various computational aspects of solving of large, sparse linear systems of equations. Along with Jacobi preconditioning, an integrated algorithm that combines polynomial preconditioning with the Conjugate Gradient Method (CGM) is able to solve the forward problem in EEG in a reasonable amount of time, such that clinical application of the head modeling method is possible. Optimization of polynomial preconditioning input parameters is explored in detail for the high resolution head model, as well as for a model of lesser resolution, which yields a much smaller linear system of equations to be solved.

CHAPTER 1
FINITE VOLUME HEAD MODEL

I. Introduction

A. Motivation

EEG recordings are routinely obtained from patients who exhibit brain disorders such as epilepsy. The bioelectric signals measured by EEG are a result of coherent activation of pyramidal cells in the cortex. In focal epilepsy, seizures originate from abnormal electrical activity in a small region of brain tissue known as the epileptogenic focus [1], then propagate throughout the head. Surgeons would like to know the exact location of the source so that the aberrant tissue can be removed, and the patient cured. Presently, clinical EEG source localization is a hit and miss procedure. Often, the affected region of the brain is identified by a series of cognitive tests, along with functional and anatomical imaging. Sometimes depth electrodes are used to pinpoint the source of electrical disturbance. This intracranial recording technique is extremely invasive and ineffective in some cases. It is therefore important to investigate alternative solutions to the problem of EEG source localization.

In the past half century, much research has been done in the area of epileptic source localization via EEG. There are some inferential techniques that involve visual inspection of EEG time series or scalp voltage topography. These methods are widely used in clinical settings, but they provide only a rough indication of the nature of epileptic activity exhibited by a patient. Unquestionably there is a need for a more definitive approach to uncovering the valuable diagnostic information embedded in EEG data. Any such procedure necessarily requires the use of models to approximate both the source of electric brain potentials, and the conductive medium (the head) through which

the biological signal propagates. Various approaches to these modeling problems are described next.

B. Equivalent Dipole Source Model

There is a strong physiological argument to support the assertion that equivalent current dipoles can adequately approximate the electric field produced by a region of active cortical cells. It is well understood that scalp electrodes merely detect the *net* magnitude and orientation of electric fields generated by any group of excited neurons in the brain. In fact, there is substantial signal canceling amongst cells with opposite orientation (in the many folds of the cortical surface, for example). It is suggested, therefore, that modeling the source of this electric field with equivalent dipole(s) is entirely appropriate because the EEG field that would be simulated by the dipole is very similar to that produced by an aggregation of neurons extending over several square centimetres [2]. The three-dimensional location and moment of an equivalent dipole is indicative of the geometric centre and net orientation of the active cortical region, respectively. Admittedly, there is some ambiguity between source depth and strength when it comes to interpretation of the signal magnitude measured on the scalp [2], [3]. However, this confounding effect should be diminished by careful consideration of the dipole orientation and reconciling that with extensive knowledge of cell orientation in the cortical anatomy, thereby incorporating physiological constraints into the problem [4], [5].

Since complex combinations of cortical generators can emit overlapping signals that evolve over time, it may be necessary to develop more complicated source models to account for such cerebral activity. Spatiotemporal dipole source models have been

investigated to this end. In some cases, a single dipole is localized and then allowed to shift location and orientation with consecutive scalp potentials from the EEG time series. Alternatively, a superposition of several fixed dipoles are allowed to change in magnitude and polarity to account for the time-changing electric field measured on the scalp [1], [6]. In any case, an important feature of the equivalent dipole model is the ability to sum and evolve any distribution of single dipoles to represent a cortical source distribution of arbitrary complexity over a period of time. Furthermore, by principal component analysis spatiotemporal data can be exploited to null the effect of EEG background – uncorrelated noise – in single or multiple dipole source estimation algorithms [7]–[10].

C. Current Density Distribution

Alternatively to the equivalent dipole, neuronal activation in the finite volume head model can be described by volume currents, which vary in magnitude across all the voxels in the solution space. Such a representation of distributed activity is generally developed by a minimum norm solution, where the estimated current density profile throughout the solution space best accounts for instantaneous or spatiotemporal EEG data. The method is necessarily subject to domain constraints such maximal smoothness, where it assumed that the brain expends minimal energy to produce the measured EEG signal, as in LORETA [11]. Other a priori knowledge obtained from physiological constraints or functional imaging can also be incorporated to obtain a viable solution to the inverse problem [12], [13].

D. Analytical Conductor Models

The earliest and most simple head models developed for EEG source localization were analytically-derived spherical volume conductors. Some models of this type were

homogenous, but truer approximation of an actual head volume demands that some structure be accounted for through use of an inhomogeneous sphere consisting of three or four concentric or eccentric shells of differing resistivity (to represent the scalp, skull, brain and sometimes cerebrospinal fluid). These days, it is widely agreed that any spherical model is too simplistic to accurately locate epileptogenic foci [1], [14], [15]. Some work in fitting spherical surface potentials to a realistic head shape [16]–[19], or vice-versa [20] has been documented. These techniques are quite effective for localizing superficial sources, but less so for electrical activity originating deeper in the brain, where the shape of the skull deviates most dramatically from the ideal sphere.

Increased accessibility of efficient and affordable computing has borne a widespread pursuit of more realistic, numerical head models. These constructions are obviously subject to the inaccuracies of any discrete volume approximation (finite resolution, round-off error, etc.), but fortunately, analytical spherical models serve as a "gold standard" by which the performance of numerical volume conductor models may be assessed.

E. Boundary Element Method

The Boundary Element Method (BEM) [5], [14], [21], [22] is one approach to representing a realistically shaped volume conductor. Such a model specifies closed boundary surfaces between tissue regions to account for differing resistive properties in the head volume. The surfaces are described by an assemblage of triangular elements of limited spatial resolution, and potentials on any surface can be calculated given a known dipole source inside the volume. Through verification with analytical models it has been

shown that BEM models comprised of few (less than 5000) elements provide a reasonably accurate approximation of volume conduction effects [14], [21].

On the other hand, since the model is constructed from a combination of closed surfaces, tissue discontinuities, inhomogeneities, and anisotropy are not taken into account, leaving important features of the real head volume unresolved [23]. Furthermore, the formulation of equations that describe the boundary model are rather complicated requiring substantial integration of complex functions [24]. Therefore, the technique usually incorporates four or fewer surfaces per volume and offers only marginal improvement in realism over an eccentric spheres model. Results obtained by localizing implanted sources in a human head with a BEM model confirm that it is a weak approximation of realistic head volumes [14], [21].

F. Finite Element Method

The Finite Element Method (FEM) [4], [25] is an alternative numerical construction that can be used to represent realistic head volumes. Rather than specifying tissue interface surfaces, this technique models the entire volume with interconnected volume elements of various shapes and sizes. As such, this method accounts for many of the complexities omitted by the Boundary Element Method including tissue discontinuities, inhomogeneities, and anisotropy. It is therefore is a better model for EEG source localization [4]. Formulation of equations that describe the FEM are significantly less complicated than for the BEM, but setting up the optimal nonuniform volume grid can be a challenging task [4], [24].

II. Methods

A. Finite Volume Method

The Finite Volume Method (FVM) is a numerical technique used to model the current flow through an inhomogeneous medium by building a mathematical description of the volume as an assemblage of many equally sized discrete volume elements [24], [26]. Each hexahedron is assigned resistive properties based on those of the tissue it represents. Specifying one or more current sources anywhere in the model, the resulting resistive network is translated into a large, sparse system of finite difference equations and solved to determine potentials at each node. This method is based on general curvilinear coordinates. In the present work, cubic voxels are framed in an isotropic Cartesian grid.

Thus the volume decomposition and formulation of equations is conceptually and mathematically very simple [27], lending itself well to a robust, unsupervised algorithm for patient-specific head model development.

Since the voxels in this particular implementation of the FVM are strictly cubic, the discretized head model can be extracted directly from pixels of medical images. Furthermore, the computational complications of a nonuniform grid are avoided by using very high finite volume resolution throughout the head, rather than doing mesh refinement at critical tissue interfaces, as is sometimes necessary with the FEM. In this way, the FVM decomposition algorithm and processing is straightforward, unlike models based on irregularly shaped volume elements.

A FVM head model can account for the actual head shape and tissue discontinuities such as holes in the bone structure. This important flexibility offers maximal accuracy in source localization. Furthermore, this approach can easily accommodate anisotropic

tissue in the conductivity model of the head volume [23], [27]. This is vital requirement of any realistic head model since electrical conduction through some paths in the brain is highly restricted by the structured orientation white matter tracts, for example [28]. It has been shown that neglecting this effect introduces further errors in EEG source estimation [13], [29], [30].

Previous research on the use of finite differences (FVM and the similar Finite Difference Method) to solve the forward problem of EEG signal propagation can be found in [23], [27], and [31]–[33]. There is general agreement that the relative discrepancy between scalp potentials calculated by the FVM versus those from an analytical spherical model is reasonably low. Furthermore, correlation between the solutions from the two methods can be improved by increasing the spatial resolution of the three-dimensional finite volume grid. For spatial resolution of one millimeter, the head must be represented by millions of discrete volume elements. The large number of voxels that constitute a head model yield an enormous set of data to be algebraically manipulated. This leads to significant challenges in terms of computation time and memory requirements. Integration of polynomial preconditioning with the Conjugate Gradient Method algorithm provides the ability to solve these extremely large systems of equations in an acceptable amount of time. It is proposed here that the application of polynomial preconditioning will make it possible to solve much larger systems of finite difference equations so that the head model can be discretized into many more volume elements (better spatial resolution) than has been attempted in the past.

B. Lead Field Analysis Using Reciprocity

The concept of lead field analysis is central to the inverse problem. It allows for the patient-specific localization of any number of various source configurations in a relatively short time frame. Since potentials are measured only at particular places on the scalp, rather than throughout the entire head volume, there is no configuration of estimated sources that uniquely accounts for the EEG measurements. In other words, the problem is vastly underdetermined. For the purposes of this work, the epileptogenic focus is modeled as a single equivalent dipole of arbitrary strength and orientation. That is, surface potentials are interpreted as the superposition of the electric fields produced by a single dipole in three mutually orthogonal orientations at one location in the head. One need only discover the most likely dipole position and the level of contribution from each orientation which combine to induce scalp potentials that are best fit to the measured data.

Given this mandate, application of the FVM to the inverse problem in EEG would seem to require calculation of the forward solution for every possible dipole location in the gray matter elements, in each of three orientations. The potentials computed at the electrode sites would then be extracted and compared to those recorded by EEG to identify the most likely candidate dipole location. The set of data that maps the input-output relationship between all possible current sources and the electrode potentials on the scalp is known as the lead field matrix (LFM). As indicated, solution of the forward problem for a numerical model of high spatial resolution is a rigorous computational process that requires a great deal of CPU time. Therefore it is entirely impractical to solve the forward problem for each of the possible dipole locations and orientations.

Reciprocity is a well-known property of linear volume conductors that can be readily applied to the FVM by way of lead field analysis. By this scheme, the calculated electrode potentials for dipoles in any position are available by solving the forward problem only once for each measurement lead, rather than thrice for each of the millions of possible dipole locations. Thus, a complete patient-specific LFM can be compiled in a reasonable period of time for clinical application to EEG source localization. This concept is developed further in Section II-G2.

A desirable feature of this scheme is that the lead field data for a specific conductivity model can be used repeatedly to localize any number of equivalent dipole sources based on various EEG recording samples. The LFM depends only on the head model and the electrode montage [4], [5], [34]. In effect, a complete lead field data set provides the necessary information to localize one or a combination of equivalent dipole sources by any discrete volume localization method. The same data can be used to arrive at a distributed current density estimation of EEG sources. Similar implementations of lead field analysis based on the Finite Difference Method (FDM) are described in [35] and [34]. Examples of some other conductor model independent source localization methods are LORETA (Low Resolution Electromagnetic Tomography) – [11], [36], [37], and FOCUSS (Focal Underdetermined System Solution) – [38].

C. Verification of the Model

The analytical three-shell spherical conductor model provides an accurate account of potentials induced on the surface of a sphere, but is limited in its application to EEG source localization because a sphere does not reflect the real geometry of the human head. Simulated EEG measurements were obtained from the analytic three-shelled

spherical model and used to localize single equivalent dipole sources in a FVM version of the same sphere. Several of these experiments were carried out to analyze how factors such as spatial resolution of the model, source location, depth, and orientation, affect the localization accuracy in terms of the estimated source location, orientation, and magnitude.

D. Realistic Head Geometry

Since patient-specific data from MRI and other imaging modalities is usually available, it is proposed that this information can be processed to provide a regular grid of discrete volume elements, each identified by tissue type. Once tissue segmentation is complete, one can generate a large three-dimensional matrix of volume conductivities to which the numerical source localization algorithm will be applied.

To verify the importance of realistic head geometry in determining the location of epileptogenic foci, simulated scalp potentials produced by forward solution of a numerical (FVM) 3-shelled spherical model are used to localize a source in a FVM head model of realistic geometry. Localization errors are expected to be unreasonably large owing to the inconsistency between the spherical and realistic modeling techniques. This investigation also served to give an estimate of the number of volume elements required to represent a realistic head (which has irregular dimensions, unlike a sphere) with fine spatial resolution, and the time required to perform a forward calculation for a FVM model of this nature. Previous work has been done to examine the accuracy of spherical model in localizing cortical sources using scalp potentials derived from other types of realistic head models [14], [21].

E. Model Preparation

1) Finite Volume Decomposition: For the purpose of simulating the flow of current from a source in the brain to electrodes on the scalp (the forward problem), the assemblage of discrete volume elements are modeled as a three-dimensional mesh circuit. Theoretical details and justification for this treatment is provided in [24] and [26]. Each cube is represented by a node, which is coupled to six adjacent nodes by a resistor (see Figure 1-1). The conductivity of the connection between two neighbouring nodes (effective conductivity, σ_{eff}) is simply the series combination of the conductivities of the two voxels. That is, the nodes at the centres of voxels 0 and 1 are separated by the effective conductivity

$$\acute{o}_{eff1} = \frac{2\acute{o}_0\acute{o}_1}{\acute{o}_0 + \acute{o}_1}. \qquad (1)$$

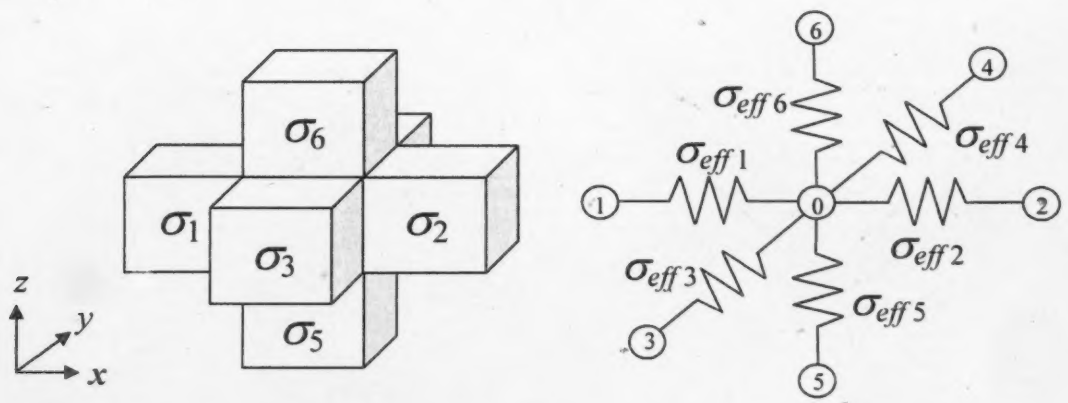

Figure 1-1: A set of adjacent voxels modeled as nodes in a 3D mesh circuit.

To accommodate the strong likelihood of anisotropic tissues, the conductivity of each voxel can be represented by three distinct values, one for each orthogonal direction (x, y, z) of current flow. In this context, the principle directions of conductivity are restricted to

the global axes of the model. That is, the conductivity of each voxel is *orthotropic*. Fortunately, incorporation of this specific form of anisotropic conduction does not add any computational complexity to the FVM decomposition algorithm.

For the purposes of this study, the origin of an electrical signal in the brain is modeled as a single current dipole – two current sources of equal and opposite magnitude (source/sink) located at nodes separated by some distance. Not only is this bipolar representation natural to the FVM, it also reflects the elongated shape of pyramidal cells from which recorded neural activity is believed to originate [1]. The extent of the simulated dipole can be increased by spreading the source and sink out across non-adjacent nodes, and the orientation of the dipole moment is defined by the spatial position of the source and sink with respect to one another.

2) *Finite Difference System of Equations*: A relationship between any node and its six neighbours is expressed using Kirchoff's Current Law – the sum of the currents flowing out of a node is zero, unless the node is the site of a current source or sink. The finite difference equation that describes the relationship amongst any set of adjacent nodes is

$$\begin{aligned} &\acute{o}_{eff1}(ø_0 - ø_1) + \acute{o}_{eff2}(ø_0 - ø_2) + \acute{o}_{eff3}(ø_0 - ø_3) + \\ &\acute{o}_{eff4}(ø_0 - ø_4) + \acute{o}_{eff5}(ø_0 - ø_5) + \acute{o}_{eff6}(ø_0 - ø_6) = \frac{I_0}{h}, \end{aligned} \tag{2}$$

where ψ_0 is the potential of the central node, ψ_n are the potentials of the adjacent nodes, σ_{effn} are the conductivities shared by the central node and each adjacent node (conductivity per unit length), I_0 is the total current flow out of the central node, and h is the side length of every voxel. Note that I_0 is zero for every voxel except those where a current source or sink are located. Briefly explained, the factor h scales effective

conductivities to account for voxel dimensions. This relationship is derived from Poisson's electrostatic equation as detailed in [39].

The difference equation (2) is applied to every volume element to create a system of equations governed by Ohm's Law,

$$\mathbf{A} \cdot \mathbf{v} = \mathbf{b}, \tag{3}$$

where **A** is the coefficient matrix, **v** is a column vector of the potentials at every node, and **b** is a column vector of the sum of currents leaving each node. **A** is a symmetric and sparse matrix with exactly seven nonzero elements per row, **b** is also a sparse vector – the only nonzero elements are due to the current source and sink specified for the particular forward problem. For a visual depiction of the matrix equation format see Figure 1-2.

Determining the vector of potentials **v**, then extracting the values at those nodes which represent scalp electrodes constitutes calculation of the forward problem in EEG. Conventionally, building a LFM requires solving the system by forcing a current source/sink combination at every pair of adjacent voxels in the solution space. Using the reciprocal approach, however, the current source is designated at an electrode voxel, while the current sink is placed at the reference electrode. Thus, there are only as many forward problems to solve as there are electrode leads.

Figure 1-2: A visual depiction of the finite difference system of equations. N is the number of voxels in the head model.

F. Solving the Forward Problem

1) *The Conjugate Gradient Method*: The objective is to be able to solve the system of equations (3) by inverting its coefficient matrix,

$$\mathbf{v} = \mathbf{A}^{-1} \cdot \mathbf{b}. \tag{4}$$

However, the larger the matrix dimensions, however, the more computationally demanding its inversion becomes. Since the dimensions of **A** could be millions by millions, it is clearly too large to invert, even for a modern computer processor. We rely on an iterative approach known as the Conjugate Gradient Method (CGM), used to solve linear systems of equations.

As noted above, **A** is sparse – it contains relatively few nonzero values. Furthermore, the coefficient matrix is symmetric and positive semidefinite. Proof of these properties is illustrated in [24]. These matrix attributes are necessary for employment of the CGM.

The CGM is an iterative technique designed to achieve the solution result using a number of steps that is no more than the dimension of the matrix itself. In practice though, the number of iterations may not need to be so large. Iterations need to be

carried out only until the mean squared difference between **A** v and the input vector **b** is less than some tolerance value å. That is,

$$\|\mathbf{A}\cdot\mathbf{v}_i - \mathbf{b}\|_2 < \varepsilon, \tag{5}$$

where $\mathbf{v}_i$ is the intermediate solution at iteration *i*. At every iteration, (5) is evaluated and once ε is sufficiently small, the iterated vector $\mathbf{v}_i$ is accepted as the approximation of the exact solution **v**, and the solver program is stopped. Previous work with the FVM has shown that a tolerance value of $\varepsilon = 10^{-10}$ or less gives minimum error when comparing potentials on the surface of a discretized inhomogeneous sphere to those calculated by a gold standard analytical model [24]. Therefore we assume that this convergence criterion will provide a solution vector, **v**, of acceptable accuracy for the purposes of source localization by lead field analysis.

2) Matrix Deflation: The coefficient matrix, **A,** is positive semidefinite which means that the system of equations does not have a unique solution. Since **A** is rank deficient by 1, the CGM will converge to a solution vector that is offset by some constant value which depends on the initial solution estimate, $\mathbf{v}_0$, provided to the solver program [40]. This problem is easily overcome by arbitrarily assigning a reference value to one of the potential variables, removing its row and column from **A**, and deleting the corresponding input and output variables from **v** and **b**. The deflated conductivity matrix $\mathbf{A}_d$ is positive definite and the remaining solution vector will be made up of values that are relative to the predefined reference potential [24]. In fact, this situation makes physical sense because monopolar EEG measurements are taken relative to an inactive electrode. By assigning a value of zero to the node that represents the reference electrode, the other electrodes will sense potentials that are relative to ground, as is the case in clinical

measurements. Recall, however, that the CGM is applicable to symmetric positive semidefinite systems, as well as those that are positive definite. Thus, matrix deflation is *not* strictly necessary for the solution method used in this work. Lack of uniqueness in the solution of the undeflated system (3) can be overcome by subtracting a constant value from the potential vector such that the reference node is grounded.

3) Preconditioning: One of the major parameters that influences the effectiveness of the CGM is the ratio of the largest eigenvalue of **A** to the smallest one, often referred to as the *condition number* of **A**. The closer the condition number is to one the more quickly the iterative process converges. The process of improving the condition number of a matrix is known as *preconditioning*. Prior to or during solution, preconditioning operations can be performed on **A**. Many such methods are available, but two that applicable and suitable to improve the condition of the extraordinarily large system (3) are Jacobi preconditioning and polynomial preconditioning with Chebyshev polynomials. These methods are applied to all solutions of FVM systems in this research and are described in detail in [41].

Head model decomposition was implemented using MATLAB. Vectorization techniques were applied widely throughout the code to avoid any programming loops that might be used for node-by-node computations, since loops executed by interpretive software platforms such as MATLAB are notoriously inefficient. Jacobi preconditioning and generation of the polynomial coefficients, which are read as inputs to the solver program [41], were also generated using MATLAB. The highly vectorized program used in this research (see Figure 1-3) can prepare a high resolution 3-shelled spherical model (~4,000,000 voxels) for forward solution in about 6 minutes on the UltraSparc II 296

MHz processor with 1.2 GB RAM. The polynomial preconditioned CGM solver was programmed and compiled using C for increased computational and data input/output efficiency.

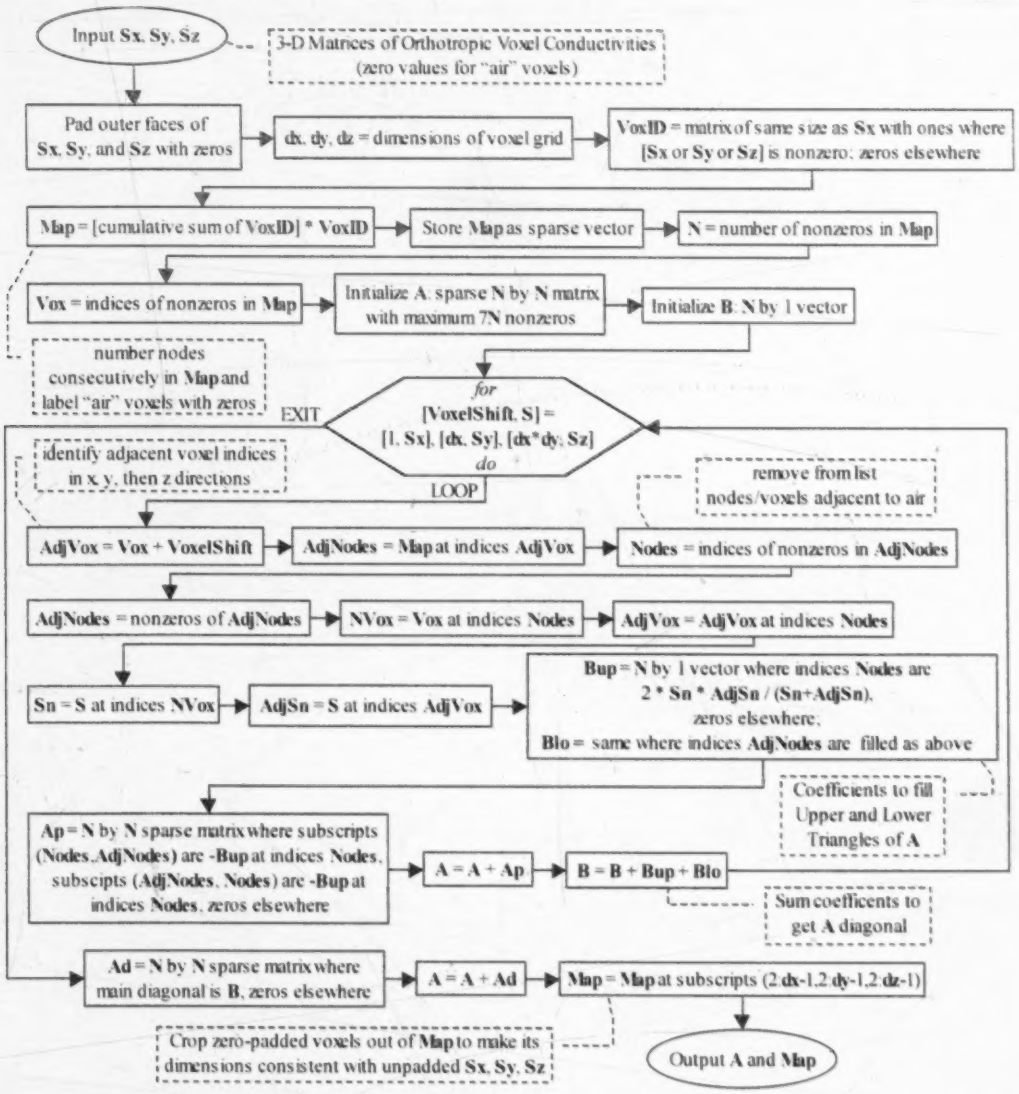
Input Sx, Sy, Sz
3-D Matrices of Orthotropic Voxel Conductivities (zero values for "air" voxels)
Pad outer faces of Sx, Sy, and Sz with zeros
dx, dy, dz = dimensions of voxel grid
VoxID = matrix of same size as Sx with ones where [Sx or Sy or Sz] is nonzero; zeros elsewhere
Map = [cumulative sum of VoxID] * VoxID
Store Map as sparse vector
N = number of nonzeros in Map
Vox = indices of nonzeros in Map
Initialize A: sparse N by N matrix with maximum 7N nonzeros
Initialize B: N by 1 vector
number nodes consecutively in Map and label "air" voxels with zeros
EXIT
for [VoxelShift, S] = [1, Sx], [dx, Sy], [dx*dy, Sz] do
LOOP
identify adjacent voxel indices in x, y, then z directions
remove from list nodes/voxels adjacent to air
AdjVox = Vox + VoxelShift
AdjNodes = Map at indices AdjVox
Nodes = indices of nonzeros in AdjNodes
AdjNodes = nonzeros of AdjNodes
NVox = Vox at indices Nodes
AdjVox = AdjVox at indices Nodes
Sn = S at indices NVox
AdjSn = S at indices AdjVox
Bup = N by 1 vector where indices Nodes are 2 * Sn * AdjSn / (Sn+AdjSn), zeros elsewhere;
Blo = same where indices AdjNodes are filled as above
Coefficients to fill Upper and Lower Triangles of A
Ap = N by N sparse matrix where subscripts (Nodes, AdjNodes) are -Bup at indices Nodes, subscipts (AdjNodes, Nodes) are -Bup at indices Nodes, zeros elsewhere
A = A + Ap
B = B + Bup + Blo
Sum coefficents to get A diagonal
Ad = N by N sparse matrix where main diagonal is B, zeros elsewhere
A = A + Ad
Map = Map at subscripts (2:dx-1,2:dy-1,2:dz-1)
Crop zero-padded voxels out of Map to make its dimensions consistent with unpadded Sx, Sy, Sz
Output A and Map

Figure 1-3: Vectorized Finite Volume decomposition algorithm flowchart. Voxel locations in the 3D model grid are referenced by triplets of (x, y, z) subscripts, or equivalently by scalar indices ranging from 1 to $dx*dy*dz$. Each "non-air" voxel in the 3D model grid is assigned a unique node number that dictates its place in the system of equations. The coefficient matrix **A** is symmetric since the effective conductivity between nodes a and b appears in the linear equation for node a as the coefficient for potential variable b, and vice-versa. Furthermore, since elements on the main diagonal of **A** are just the negated sum of coefficients in that row (or column), only elements in **A**'s upper triangle need be computed explicitly. This is accomplished by considering conductivities of adjacent voxels only in the positive x, y, and z directions relative to each node. All uses of the multiplication symbol * indicate array (not matrix) multiplication. Boxes with dotted outlines enclose comments on the algorithm.

G. The Inverse Problem

1) Localization Method: There are many possible ways to estimate single equivalent dipole sources given a complete LFM, which is specific only to the patient's head and the EEG recording montage. Here, a current dipole is defined as a source and sink separated by one voxel. This middle voxel is deemed to be the dipole location (see Figure 1-4). The exhaustive (and inefficient) method used to localize dipole sources in this work is described next.

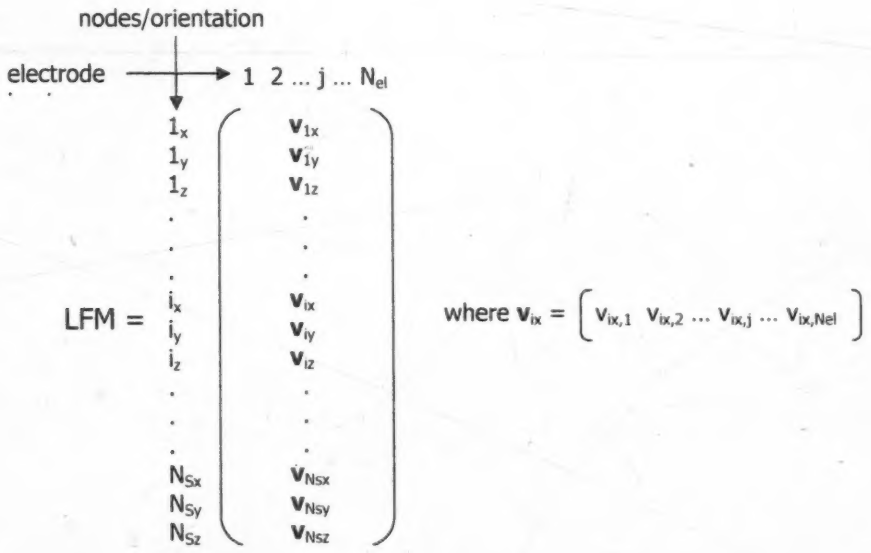

Figure 1-4: A visual description of the LFM. $\mathbf{v}_{ix}$ is the row vector of scalp potentials extracted from a forward solution of a dipole at the i^{th} voxel, oriented in the x direction. N_{el} is the number of electrode pairs. N_S is the number of voxels in the localization solution space. $3N_S$ forward solutions are required to compile the LFM by this method.

At each candidate dipole source location (a voxel denoted by subscript i), three vectors of electrode potentials ($\mathbf{v}_{ix}$, $\mathbf{v}_{iy}$, $\mathbf{v}_{iz}$) induced by mutually orthogonal dipoles at voxel i are extracted from the LFM and combined according to

$$\mathbf{v}_i = a_i\mathbf{v}_{ix} + b_i\mathbf{v}_{iy} + c_i\mathbf{v}_{iz}, \quad \text{where } \sqrt{a_i^2 + b_i^2 + c_i^2} = 1. \tag{6}$$

The result is a vector of electrode potentials, $\mathbf{v}_i$, caused by a unit dipole source of arbitrary orientation at location i. The linear coefficients in (6) are chosen such that $\mathbf{v}_i$ matches the measured (or simulated) EEG potentials ($\mathbf{v}_{EEG}$) as closely as possible by minimizing the function J_i, given by

$$J_i = \left\| \mathbf{v}_{EEG} - \mathbf{v}_i \right\|_2 . \tag{7}$$

The quality of fit at each voxel is measured by J_i, the mean squared difference between the EEG potential vector, $\mathbf{v}_{EEG}$, and the calculated electrode potential vector, $\mathbf{v}_i$. The voxel location (i) of the single dipole source whose resultant electric field most closely matches the scalp EEG data in a least squares sense (has the smallest value of J_i) is chosen as the source location. The linear coefficients of (6) for the selected voxel yield the source orientation. The estimated dipole moment (source magnitude, m) is obtained by multiplying the pseudo-inverse of the best-fit electrode potential vector, $\mathbf{v}_i$, by the measured EEG potential vector, as in

$$m = \mathbf{v}_i^{\dagger} \cdot \mathbf{v}_{EEG} . \tag{8}$$

The localization method described is an exhaustive search of the solution space for a single equivalent dipole that best accounts for the measured scalp potentials. This technique is not a recommended approach to the inverse problem because it is naïve to assume that the source of a patient's epileptic activity can be represented by a *single* equivalent dipole. Furthermore, scanning every voxel to assess the quality of fit at each candidate location is extremely time consuming in a high resolution head model. More sophisticated techniques such as directed searches or simulated annealing, which eliminate the need for an exhaustive search are available and discussed extensively in literature [42]–[44].

2) Collection of Lead Field Data: As described in above, EEG source localization requires calculation of the LFM. From the conventional perspective, acquisition of this data requires solving the forward problem thrice for each voxel in the solution space. For a sphere set in a 100^3 voxel grid, there are approximately 530,000 non-air voxels. Since gray matter typically constitutes 1/8 of head volume, the solution space would consist of about 66,250 voxels. Therefore the forward problem must be solved about 66,250×3=198,750 times. On the UltraSparc II 296 MHz processor with 1.2 GB RAM, it takes roughly 10 CPU minutes to perform one forward solution for a spherical model of this refinement, so it would take over five CPU years to calculate the entire lead field matrix for this level of discretization. Similarly, for a sphere set in a 200^3 voxel grid, it would take around 360 CPU years to generate the entire LFM. Obviously, these computational requirements are prohibitively time consuming. Therefore, the LFM must be calculated by some other means for this method to be implemented clinically. Fortunately, such means are available owing to the reciprocal nature of the FVM system of equations.

The three-dimensional mesh circuit that is used to model current flow through the discrete volume elements is a linear resistive network. Thus, it is reciprocal. When a current source is placed at 'Port A' in such a network, it will result in a voltage across the terminals of 'Port B'. Now, if the current source is moved to 'Port B', reciprocity guarantees that exactly the same voltage will be induced across 'Port A' (see Figure 1-5). Reciprocity of the FVM system is evident by the symmetric nature of its coefficient matrix **A**, since replacing **A** with its transpose in (3) does not affect the validity of the equation, yet is equivalent to reversing the input and output dimensions of the

relationship. This special property can be exploited to calculate the complete LFM by computing the forward solution only once for every electrode lead (less than 100 solutions) rather than hundreds of thousands of times.

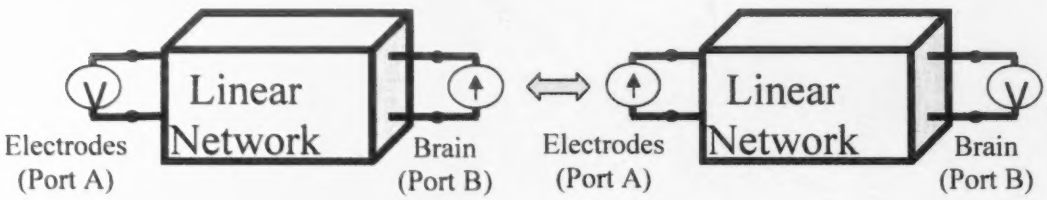

Figure 1-5: Linear network reciprocity illustrated.

Rather than specifying the current dipole at each voxel in the solution space, we place the current source at each electrode site (j) and the current sink at the reference electrode, then solve the forward problem to obtain potentials everywhere in the solution space. The result is the potential field for that particular electrode lead. Taking the 3-D gradient of the potential at each voxel gives the electric field, $\mathbf{v}_{ej}$, produced in the conductor by stimulation of that lead. Thus, we compute the lead field matrix column-wise instead of row-wise (see Figure 1-6).

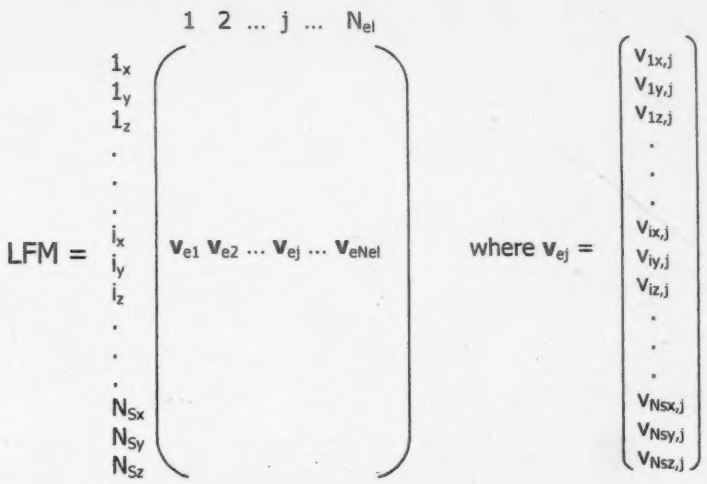

Figure 1-6: A visual description of a lead field matrix obtained by reciprocity. $\mathbf{v}_{ej}$ is the column vector of gray matter potentials extracted from a forward solution of a source/sink on the j^{th} electrode lead, but is interpreted as the j^{th} electrode potential induced by $3N_S$ dipoles at N_S solution space voxels. N_{el} is the number of electrode pairs. N_S is the number of voxels in the solution space. N_{el} forward solutions are required to compile the LFM by this method.

After the solver program generates a forward solution for each lead, a simple multiplication operation must be performed on the vectors to reverse the effect of Jacobi preconditioning [41]. Also, all potentials are set relative to the node that represents the reference electrode, which is assigned ground potential. Then the lead field matrix is compiled, using data from only the nodes that are part of the solution space. Since this large data set depends only on the head model and the electrode montage, the bulk of the computational workload needs to be performed only once per patient. Finally, an appropriate source localization routine is executed.

All post-processing including lead field compilation and dipole localization were implemented MATLAB. It should be noted that with the exhaustive search dipole fitting method used here, node-by-node evaluation of the lead field data is unavoidable, that is,

the process cannot be vectorized. On the UltraSparc II 296 MHz processor with 1.2 GB RAM, the localization program takes about ten minutes to estimate a dipole position from 345,243 nodes (the number of voxels in the solution space of a sphere set in a 100^3 grid). This process takes 1.5 hours when searching 2,757,473 nodes (200^3 grid). It would be advisable to code such a localization program in a language that executes loops more efficiently, such as C, since the process may need to be repeated for various input (EEG) data sets.

H. Verification

1) Source Localization Accuracy: The three-shelled sphere is an analytic model used to determine the electric potential on the surface of a spherical volume inside which the location, orientation, and magnitude of a dipole current source is specified. The volume is composed of three concentric shells where the outer and middle shells represent the scalp and skull, and the inner sphere models the brain. Each region is assigned a conductivity value equal to that of the tissue it represents. The equation that describes electric potential on the surface of this simplistic head model serves as a "gold standard" to which results from the numerical procedure are compared.

The ability of the FVM to accurately represent electric fields in an inhomogeneous volume conductor was verified by using lead field data obtained from a finite volume version of the three-shelled sphere to localize simulated dipole sources given "scalp" potentials from the analytic model of the same three-shelled sphere. The outer radius of the sphere was specified as R = 92 mm, and the inner shells had fractional radii of 0.92 R (84.64 mm) and 0.87 R (80.04 mm). Tissue conductivities were specified as $(3.5\ \Omega m)^{-1}$ for scalp/brain, and $(280\ \Omega m)^{-1}$ for bone. These values are typically used in three-shelled

spherical models of the head [24], though references to differing conductivity parameters are also common. FVM decomposition was executed on the spherical volume situated inside a cubic grid of 100^3 voxels (1.84 mm resolution for a sphere with 92 mm radius). The spherical volume takes up 523,305 voxels in this grid. Localization experiments were performed for dipoles at several positions in the sphere (eccentricity = 0.5, 0.6, 0.7, and 0.8) along three Cartesian axes (x, y, and z). In each of the 12 dipole positions, the localization procedure was carried out for sources with radial and tangential orientation. The 24-lead electrode montage (a superset of the 10-20 system) used to extract surface potentials from the analytic sphere and to perform lead field analysis on the numeric model is shown in TABLE 1-1.

TABLE 1-1

24-LEAD ELECTRODE MONTAGE. TIP IS MEASURED IN DEGREES AS THE ANGULAR DISPLACEMENT FROM THE POSITIVE *Z* AXIS (TOP) TOWARD THE *XY* PLANE. SPIN IS IN DEGREES AS THE ANGULAR DISPLACEMENT FROM THE POSITIVE *X* AXIS (R. EAR) TO THE POSITIVE *Y* AXIS (NOSE).

Electrode No.	Tip (degrees)	Spin (degrees)
1	90.00	108.00
2	90.00	72.00
3	58.57	130.71
4	58.57	49.29
5	45.00	180.00
6	45.00	0.00
7	58.57	229.29
8	58.57	-49.29
9	90.00	252.00
10	90.00	-72.00
11	90.00	144.00
12	90.00	36.00
13	90.00	180.00
14	90.00	0.00
15	90.00	216.00
16	90.00	-36.00
17	45.00	90.00
18	0.00	90.00
19	45.00	270.00
20	112.50	162.00
21	112.50	18.00
22	112.50	-162.00
23	112.50	-18.00
24	90.00	-90.00
reference	22.50	270.00

The complete set of localization experiments was repeated for a discretized 3-shelled sphere with the same shell proportions and conductivity parameters, but with double the spatial resolution. The spherical volume was set inside a cubic grid of 200^3 voxels (0.92 mm resolution). The sphere constitutes 4,187,857 voxels in this grid.

2) Error Measurements: The quality of single dipole source localization is measured

by three factors: displacement error, orientation error, and magnitude (dipole moment) error. The importance of achieving adequately small displacement error is apparent – the epileptogenic focus must be precisely identified so that it can be surgically removed with minimal damage to the surrounding functional brain tissue. Dipole orientation also yields knowledge about dipole location because EEG sources (pyramidal cells) tend to be aligned normal to the surface of the cortex. Finally, the relative magnitude of a localized dipole is an indication of the surface area of coherently active cortical cells. This information is a clue to the size of the affected region of brain tissue [1].

Additionally, error norms between the simulated electrode potentials and those extracted from the LFM for the estimated dipoles were also be examined to get a sense of how closely the scalp potential vectors match. However this data is somewhat extraneous since it is the localization results that are important in a clinical setting.

3) Importance of Realistic Head Geometry: Since the purpose of this experiment is to demonstrate the inaccuracy of spherical models, it is unnecessary to use a fully detailed realistic head volume. Rather a simplistic, two-tissue segmentation was performed on the National Library of Medicine's Visible Man CT data. The head was framed in a 200^3 grid, and the volume took up 2,511,550 voxels (roughly 60% of the spherical volume set in the same cubic grid). Voxels were identified as either bone or soft tissue and generalized conductivities (as in the spherical model, $(3.5\ \Omega m)^{-1}$ and $(280\ \Omega m)^{-1}$) were assigned to the tissue types. Electrode sites were designated on the realistic head model by fitting a sphere to the voxels that represent the skull. The sphere was fit by least squares and its centre was used as the origin of the spherical coordinate system. Based on this origin, the electrode positions (as defined in TABLE 1-1) were assigned to

the nearest neighbour voxels on the surface of the discretized head model.

Lead field analysis was not used to locate dipole sources in the realistic head. Rather, a simplified localization algorithm was used to conserve computational resources. Forward solutions were calculated for many dipole locations over a continuous range of eccentricities (0.42 through 0.86, in steps of 0.02) along the x, y, and z axes, in both radial and tangential orientations. Scalp potentials at the electrode sites were extracted from the forward solution and stored. The full set of simulated EEG vectors that were applied to the discretized 3-shelled sphere were used again in this test. For each of the 24 dipole positions in the simulated set (x, y, z, eccentricity = 0.5, 0.6, 0.7, 0.8, radial and tangential) localization was performed by comparing the simulated potential vector to scalp potentials generated using the realistic head model. Candidate dipole positions included only those located along the axis of interest, and only in one orientation. Since solution space is restricted to a small number of locations (24 candidate positions per dipole), this method is not a thorough means of source localization. However it serves to illustrate that volume currents in a human head are not adequately modeled by conduction in a 3-shelled sphere.

Since dipole orientations were fixed, and dipole moment was not examined, only the displacement error is reported. To obtain some measure of source displacement, the irregular shape of the realistic head must somehow be reconciled with the spherical model. A sphere was fit (again, in a least squares sense) to the voxels designated as electrode sites. The radius of this co-registered sphere was defined to be 92 mm, corresponding to the specified radius of the spherical model. Dipole eccentricities in the realistic head were then based on the centre and radius of the co-registration sphere.

Clearly, this 92 mm sphere does not span the full 200^3 cubic grid, so the spatial resolution of the head model is less than 0.92 mm. In fact, for this particular head, the side length of each voxel is 1.21 mm. Note that this value is strictly dependent on the radius of the co-registration sphere relative to the grid spacing, and the arbitrary assertion that the sphere has a 92 mm radius. This is an artificial construct solely for the purpose of model comparison. In practice, it is the grid refinement relative to the patient's actual head dimensions that define the spatial resolution of the head model.

III. Results

A. 3-Shelled Sphere

The less-refined (1.84 mm resolution) sphere achieved average displacement accuracy of 2.35 (0.00 – 4.11) mm, average orientation error of 0.72 (0.00 – 4.64) degrees, and average magnitude (dipole moment) error of 11.07 (4.83 – 25.65) percent. The higher resolution (0.92 mm resolution) sphere achieved an average displacement accuracy 1.03 (0.00 – 3.32) mm, average orientation error of 0.23 (0.00 – 1.14) degrees, and average magnitude error of 4.31 (1.39 – 7.26) percent. For both models, radial and tangential dipole estimations tended to be slightly deeper in the sphere than the actual dipole location. Localization error on this scale is quite acceptable and an improvement on the results of many previous EEG source localization systems.

Visual representations of dipole localization errors in the 100^3 grid for radial and tangential orientations are given in Figure 1-7 and Figure 1-8, respectively. Similarly, Figure 1-9 and Figure 1-10 show dipole localization errors in the 200^3 grid. All test positions and the 24-lead electrode arrangement are depicted on a 3 dimensional plot.

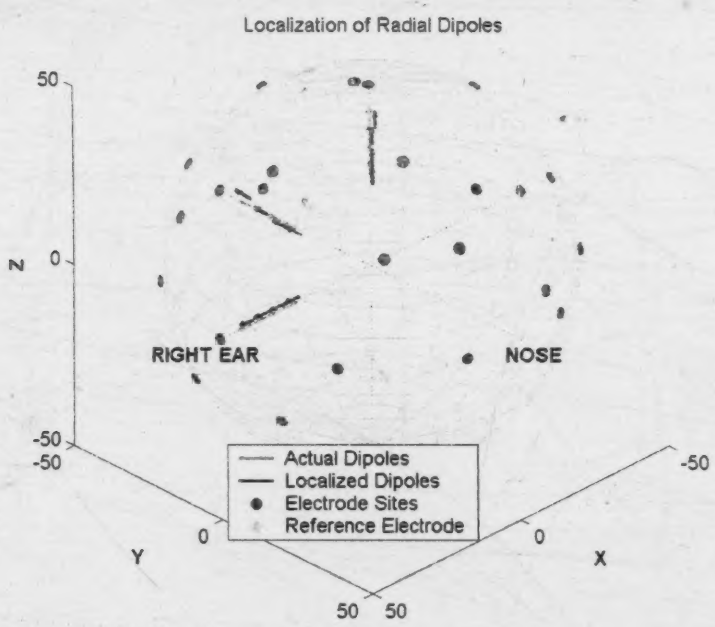

Figure 1-7: Estimation of radial dipoles in a 3-shelled sphere with 1.84 mm resolution (100^3 grid).

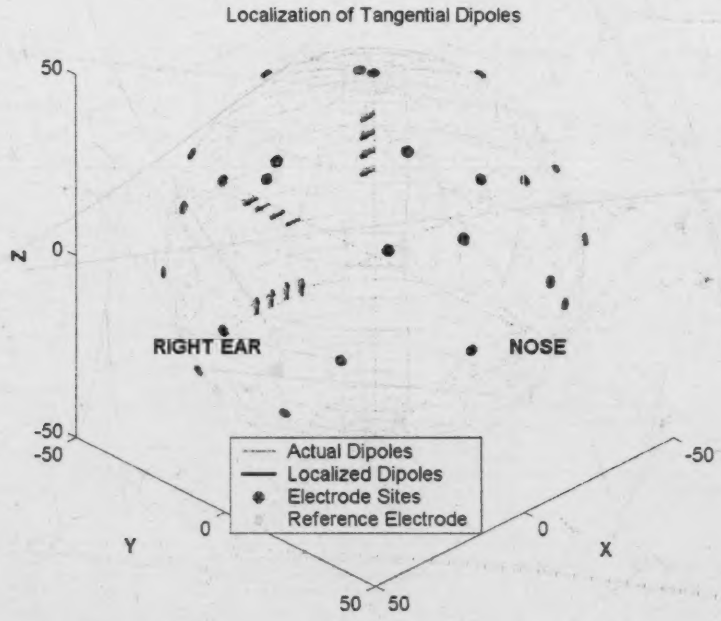

Figure 1-8: Estimation of tangential dipoles in a 3-shelled sphere with 1.84 mm resolution.

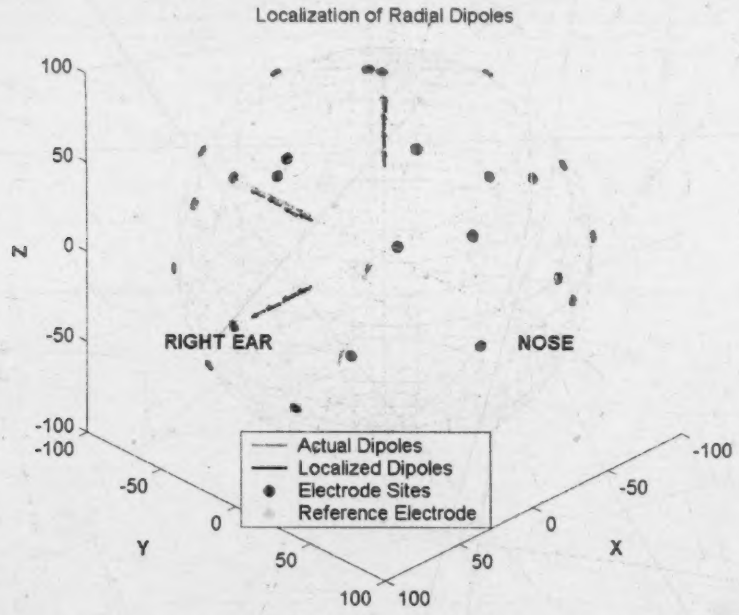

Figure 1-9: Estimation of radial dipoles in a 3-shelled sphere with 0.92 mm resolution (200^3 grid).

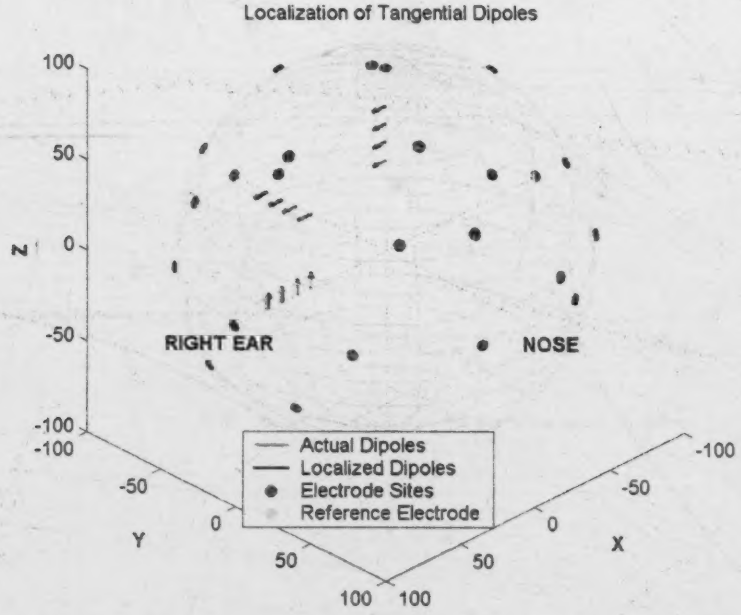

Figure 1-10: Estimation of tangential dipoles in a 3-shelled sphere with 0.92 mm resolution.

TABLE 1-2 shows the displacement, magnitude, and orientation errors for all localization tests as depicted in Figure 1-7 through Figure 1-10.

TABLE 1-2

POSITION ERROR IN MILLIMETERS FOR EACH TEST DIPOLE. ORIENTATION ERROR IS EXPRESSED IN DEGREES DIFFERENCE BETWEEN THE ACTUAL AND ESTIMATED SOURCES, AND AMPLITUDE ERROR AS A PERCENTAGE OF THE SIMULATED SOURCE MAGNITUDE. BLACK CELLS INDICATE THE MINIMUM ERROR VALUES IN EACH COLUMN. SHADED CELLS ARE THE MAXIMUM ERRORS.

			grid: 100^3, resolution = 1.84 mm 523,305 nodes			grid: 200^3, resolution = 0.92 mm 4,187,857 nodes		
		Eccentricity	Displ. Err. (mm)	Mag. Err. (%)	Ori. Err. (deg.)	Displ. Err. (mm)	Mag. Err. (%)	Ori. Err. (deg.)
Radial	x	0.5	2.60	12.48	0.91	1.30	5.79	0.46
		0.6	2.60	13.66	1.15	1.30	5.98	0.60
		0.7	2.60	15.46	1.43	0.00	7.26	0.88
		0.8	2.60	17.40	2.27	0.00	5.68	0.68
	-y	0.5	4.11	9.95	1.22	2.60	4.20	0.29
		0.6	4.11	10.89	1.24	3.32	4.11	0.17
		0.7	1.84	16.63	2.56	2.06	5.60	0.59
		0.8	3.68	25.65	4.64	1.84	5.64	1.14
	z	0.5	4.11	9.45	0.29	2.06	3.73	0.07
		0.6	4.11	10.64	0.04	1.30	5.08	0.03
		0.7	2.60	15.53	0.12	1.30	4.88	0.17
		0.8	4.11	16.04	0.67	2.06	1.39	0.13
Tangential	x	0.5	2.60	6.93	0.42	0.00	4.14	0.07
		0.6	1.84	8.62	0.13	0.92	3.92	0.10
		0.7	1.84	7.93	0.06	0.92	3.81	0.07
		0.8	1.84	6.46	0.05	1.84	3.69	0.08
	-y	0.5	0.00	8.99	0.00	0.00	4.09	0.00
		0.6	0.00	8.58	0.00	0.00	3.90	0.00
		0.7	0.00	8.13	0.00	0.92	3.03	0.00
		0.8	1.84	4.83	0.00	0.92	3.14	0.00
	z	0.5	1.84	9.18	0.00	0.00	4.09	0.00
		0.6	1.84	8.69	0.00	0.00	3.76	0.00
		0.7	1.84	7.82	0.00	0.00	3.31	0.00
		0.8	1.84	5.71	0.00	0.00	3.18	0.00

Figure 1-11 and Figure 1-12 show sample profiles of the dipole fitting function, $-\log(J_i)$, where J_i is defined by (7), for two of the test dipoles, across one central slice of the sphere (200^3 grid). The dot indicates the actual dipole location and its corresponding fit to the simulated potentials. The estimated dipole location is found at the profile peak. Note that an exact fit to the simulated scalp potentials would yield an infinite "Goodness

of Fit" peak. We observe that the peaks of the dipole fitting function are quite well defined and very close to the actual dipole location, even in the case of maximum displacement error of 3.32 mm (Figure 1-11). In practice, of course, EEG recordings are significantly distorted by noise, which would have a smearing effect on the dipole fitting profile. Nonetheless, these noise-free illustrations highlight the inherent ability of a high resolution finite volume conductor model to yield calculated surface potentials of excellent accuracy with respect to the analytic "gold standard".

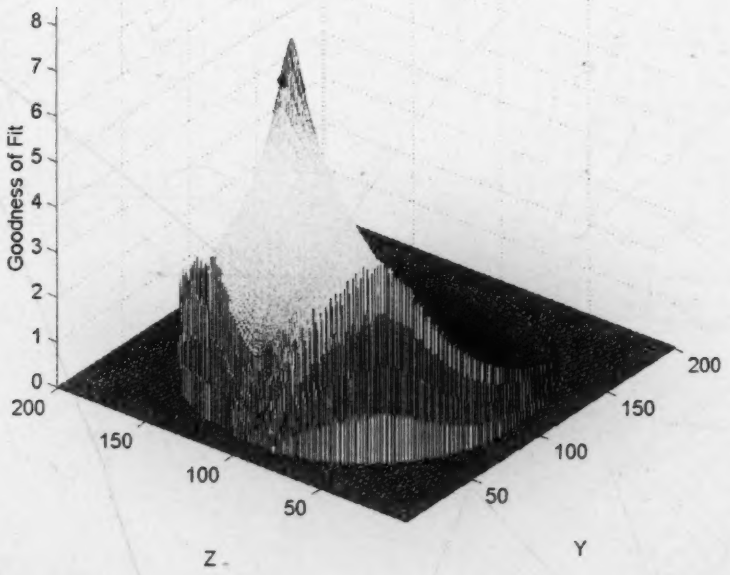

Figure 1-11: Example Goodness of Fit profile,-log(J_i), through a central slice of the 200^3 sphere on the x axis (sagittal slice). The actual dipole position, indicated by the dot near the top of the peak, is at eccentricity 0.6 radially oriented on the negative y axis. Displacement error for this estimated dipole is 3.32 mm. In this figure the origin is shifted to the corner of the voxel grid.

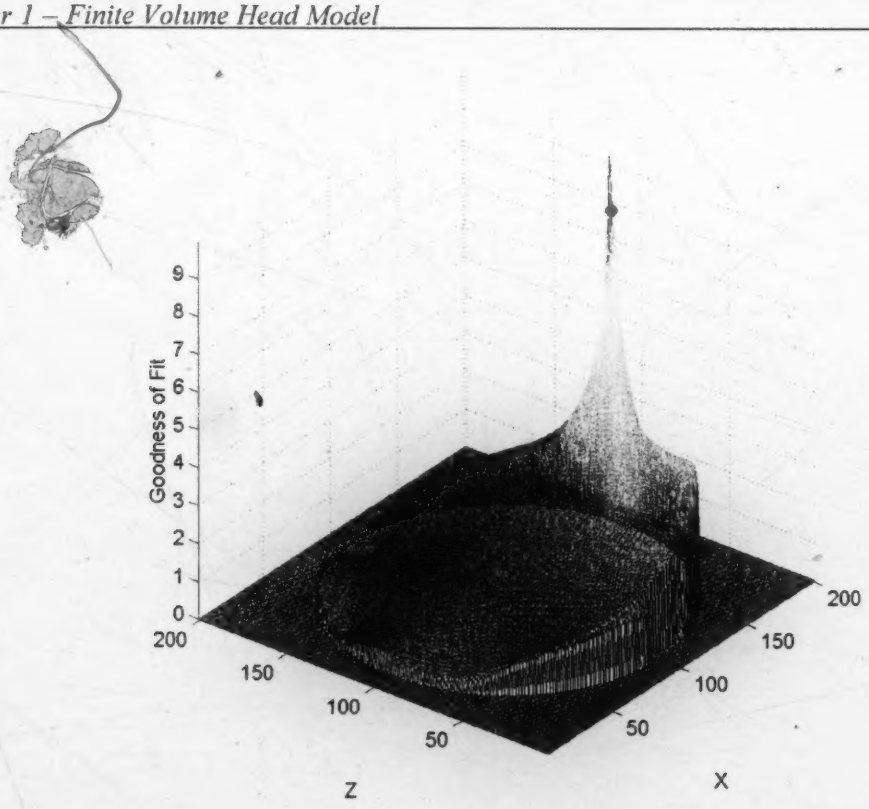

Figure 1-12: Dipole Goodness of Fit,-log(J_i), through a central slice of the 200^3 sphere on the *y* axis (coronal slice). The actual dipole position, indicated by the dot near the top of the peak, is at eccentricity 0.8 tangentially oriented on the positive *x* axis. Displacement error for this estimated dipole is 1.84 mm. In this figure the origin is shifted to the corner of the voxel grid.

Corresponding L1, L2, and L∞ potential vector error norms are displayed in TABLE 1-3.

Note that error norms are generally 1.5 to 2.5 times higher for the lower resolution model.

TABLE 1-3

L_1, L_2, AND L_∞ ERROR NORMS OF THE SCALP POTENTIAL VECTORS FOR EACH DIPOLE. V_{FV} IS THE CALCULATED SCALP POTENTIAL VECTOR FOR THE ESTIMATED DIPOLE. V_A IS THAT OF THE ACTUAL DIPOLE GENERATED BY THE ANALYTIC 3-SHELLED SPHERE MODEL. BLACK CELLS INDICATED THE MINIMUM ERROR NORMS IN EACH COLUMN. SHADED CELLS ARE THE MAXIMUM ERRORS.

			grid: 100^3, resolution = 1.84 mm 523,305 nodes			grid: 200^3, resolution = 0.92 mm 4,187,857 nodes		
		Eccentricity	$\frac{\lvert V_{FV}-V_A\rvert_1}{\lvert V_A\rvert_1}\times 100\%$	$\frac{\lvert V_{FV}-V_A\rvert_2}{\lvert V_A\rvert_2}\times 100\%$	$\frac{\lvert V_{FV}-V_A\rvert_\infty}{\lvert V_A\rvert_\infty}\times 100\%$	$\frac{\lvert V_{FV}-V_A\rvert_1}{\lvert V_A\rvert_1}\times 100\%$	$\frac{\lvert V_{FV}-V_A\rvert_2}{\lvert V_A\rvert_2}\times 100\%$	$\frac{\lvert V_{FV}-V_A\rvert_\infty}{\lvert V_A\rvert_\infty}\times 100\%$
Radial	x	0.5	1.90%	1.80%	1.78%	1.26%	1.24%	1.18%
		0.6	2.05%	1.76%	1.53%	1.44%	1.34%	1.11%
		0.7	2.02%	1.58%	1.20%	1.47%	1.30%	0.88%
		0.8	2.04%	1.51%	0.85%	1.58%	1.07%	0.55%
	-y	0.5	1.88%	1.90%	1.35%	1.32%	1.28%	0.92%
		0.6	2.15%	2.11%	1.61%	1.47%	1.48%	1.33%
		0.7	3.46%	2.69%	1.54%	2.13%	1.73%	1.02%
		0.8	3.95%	2.75%	1.34%	2.07%	1.49%	0.83%
	z	0.5	0.60%	0.70%	1.53%	0.28%	0.33%	0.57%
		0.6	0.52%	0.74%	1.77%	0.30%	0.41%	1.06%
		0.7	0.64%	0.76%	1.48%	0.24%	0.36%	1.04%
		0.8	0.52%	0.62%	1.11%	0.24%	0.30%	0.52%
Tangential	x	0.5	0.87%	0.99%	1.56%	0.53%	0.62%	0.56%
		0.6	1.16%	1.06%	0.84%	0.64%	0.69%	0.81%
		0.7	0.65%	0.71%	0.65%	0.53%	0.63%	0.67%
		0.8	1.05%	1.02%	0.91%	0.58%	0.68%	0.82%
	-y	0.5	1.18%	1.23%	1.49%	0.57%	0.68%	0.75%
		0.6	1.22%	1.18%	1.35%	0.56%	0.62%	0.71%
		0.7	1.65%	1.80%	2.25%	0.84%	0.90%	1.08%
		0.8	0.88%	0.91%	0.74%	0.63%	0.59%	0.50%
	z	0.5	1.41%	1.72%	1.85%	1.02%	1.08%	1.00%
		0.6	1.17%	1.56%	1.68%	1.01%	1.06%	0.90%
		0.7	1.21%	1.49%	1.54%	1.00%	1.03%	0.81%
		0.8	1.31%	1.49%	1.44%	0.98%	0.99%	0.73%

B. Realistic Head Geometry

TABLE 1-4 shows the complete set of displacement errors in millimeters for the realistic head model. Note that no tests were performed for dipoles at eccentricity = 0.7, 0.8 on the *x* axis, or eccentricity = 0.8 on the *z* axis because those locations lie outside the brain in the realistic head volume.

TABLE 1-4

DISPLACEMENT ERRORS OF ESTIMATED DIPOLES IN THE REALISTIC HEAD MODEL. THE SECOND COLUMN IS A DESCRIPTION OF WHERE THE DIPOLE WAS LOCALIZED RELATIVE TO THE ACTUAL DIPOLE POSITION.

			grid: 200^3 resolution = 1.21 mm 2,511,550 nodes	**Relative or Anatomical Dipole Localization**
		Eccentricity	Displacement Error (mm)	---
Radial	x	**0.5**	9.20	deeper
		0.6	-22.08	outside head
	-y	**0.5**	9.20	deeper
		0.6	18.40	deeper
		0.7	27.60	deeper
		0.8	36.80	deeper
	z	**0.5**	9.20	deeper
		0.6	18.40	deeper
		0.7	27.60	deeper
Tangential	x	**0.5**	1.84	deeper
		0.6	9.20	deeper
	-y	**0.5**	9.20	deeper
		0.6	18.40	deeper
		0.7	22.08	deeper
		0.8	23.92	deeper
	z	**0.5**	-31.28	within skull
		0.6	-22.08	within skull
		0.7	-12.88	within skull

As expected, using simulated potentials produced by a spherical model to estimate the location of dipoles in a realistic head yields very large errors (1.84 – 36.8 mm). In some cases, the estimated dipoles are positioned outside the physiological solution space (the brain), or even outside the head volume. These results reinforce the assertion that realistic head models are important for accurate EEG source localization. Figure 1-13 through Figure 1-15 show examples of localization results from this experiment.

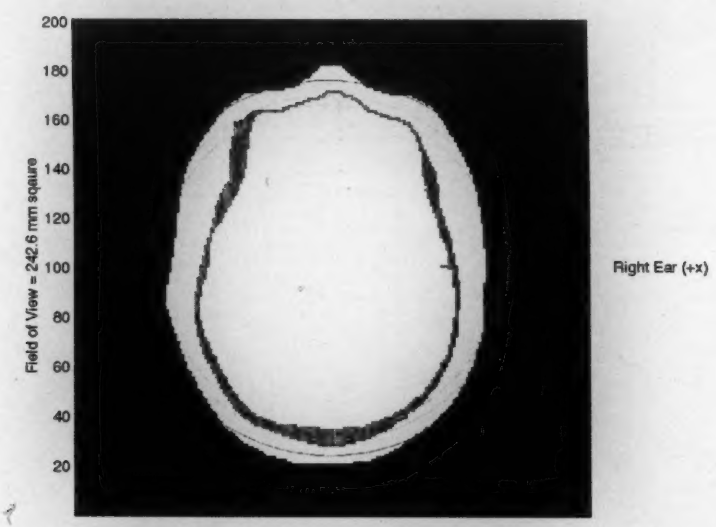

Figure 1-13: Axial view of radial source localization in a realistic head model with 1.21 mm resolution (200^3 grid). The arrow inside the skull is the simulated source location. The arrow to the right of the head is the localized source. The outermost circle is the co-registration sphere (radius = 92 mm). The two inner circles mark the skull region of 3-shelled sphere. Displacement error is 22.1 mm. Dipole was localized outside head volume.

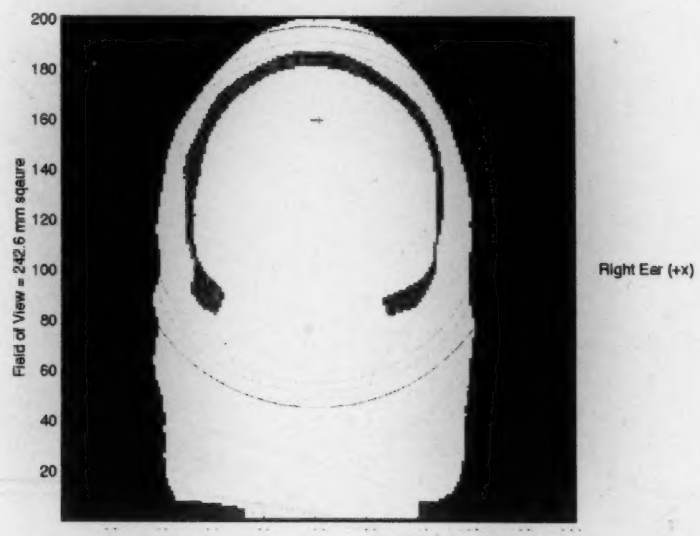

Figure 1-14: Coronal view of tangential source localization in a realistic head model with 1.21 mm resolution (200^3 grid). The arrow in the brain region is the simulated source location. The arrow inside the skull at the top of the head is the localized source. Overlaid spheres are as in Figure 1-13. Displacement error is 31.3 mm. Dipole was localized outside brain region.

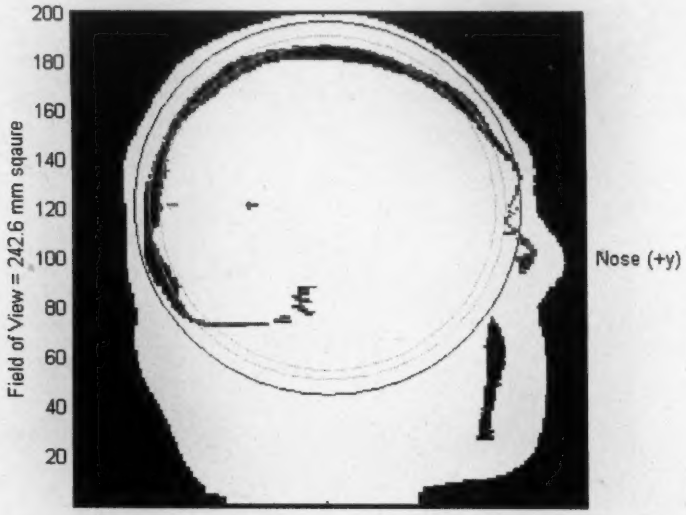

Figure 1-15: Sagittal view of radial source localization in a realistic head model with 1.21 mm resolution (200^3 grid). The arrow just inside the skull at the back of the head (left) is the simulated source location. The arrow near the middle of the brain region is the localized source. Overlaid spheres are as in Figure 1-13. Displacement error is 36.8 mm.

IV. Analysis of Results

The results given in this report are intended to demonstrate the capacity of the FVM for application to the problem of EEG source localization. Specifically, it was shown that this model can be effectively implemented with very high spatial resolution using an interpretive software platform such as MATLAB, though the iterative solution process is better handled by a lower-level computing language like C. Also, it was shown that a fine three-dimensional grid of discrete volumes can model volume current flow through an inhomogeneous medium with acceptably low error. The linearity of this model is exploited to build a complete LFM, which provides all the necessary data for any voxel-based source localization algorithm, in a clinically acceptable time frame.

A exhaustive search least squares dipole fitting approach to the inverse problem was implemented to demonstrate the performance of the FVM in the simplest case of single dipole localization. The results obtained from testing the source localization technique on an inhomogeneous spherical volume indicate that the FVM is a valid approach to the forward problem in EEG, for use with any voxel-based inverse algorithm. Dipole localization errors were significantly lower using a higher resolution numerical conductor model. This observation exemplifies the value of a finely discretized head model, which is realizable owing to the polynomial preconditioned CGM algorithm utilized in this research [39]. In the case of the higher resolution volume grid, all displacement errors were less than 3.5 mm, which is adequate for the purpose of locating abnormal brain tissue for surgical removal. Since the accuracy of the FVM with respect to dipole orientation and strength (dipole moment) calculations is also very acceptable, these parameters can offer additional information about the location of epileptogenic foci.

Experiments carried out using scalp potentials simulated with an analytical spherical model to localize dipole sources within a realistic numerical head model showed that head geometry should not be neglected. We confirmed that analytical models of idealistic spherical shape are not sufficient to estimate the source of epileptic activity measured by scalp EEG. Numerical models such as the FVM that can accommodate complex volumetric geometry are necessary to properly represent the conductive properties of a human head.

V. Future Directions

The time required for computation of the FVM source localization method can be further decreased using parallel computing [27]. Generation of lead field data is a repetitive process where a forward solution is calculated for each electrode lead using a single coefficient matrix. The forward solutions could easily be obtained simultaneously by distributing the equations to an array of parallel processors. This would allow source localization results to be available within half a day from the time EEG measurements are recorded and medical images of the patient's head are acquired. Once the LFM is compiled, the speed of source localization will depend entirely on the inverse algorithm used.

All experiments in this research were performed using noise-free data. Actual scalp EEG recordings are always impaired by some amount of recording noise. Regularization is a process performed on systems of equations to suppress the effect of noise in the solution [45]–[47]. Tikhonov regularization, in particular, should be studied in applying the FVM to noisy EEG data.

It has been determined that accurate modeling of bioelectric activity relies heavily on proper specification of tissue conductivities. These values vary not only amongst tissue types, but also from patient to patient [48]. Thus, conductivity values found in literature ([49] for example) are often misleading, if not erroneous. Furthermore, conventional medical imaging does not provide any indication of tissue anisotropy. For clinical application of the FVM to EEG source localization, it may be advantageous to obtain quantitative head conductivity data directly from diffusion tensor MRI (DTI), since it has been reported that conductivity tensors are linearly related to diffusion tensors [28], [50].

Not only would this conductivity data be quantitative and patient-specific, its use would also reduce the dependence on subjective tissue segmentation based on pixel intensities of CT and MR images [51], enhancing the accuracy of the head model overall. However, since the electromagnetic signal for MRI is acquired primarily from the hydrogen proton in water molecules, it is likely that the DTI data would need to be augmented with information from other medical imaging modalities to achieve an adequate representation of some water-deficient tissues such as the skull.

Extensive domain knowledge is available through various functional neuro-imaging tools such as fMRI [12], [52]. It may be useful to exploit a variety of technologies to complement an inverse algorithm. In particular, the localization space can be constrained by a priori knowledge of tissue activation by blood flow, and neuronal orientation in white matter tracts and cortical surfaces [5].

Clearly, electrode configuration has a significant effect on the accuracy of any EEG source localization method [53]–[56]. It has been suggested that the International 10-20 electrode configuration does not provide adequate spatial sampling in the basal region of the head for accurate localization of signals originating from deep sources [1]. Perhaps an ideal recording montage for EEG source localization could be developed and proposed for standard clinical practice in this field.

References

[1] J. S. Ebersole, "Defining epileptogenic foci: past, present, and future," J. Clin. Neurophysiol., vol. 14, pp. 470-483, Nov. 1997.

[2] J. S. Ebersole, "Noninvasive localization of epileptogenic foci by EEG source modeling," Epilepsia, vol. 41 (Suppl. 3), pp. S24-S33, 2000.

[3] F. H. Lopes da Silva, H. J. Wieringa, and M. J. Peters, "Source localization of EEG versus MEG: empirical comparison using visually evoked responses and theoretical considerations," Brain Topogr., vol. 4, pp. 133-142, Winter 1991.

[4] H. Buchner, G. Knoll, M. Fuchs, A. Rienäcker, R. Beckmann, M. Wagner, J. Silny, and J. Pesch, "Inverse localization of electric dipole current sources in finite element models of the human head," Electroencephalogr. Clin. Neurophysiol., vol. 102, pp. 267-278, Apr. 1997.

[5] C. M. Phillips, "Source estimation in EEG – combining anatomical and functional constraints," Sc.A.D thesis, Faculté des Sciences Appliquées, Université de Liège – Liège, 2001.

[6] P. H. Schimpf, C. Ramon, and J. Haueisen, "Dipole models for the EEG and MEG," IEEE Trans. Biomed. Eng., vol. 49, pp. 409-418, May 2002.

[7] Z. J. Koles, J. C. Lind, and A. C. K. Soong, "Spatio-tempral decomposition of the EEG: a general approach to the isolation and localization of sources," Electroencephalogr. Clin. Neurophysiol., vol. 95, pp. 219-230, Oct. 1995.

[8] Z. J. Koles and A. C. K. Soong, "EEG source localization: implementing the spatio-temporal decomposition approach," Electroencephalogr. Clin. Neurophysiol., vol. 107, pp. 343-352, Nov. 1998.

[9] C. Uhl, F. Kruggle, B. Opitz, and D. Yves von Cramon, "A new concept of EEG/MEG signal analysis: detection of interacting spatial modes," Hum. Brain Mapp., vol. 6, pp. 137-149, 1998.

[10] H. M. Huizenga, J. C. de Munck, L. J. Waldorp, and R. P. Grasman, "Spatiotemporal EEG/MEG source analysis based on a parametric noise covariance model," IEEE Trans. Biomed. Eng., vol. 49, pp. 533-539, June 2002.

[11] R. D. Pascual-Marqui, C. M. Michel, and D. Lehmann, "Low resolution electromagnetic tomography: a new method for localizing electrical activity in the brain," Int. J. Psycophysiol., vol. 18, pp. 49-65, Oct. 1994.

[12] Z. J. Koles ZJ, "Trends in EEG source localization," Electroencephalogr. Clin. Neurophysiol., vol. 106, pp. 127-137, Feb. 1998.

[13] G. Marin, C. Guerin, S. Baillet, L. Garnero, and G. Meunier, "Influence of skull anisotropy for the forward and inverse problem in EEG: simulation studies using FEM on realistic head models," Hum. Brain Mapp., vol. 6, pp. 250-269, 1998.

[14] B. J. Roth, M. Balish, A. Gorbach, and S. Sato, "How well does a three-sphere model predict positions of dipoles in a realistically shaped head?", Electroencephalogr. Clin. Neurophysiol., vol. 87, pp. 175-184, Oct. 1993.

[15] B. N. Cuffin, D. L. Schomer, J. R. Ives, and H. Blume, "Experimental tests of EEG source localization accuracy in spherical head models," Clin. Neurophysiol., vol. 112, pp. 46-51, Jan. 2001.

[16] R. J. Sclabassi, M. Sonmez, and M. Sun, "EEG source localization: a neural network approach," Neurol. Res., vol. 23, pp. 457-464, July 2001.

[17] T. Krings, K. H. Chiappa, B. N. Cuffin, J. I. Cochius, S. Connolly, and G. R. Cosgrove, "Accuracy of EEG dipole source localization using implanted sources in the human brain," Clin. Neurophysiol., vol. 110:106, pp. 106-114, Jan. 1999.

[18] V. L. Towle, R. Cakmur, Y. Cao, M. Brigell, and L. Parmeggiani, "Locating VEP equivalent dipoles in magnetic resonance images," Int. J. Neurosci., vol. 80, pp. 105-116, 1995.

[19] M. Hämäläinen, "Anatomical correlates for magnetoencephalography: integration with magnetic resonance images," Clin. Phys. Physiol. Meas., vol. 12 (Suppl. A), pp. 29-32, 1991.

[20] L. Spinelli, S. G. Andino, G. Lantz, M. Seeck, and C. M. Michel, "Electromagnetic inverse solutions in anatomically constrained spherical head models," Brain Topogr., vol. 13, pp. 115-25, Winter 2000.

[21] B. N. Cuffin, D. L. Schomer, J. R. Ives, and H. Blume, "Experimental tests of EEG source localization accuracy in realistically shaped head models," Clin. Neurophysiol., vol. 112, pp. 2288-2292, Dec. 2001.

[22] M. Fuchs, M. Wagner, and J. Kastner, "Boundary element method volume conductor models for source reconstruction," Clin. Neurophysiol., vol. 112, pp. 1400-1407, Aug. 2001.

[23] S. Abboud, Y. Eshel, S. Levy, and M. Rosenfeld, "Numerical calculation of the potential distribution due to dipole sources in a spherical model of the head, "Comput. Biomed. Res., vol. 27, pp. 441-455, Dec. 1994.

[24] V. E. Agapov, "Numerical solution of the forward problem in electroencephalography," Ph.D. thesis, Department of Mathematical Sciences, University of Alberta – Edmonton, 2001.

[25] K. A. Awada, D. R. Jackson, J. T. Williams, D. R. Wilton, S. B. Baumann, and A. C. Papanicolaou, "Computational aspects of finite element modeling in EEG source localization," IEEE Trans. Biomed. Eng., vol. 44, pp. 736-752, Aug. 1997.

[26] M. Rosenfeld, R. Tanami, and S. Abboud, "Numerical solution of the potential due to sources in volume conductors with arbitrary geometry and conductivity," IEEE Trans. Biomed. Eng., vol. 43, pp. 679-689, July 1996.

[27] L. Lemieux, A. McBride, and J. W. Hand, "Calculation of electrical potentials on the surface of a realistic head model by finite differences," Phys. Med. Biol., vol. 41, pp. 1079-1091, July 1996.

[28] D. S. Tuch, V. J. Wedeen, A. M. Dale, J. S. George, and J. W. Belliveau, "Conductivity tensor mapping of the human brain using tensor MRI," Proc. Natl. Acad. Sci. U. S. A., vol. 98, pp. 11697-11701, Sept. 2001.

[29] J. Haueisen, D. S. Tuch, C. Ramon, P. H. Schimpf, V. J. Wedeen, J. S. George, and J. W. Belliveau, "The influence of brain tissue anisotropy on human EEG and MEG," Neuroimage vol. 15, pp. 159-166, Jan. 2002.

[30] S. P. Van den Broek, F, Reinders, M. Donderwinkel, and M. J. Peters, "Volume conduction effects in EEG and MEG," Electroencephalogr. Clin. Neurophysiol., vol. 106, pp. 522-534, June 1998.

[31] B. Vanrumste, G. Van Hoey, R. Van de Walle, M. R. D'Havé, I. A. Lemahieu, and P. A. Boon PA, "The Validation of the Finite Difference Method and Reciprocity for Solving the Inverse Problem in EEG Dipole Source Analysis," Brain Topogr., vol. 14, pp. 83-92, Winter 2001.

[32] H. I. Saleheen and K. T. Ng, "New finite difference formulations for general inhomogeneous anisotropic bioelectric problems," IEEE Trans. Biomed. Eng., vol. 44, pp. 800-809, Sept. 1997.

[33] P. Laarne, H. Eskola, J. Hyttinen, V. Suihko, and J. Malmivuo, "Validation of a detailed computer model for the electric fields in the brain," J. Med. Eng. Technol., vol. 19, pp. 84-87, Mar.-June 1995.

[34] P. Laarne, J. Hyttinen, S. Dodel, J. Malmivuo, and H. Eskola, "Accuracy of two dipolar inverse algorithms applying reciprocity for forward calculation," Comput. Biomed. Res., vol. 33, pp. 172-185, June 2000.

[35] P. Kauppinen, J. Hyttinen, P. Laarne, and J. Malmivuo, "A software implementation for detailed volume conductor modeling in electrophysiology using finite difference method," Comput. Methods Programs Biomed., vol. 58, pp. 191-203, Feb. 1999.

[36] Z. J. Koles, P. Flor-Henry, and J. C. Lind, "Low-resolution electrical tomography of the brain during psychometrically matched verbal and spatial cognitive tasks," Hum. Brain Mapp., vol. 12, pp. 144-156, Mar. 2001.

[37] G. A. Worrell, T. D. Lagerlund, F. W. Sharbrough, B. H. Brinkmann, N. E. Busacker, K. M. Cicora, and T. J. O'Brien, "Localization of the epileptic focus by low-resolution electromagnetic tomography in patients with a lesion demonstrated by MRI," Brain Topogr., vol. 12, pp. 273-282, Summer 2000.

[38] I. F. Gorodnitsky, J. S. George, and B. D. Rao, "Neuromagnetic source imaging with FOCUSS: a recursive weighted minimum norm algorithm," Electroencephalogr. Clin. Neurophysiol., vol. 95, pp. 231-251, Oct. 1995.

[39] L. A. Neilson, "Anisotropic Expansion of the Finite Volume Method – Application of Diffusion Tensor Imaging to Realistic Head Modeling for EEG Source Localization," University of Alberta – Edmonton, 2003.

[40] Y. Saad, *Iterative Methods for Sparse Linear Systems*. Boston, MA: PWS-Kent., 1996.

[41] L. A. Neilson, Z. J. Koles, M. Kovalyov, "Accelerated forward solution of a high resolution volume conductor model by Chebyshev polynomial preconditioning," University of Alberta – Edmonton, 2003.

[42] D. Weinstein, L. Zhukov, and C. Johnson, "Lead-field bases for electroencephalography source imaging," Ann. Biomed. Eng., vol. 28, pp.1059-1065, Sept. 2000.

[43] J. C. Mosher, S. Baillet, and R. M. Leahy, "EEG source localization and imaging using multiple signal classification approaches," J. Clin. Neurophysiol., vol. 16, pp. 225-238, May 1999.

[44] J. C. Mosher and R. M. Leahy, "Recursive MUSIC: a framework for EEG and MEG source localization," IEEE Trans. Biomed. Eng., vol. 45, pp. 1342-1354, Nov. 1998.

[45] I.F. Gorodnitsky, B. D. Rao, "Analysis of error produced by truncated SVD and Tikhonov regularization methods," Asilomar Conference on Signals, Systems, and Computers – Computer Society Press of the IEEE, pp. 25-29, 1995.

[46] A. Sano, "Optimally regularized inverse of singular value decomposition and application to signal extrapolation," Signal Processing, vol. 30, pp. 163-76, 1993.

[47] G. Wahba, 'Spline interpolation and smoothing on the sphere," SIAM J. Sci. Stat. Comput., vol. 2, pp. 5-16, 1981.

[48] P. Laarne, P. Kauppinen, P. Hyttinen, J. Malmivuo, and H. Eskola, "Effects of tissue resistivities on electroencephalogram sensitivity distribution," Med. Biol. Eng. Comput., vol. 37, pp. 555-559, Sept. 1999.

[49] L. A. Geddes, L. E. Baker, "The specific resistance of biological material – a compendium of data for the biomedical engineer and physiologist," Med. Biol. Eng. Comput., vol. 5, pp. 271-293, May 1967.

[50] M. M. Bahn, "A linear relationship exists among brain diffusion eigenvalues measured by diffusion tensor magnetic resonance imaging," J. Magn. Reson., vol. 137, pp. 33-38, Mar. 1999.

[51] M. Cercignani, M. Inglese, M. Siger-Zajdel, M. Filippi, "Segmenting brain white matter, gray matter and cerebro-spinal fluid using diffusion tensor-MRI derived indices," Magn. Reson. Imaging, vol. 19, pp. 1167-1172, Nov. 2001.

[52] M. Wagner and M. Fuchs, "Integration of functional MRI, structural MRI, EEG, and MEG," Hamburg: Neuroscan Labs, 2001.

[53] B. N. Cuffin, "Effects of modeling errors and EEG measurement montage on source localization accuracy," J. Clin. Neurophysiol., vol. 18, pp. 37-44, Jan. 2001.

[54] P. H. Laarne, M. L. Tenhunen-Eskelinen, J. K. Hyttinen, and H. J. Eskola, "Effect of EEG electrode density on dipole localization accuracy using two realistically shaped skull resistivity models," Brain Topogr., vol. 12, pp. 249-254, Summer 2000.

[55] G. H. Klem, H. O. Lüders, H. H. Jasper, and C. Elger, "The ten-twenty electrode system of the International Federation," Electroencephalogr. Clin. Neurophysiol. Suppl., vol. 52, pp. 3-6, 1999.

[56] K. B. E. Böcker, J. A. G. van Avermaete, M. M. C. van den Beg-Lenssen, "The international 10-20 system revisited: cartesian and spherical co-ordinates," Brain Topogr., vol. 6, pp. 231-235, 1994.

CHAPTER 2

ANISOTROPIC EXPANSION OF THE FINITE VOLUME METHOD AND QUANTITIFYING TISSUE CONDUCTIVITIES BY DIFFUSION TENSOR IMAGING

I. Introduction

A. EEG Source Localization

Electroencephalographic (EEG) recordings are routinely obtained from patients who exhibit brain disorders such as epilepsy. The bioelectric signals measured by EEG are a result of coherent activation of pyramidal cells in the cortex. In focal epilepsy, seizures originate from abnormal electrical activity in a small region of brain tissue known as the epileptogenic focus [1], then propagate throughout the head. Surgeons would like to know the exact location of the source so that the aberrant tissue can be removed, and the patient cured. Presently, clinical EEG source localization is a hit and miss procedure. Often, the affected region of the brain is identified by a series of cognitive tests, along with functional and anatomical imaging. Sometimes depth electrodes are used to pinpoint the source of electrical disturbance. This intracranial recording technique is extremely invasive and ineffective in some cases. It is therefore important to investigate alternative solutions to the problem of EEG source localization.

In the past half century, much research has been done in the area of epileptic source localization via EEG. There are some inferential techniques that involve visual inspection of EEG time series or scalp voltage topography. These methods are widely used in clinical settings, but they provide only a rough indication of the nature of epileptic activity exhibited by a patient. Unquestionably there is a need for a more definitive approach to uncovering the valuable diagnostic information embedded in EEG

data. Any such procedure necessarily requires the use of a model to approximate the conductive medium (the head) through which the biological signal propagates.

The earliest and most simple head models developed for EEG source localization were analytically-derived spherical volume conductors. These days, it is widely agreed that any spherical model is too simplistic to accurately locate epileptogenic foci [1]-[3]. Increased accessibility of efficient and affordable computing has borne a widespread pursuit of more realistic, numerical head models.

B. The Finite Volume Method

The Finite Volume Method (FVM) is a numerical technique used to model current flow through an inhomogeneous medium by building a mathematical description of the volume as an assemblage of many hexahedral volume elements (voxels). For bioelectric problems, a quasistatic approximation is adopted where it is assumed that signal frequencies are low, and the capacitive properties of tissues can be safely neglected [4]. Applying equations that govern electrostatic phenomena discretely to each voxel yields a system of equations that describe the relationship between volume current density and potential distribution throughout an inhomogeneous volume conductor of arbitrarily complex geometry.

Other numerical formulations that apply the same principles are the Finite Difference Method (FDM) and the Finite Element Method (FEM). The FDM is based on a (sometimes isotropic) rectangular framework where nodes are assigned to the vertices of every cell. Potentials at discrete points throughout the volume are estimated by applying Poisson's equation to each node, for example in Cartesian coordinate form:

$$\nabla \cdot (\acute{o} \nabla \phi) = \acute{o} \left(\frac{\partial^2 \phi}{\partial x^2} + \frac{\partial^2 \phi}{\partial y^2} + \frac{\partial^2 \phi}{\partial z^2} \right) = -I_v(x, y, z), \quad (1)$$

where σ is tissue conductivity (per unit length), ψ is potential distribution, and I_v is the source current density in the conductor [5]-[7].

Discretization of (1) involves expanding a Taylor series, which must be truncated at second-order to arrive at a linear difference equation. As a result, Poisson's equation is not exactly satisfied over the entire domain of solution. That is, at voxel interfaces where conductivities vary by more than one order of magnitude (such as skull – soft tissue barriers), the derivative of potential is discontinuous and the discrete approximation of (1) deviates significantly from the ideal, leading to large errors in calculated potentials at those nodes [7]-[9].

Alternatively, with the FVM, nodes are assigned to cell centres, rather than their vertices. Poisson's equation is modified by taking a volume integral on each side,

$$\int_V \nabla \cdot (\acute{o} \nabla \phi) dV = -\int_V I_v dV . \quad (2)$$

By the Divergence theorem, (2) is rewritten as Gauss' Law (*the total outward electric flux over any closed surface is equal to the total free charge enclosed in the surface* [10]),

$$\oint_S (-\acute{o} \nabla \phi) \cdot d\mathbf{S} = \int_V I_v dV . \quad (3)$$

The potential at the centre point of each homogeneous voxel is defined by (3), where **S** is the surface area vector and V is the cell volume [9]. Furthermore, the volume conductor as a whole is subject to a Neumann boundary condition. Namely, current cannot flow into or out of the volume from the surrounding air, or

$$\acute{o} \frac{\partial \phi}{\partial n} = 0. \quad (4)$$

where, n is a direction normal to the volume surface [9]. Discretization of the integrals in (3) separates the hexahedron surface **S** into its six constituent faces, giving

$$\begin{aligned}\left(\acute{o}\nabla\phi\cdot\mathbf{S}^{\xi}\right)_{i-\frac{1}{2}}-\left(\acute{o}\nabla\phi\cdot\mathbf{S}^{\xi}\right)_{i+\frac{1}{2}}+\left(\acute{o}\nabla\phi\cdot\mathbf{S}^{\eta}\right)_{j-\frac{1}{2}}-\left(\acute{o}\nabla\phi\cdot\mathbf{S}^{\eta}\right)_{j+\frac{1}{2}}+\\ \left(\acute{o}\nabla\phi\cdot\mathbf{S}^{\zeta}\right)_{k-\frac{1}{2}}-\left(\acute{o}\nabla\phi\cdot\mathbf{S}^{\zeta}\right)_{k+\frac{1}{2}}=I_{v}V,\end{aligned} \tag{5}$$

where $\mathbf{S}^{\xi}$, $\mathbf{S}^{\eta}$, $\mathbf{S}^{\zeta}$ are the 3 orthonormal face area vectors, and $i\pm\frac{1}{2}$, $j\pm\frac{1}{2}$, $k\pm\frac{1}{2}$ are indices to represent the six faces through which current flows *out of* the voxel (see Figure 2-1).

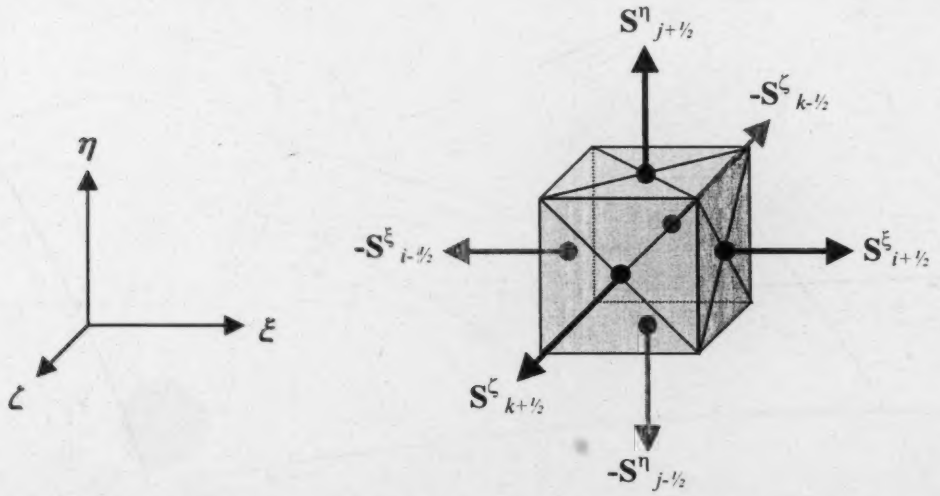

Figure 2-1: Orthonormal cell face area vectors $\mathbf{S}^{\ell}$. The six faces indices $i\pm\frac{1}{2}$, $j\pm\frac{1}{2}$, $k\pm\frac{1}{2}$ indicated in (5) are labeled, where the centre point of the cell is (i, j, k). Note that the face area vectors $\mathbf{S}^{\ell}$ are defined for any hexehedron in an orthogonal coordinate system.

The FVM uses an integral definition to describe the potential gradient, $\nabla\psi$, across a closed surface as

$$\nabla\phi=\frac{1}{V}\oint_{S}\phi\, d\mathbf{S} \tag{6}$$

Discretizing (6) does not suffer from series truncation errors at severe tissue discontinuities, as in the case of the finite difference formulation [9].

$$\nabla \phi = \frac{1}{V} \sum_{\ell} \phi_{\ell} \mathbf{S}^{\ell} \tag{7}$$

is the discrete version of (6) that describes the potential gradient at the centre of a cell, where ϕ_{ℓ} are the potentials at the middle of each cell face, and $\mathbf{S}^{\ell}$ are the six face area vectors. A full development of the FVM for isotropic tissues is outlined in [9]. The details of this method, and its expansion to incorporate generalized tissue anisotropy are discussed in Section II-A.

It should be noted that some investigators of bioelectric inverse modeling employ an approach that combines features of both FDM and FVM [11]. Starting with Poisson's equation (1), defining the nodes to be at the centre of each voxel, and imposing the necessary boundary conditions, the differential equation is transformed into a linear difference equation by "box integration". In effect, this process yields the same system of equations as FVM, though the method is usually referred to as FDM since its development begins in the differential form.

The FEM too, reduces Poisson's equation to a linear system, but employs an irregular volume element mesh with homogeneous cells of various shapes and sizes, and calculates discrete potentials at the cell vertices (nodes). Potential distributions and current densities *within* each cell can be described using assigned interpolation functions (usually linear or quadratic) [12], [13]. All three formulations (FEM, FDM, and FVM) produce a linear system of equations whose coefficient matrix is sparse and solvable by iterative methods.

Rosenfeld et al., [9], develop the FVM within a generalized curvilinear coordinate system. In the present work, however, the voxel framework is defined to be Cartesian,

with strictly cubic volume elements. There are two reasons for this choice. First, the use of non-rectangular voxels introduces singularities into the equations where cell faces degenerate to a line or point. These singularities can be removed by adding more equations and unknowns to the system [9], but their existence complicates the volume decomposition algorithm. Secondly, and more importantly, in the context of a cubic grid, the qualitative (tissue type) or quantitative (conductivity, in this case) properties of each voxel can be extracted directly from the pixels of medical images. Thus, volume decomposition can be performed directly after volumetric image data has been acquired from the patient. There is no need to develop a geometrically complicated model framework, as is the case with FEM [5], [12]. Also, since abrupt changes in tissue conductivity are taken care of by the integral formulation of Gauss' Law (3), mesh refinement at critical tissue interfaces need not be performed, as is sometimes done to improve the accuracy of the FDM. In fact, the spatial resolution of a FVM conductor model is limited only by the spatial resolution of the medical images from which it is derived.

Recognizing that a uniform distribution of nodes throughout the conductor volume may introduce computational inefficiency in large regions of homogeneous tissue, we assert that the advantages of the FVM – accommodation of abrupt conductivity changes and unsupervised volume decomposition – outweigh the disadvantage of including more variables in the linear system. This is especially true in light of our highly efficient solution method (see Section II-D), and the fact that the abundant processing capacity of modern workstations continues to become increasingly affordable.

C. Anisotropic Conductivity

As indicated in the previous section, realistic numerical modeling of bioelectric conductors is based on patient-specific medical images. In this work, high resolution details about the geometry and tissue distribution of the head are extracted by translating pixels from MR images directly into discrete volume elements. Conventionally, anatomical images are segmented by pixel intensity, and each group of voxels is identified as a particular tissue type. MRI is the best modality for outlining the structure and distribution of soft tissue, but X-ray computed tomography (CT) is often used to delineate the bone structure in the face and skull. Then all the voxels of a given type are assigned an isotropic conductivity based on published data [6], [14]. However, the inherent inaccuracies of image segmentation procedures, and the individual variability of tissue conductivities guarantee that the numerical representation of any inhomogeneous conductor will suffer from some degree of error. It has been determined experimentally that any enhancement of source localization accuracy gained by developing a realistic head model may be nullified by incorporating incorrect tissue conductivities [6], [15].

Besides providing little quantitative information about tissue conductivity, conventional medical images give no indication of tissue anisotropy. Since some tissue, such as white matter, is known to be highly anisotropic [16], [17], any numerical construction that assumes isotropic volume elements is likely to suffer from significant modeling error [18], [19]. Fortunately, a recent advance in NMR technology provides a solution to the problem of assigning accurate conductive properties to bioelectric models.

Diffusion weighted imaging (DWI) is a NMR paradigm that quantifies the net diffusive movement of water molecules over time through pixels defined by the imaging

sequence. DWI can only measure macroscopic diffusion in one direction specified by the application of a diffusion gradient incorporated into the NMR experiment. By repeating DWI on the same sample with 6 independent gradient directions, and once more without the diffusion gradient, a diffusion tensor **D** is constructed for each pixel [20], [21]. This process is known as diffusion tensor imaging (DTI).

The water self-diffusion tensor is a 3 by 3 matrix whose diagonal elements represent diffusivity in three orthogonal directions, based on a global frame of reference. The off-diagonal elements are indicative of diffusion coupling between the main axis directions. In general, diffusion tensors are non-symmetric, but in the case of uncharged media such as water, the curl of the diffusivity is zero,

$$curl(\mathbf{D}) = \nabla \times \mathbf{D} = \nabla \times \begin{bmatrix} Dxx & Dxy & Dxz \\ Dxy & Dyy & Dyz \\ Dxz & Dyz & Dzz \end{bmatrix} = 0 . \tag{8}$$

Intuitively, the rate of diffusion of a sample of molecules subject to zero-curl diffusivity may vary with direction, but the molecules spread out such that their net movement in any direction is a straight line. In other words, a sample of molecules under these conditions experiences no net circulation. Mathematically, a diffusion tensor with zero curl is symmetric [18], [21], meaning that the three principal diffusion directions (tensor eigenvectors) are mutually orthogonal. Therefore, **D** includes only six unique values, underlying the fact that only six (as opposed to nine) diffusion weighted scans are required to construct the DTI in one imaging plane.

It has been suggested that on a macroscopic scale, tissue conductivity bears a strong linear relationship to the diffusivity of water through the same medium. This is supported by the notion that although the two processes are fundamentally unrelated, on a

voxel scale, the net displacement of water molecules and cellular ions are both mediated by the geometry of the extracellular space. That is, barriers presented by cell membranes cause both water and ions to diffuse preferentially in line with tissue microstructure. An approximate linear relationship between the diffusion tensor, **D** (area per time), and the conductivity tensor, $\boldsymbol{\sigma}$ (conductivity per length), is

$$\boldsymbol{\sigma} = \frac{\sigma_e}{d_e}\mathbf{D}, \tag{9}$$

where σ_e and d_e are effective extracellular conductivity and diffusivity scalars, respectively [18], and their ratio has units of conductivity· time per volume. The linear approximation (9) assumes that intracellular conductivity and diffusivity are negligible. In fact, the exact association between $\boldsymbol{\sigma}$ and **D** is a fractional linear relationship. Details of the effective medium model, which infers tissue conductivity tensors from water self-diffusion tensors, is available in [16] where the theory has been borne out by experiment. In effect, DTI provides a quantitative and patient-specific measure of anisotropic conductivity throughout the biological volume to be modeled.

Anisotropic conductivity can be incorporated into the FEM by assigning one tensor to each volume element [18], [19], [22]. However, it is a significant challenge to allocate the tensors – which are given in a Cartesian grid due to DTI acquisition – to FEM cells of various shapes, sizes, and orientations. In keeping with the motivation to translate patient-specific images directly into a numerical volume decomposition algorithm without rearranging the geometry of the available data, it is preferable to employ a method that uses a rectangular framework.

Both the FVM and FDM can accommodate a specific form of tissue anisotropy without increasing the complexity of the decomposition algorithm or adding new variables to the resulting system of equations [5], [6]. However, in both cases, only diagonal conductivity tensors (orthotropic anisotropy – all tensor eigenvectors have globally fixed perpendicular directions) can be handled. In Cartesian coordinates, for example, it is a trivial matter to assign distinct x, y, and z conductivity values to each voxel, but neither method allows for conductive coupling between the three global axes.

Generalized anisotropic conductivity, however, refers to a situation where there is conductive coupling between global axes, and the conductivity tensor is symmetric, but not necessarily diagonal. Principal conductivity directions (tensor eigenvectors) at every voxel, along with their respective magnitudes (tensor eigenvalues) dictate the flow of current through the volume. Thus, all six values in each symmetric conductivity tensor are theoretically important to the EEG source localization problem. Other investigators have successfully expanded the FDM to allow for generalized anisotropic conductivities [7], [23], but ultimately this formulation still suffers from inaccuracy at drastic tissue interfaces. Therefore, the next section describes in detail the expansion of the FVM to incorporate full conductivity tensors at every voxel in the volume conductor model.

II. Methods

A. Development of the Expanded Finite Volume Method

The development of the expanded FVM (EFVM) follows arguments laid out for the discussion of FVM in [9]. From (5) it is clear that the volume currents flowing outward through every face of a hexahedron are defined with respect to the potential gradient at

the centre of the face. These fluxes sum to total the magnitude of the current source (or sink) located in that cell, which is just the source current density in that cell multiplied by the cell volume ($J_v V = I$). The task then is to characterize the discrete potential gradient, $\nabla\psi$, at the middle of each cell face. Consider (7), which describes $\nabla\psi$ at the centre point of a cell based on discrete potentials at every face. Apply this definition to a "secondary" cell (a theoretical construction solely for the purpose of method development) whose centre is the midpoint of the "primary" cell face $(i+½)_p$ (see Figure 2-2). Expanding (7) and applying it to the centre of the secondary cell,

$$\nabla\boldsymbol{\phi}_s = \nabla\boldsymbol{\phi}_{p,I+½} = \frac{1}{V_s}\begin{Bmatrix} \left(\boldsymbol{\phi}\mathbf{S}^i\right)_{s,I+½} - \left(\boldsymbol{\phi}\mathbf{S}^i\right)_{s,I-½} + \\ \left(\boldsymbol{\phi}\mathbf{S}^c\right)_{s,J+½} - \left(\boldsymbol{\phi}\mathbf{S}^c\right)_{s,J-½} + \\ \left(\boldsymbol{\phi}\mathbf{S}^\delta\right)_{s,K+½} - \left(\boldsymbol{\phi}\mathbf{S}^\delta\right)_{s,K-½} \end{Bmatrix}, \qquad (10)$$

gives an expression for $\nabla\psi$ on the $i+½$ face of the primary cell, where the ψ_s are the potentials at the six faces of the secondary cell.

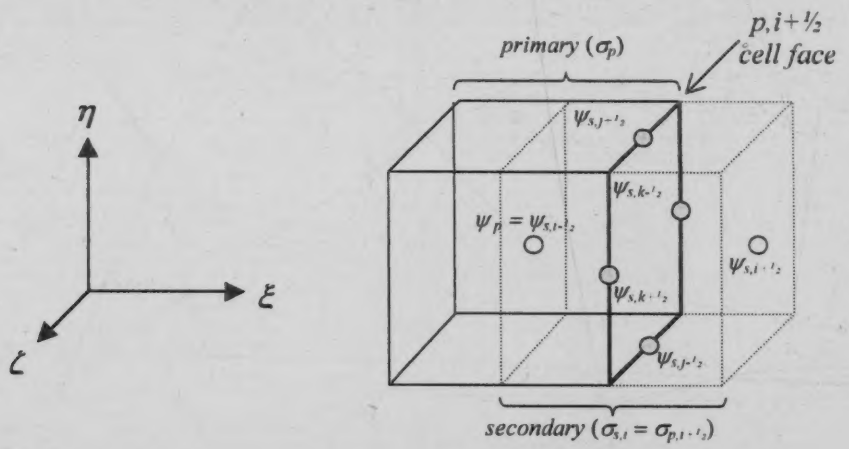

Figure 2-2: Primary and secondary cell configuration. The two cells overlap by half a voxel such that the centre point of the secondary cell volume is the $i+½$ face of the primary cell. The potential, ψ_s, at all six faces of the secondary cell are used to calculate the potential gradient across the $i+½$ face of the primary cell (bold outline), $\nabla\psi_{p,i+½}$ according to (10). Note that the primary-secondary cell relationship is valid for any hexahedron in an orthogonal coordinate system.

The conductivity at the $i+½$ face of the primary cell, $\sigma_{p,i+½}$, is the conductivity of the secondary cell, σ_s, which is some combination of conductivities of its two constituent half-voxels called *effective conductivity*, to be defined later. Then according to (5) and (10) the flux outward through the $i+½$ face of the primary cell is

$$\left(\acute{o}\nabla\acute{o}\cdot\mathbf{S}^i\right)_{p,i+½} = \frac{\acute{o}_s}{V_s}\left\{\begin{matrix}\left(\acute{o}\mathbf{S}^i\right)_{s,i+½} - \left(\acute{o}\mathbf{S}^i\right)_{s,j-½} + \\ \left(\acute{o}\mathbf{S}^c\right)_{s,j+½} - \left(\acute{o}\mathbf{S}^c\right)_{s,j-½} + \\ \left(\acute{o}\mathbf{S}^{\acute{o}}\right)_{s,k+½} - \left(\acute{o}\mathbf{S}^{\acute{o}}\right)_{s,k-½}\end{matrix}\right\}\cdot\mathbf{S}^i_{p,i+½}. \qquad (11)$$

Similar equations describe the flux into the other five faces of the primary voxel. Each definition can be developed using a secondary cell centred on the face of interest.

In Section I-B it was mentioned that we have chosen to implement the FVM (and EFVM) in a Cartesian framework, where the voxel widths are equal in all three dimensions (called x, y, and z). The centre point of every voxel is called a *node*

(illustrated with white circles in all figures). Say the side length of every voxel is h. Then all cell volumes $V = h^3$, and face areas $S = h^2$ are constant over the entire domain. The three orthonormal face area vectors are in turn

$$\mathbf{S}^x = \begin{bmatrix} h^2 \\ 0 \\ 0 \end{bmatrix}, \quad \mathbf{S}^y = \begin{bmatrix} 0 \\ h^2 \\ 0 \end{bmatrix}, \quad \mathbf{S}^z = \begin{bmatrix} 0 \\ 0 \\ h^2 \end{bmatrix}. \tag{12}$$

In order to expand the FVM for generally anisotropic media, the previously scalar voxel conductivity, σ, is treated as a symmetric tensor such that

$$\acute{\mathbf{o}} = \begin{bmatrix} \acute{o}^{xx} & \acute{o}^{xy} & \acute{o}^{xz} \\ \acute{o}^{xy} & \acute{o}^{yy} & \acute{o}^{yz} \\ \acute{o}^{xz} & \acute{o}^{yz} & \acute{o}^{zz} \end{bmatrix}. \tag{13}$$

The values of the voxel tensor diagonal represent conductivities along the global Cartesian axes. The off-diagonal elements account for conductive coupling between any two dimensions. Therefore, the tensor quantifies anisotropic tissue conductivity of arbitrary orientation. However, since it is symmetric, tensor eigenvectors are necessarily orthogonal.

Applying (12) and (13) to (11) yields

$$\left(\acute{\mathbf{o}}\nabla\acute{\mathrm{o}}\cdot\mathbf{S}^x\right)_{p,i+\frac{1}{2}} = \frac{1}{h^3}\begin{bmatrix} \acute{o}^{xx} & \acute{o}^{xy} & \acute{o}^{xz} \\ \acute{o}^{xy} & \acute{o}^{yy} & \acute{o}^{yz} \\ \acute{o}^{xz} & \acute{o}^{yz} & \acute{o}^{zz} \end{bmatrix}_s \left\{ \begin{bmatrix} \left(\acute{\mathrm{o}}_{s,i+\frac{1}{2}} - \acute{\mathrm{o}}_{s,i-\frac{1}{2}}\right)\begin{bmatrix} h^2 \\ 0 \\ 0 \end{bmatrix} + \\ \left(\acute{\mathrm{o}}_{s,j+\frac{1}{2}} - \acute{\mathrm{o}}_{s,j-\frac{1}{2}}\right)\begin{bmatrix} 0 \\ h^2 \\ 0 \end{bmatrix} + \\ \left(\acute{\mathrm{o}}_{s,k+\frac{1}{2}} - \acute{\mathrm{o}}_{s,k-\frac{1}{2}}\right)\begin{bmatrix} 0 \\ 0 \\ h^2 \end{bmatrix} \end{bmatrix} \cdot \begin{bmatrix} h^2 \\ 0 \\ 0 \end{bmatrix} \right\}. \tag{14}$$

Then

$$\left(\acute{\mathbf{o}}\nabla\acute{\mathbf{o}}\cdot\mathbf{S}^{x}\right)_{p,j+\frac{1}{2}}=\frac{1}{h^{3}}\left\{\begin{array}{l}\left(\acute{\mathbf{o}}_{s,j+\frac{1}{2}}-\acute{\mathbf{o}}_{s,j-\frac{1}{2}}\right)\begin{bmatrix}h^{2}\acute{o}^{xx}\\h^{2}\acute{o}^{xy}\\h^{2}\acute{o}^{xz}\end{bmatrix}_{s}\\+\left(\acute{\mathbf{o}}_{s,j+\frac{1}{2}}-\acute{\mathbf{o}}_{s,j-\frac{1}{2}}\right)\begin{bmatrix}h^{2}\acute{o}^{xy}\\h^{2}\acute{o}^{yy}\\h^{2}\acute{o}^{yz}\end{bmatrix}_{s}\\+\left(\acute{\mathbf{o}}_{s,k+\frac{1}{2}}-\acute{\mathbf{o}}_{s,k-\frac{1}{2}}\right)\begin{bmatrix}h^{2}\acute{o}^{xz}\\h^{2}\acute{o}^{yz}\\h^{2}\acute{o}^{zz}\end{bmatrix}_{s}\end{array}\right\}\cdot\begin{bmatrix}h^{2}\\0\\0\end{bmatrix}. \qquad (15)$$

Therefore,

$$\left(\acute{\mathbf{o}}\nabla\acute{\mathbf{o}}\cdot\mathbf{S}^{x}\right)_{p,j+\frac{1}{2}}=h\left[\acute{o}_{s}^{xx}\left(\acute{\mathbf{o}}_{s,j+\frac{1}{2}}-\acute{\mathbf{o}}_{s,j-\frac{1}{2}}\right)+\acute{o}_{s}^{xy}\left(\acute{\mathbf{o}}_{s,j+\frac{1}{2}}-\acute{\mathbf{o}}_{s,j-\frac{1}{2}}\right)+\acute{o}_{s}^{xz}\left(\acute{\mathbf{o}}_{s,k+\frac{1}{2}}-\acute{\mathbf{o}}_{s,k-\frac{1}{2}}\right)\right], \qquad (16)$$

flux out of one face of a primary voxel is defined by a linear combination of discrete potentials at all six faces of the overlapping secondary voxel. The three coefficients of this linear equation are elements of what we call the *effective conductivity vector* of the secondary cell face. ($\acute{\mathbf{o}}_{s,j}^{x}=\acute{\mathbf{o}}_{p,j+\frac{1}{2}}^{x}$ in this case for flux through the $i+\frac{1}{2}$ primary cell face, which flows in the x direction.) This vector contains one *principal effective conductivity* value, $\acute{\mathbf{o}}_{s,j}^{xx}$, and two *coupled effective conductivity* values, $\acute{\mathbf{o}}_{s,j}^{xy}$ and $\acute{\mathbf{o}}_{s,j}^{xz}$. Different effective conductivity vectors are defined for each face of a primary voxel. For example, $\acute{\mathbf{o}}_{p,j+\frac{1}{2}}^{y}$ and $\acute{\mathbf{o}}_{p,k+\frac{1}{2}}^{z}$ would be the effective conductivity vectors for the $j+\frac{1}{2}$ and $k+\frac{1}{2}$ primary cell faces, respectively.

Abandoning the notion of primary and secondary cells for the time being, the conductivity tensor of any primary voxel is now marked by i, j, k subscripts, such as $\sigma_{i,j,k}$.

The effective conductivity vector associated with a voxel face is identified by subscripts of the two cells that share the face of interest. For example, the face shared by voxels (*i, j, k*) and (*i+1, j, k*) has effective conductivity vector $\acute{\mathbf{o}}^{x}_{i+\frac{1}{2},j,k}$. Rewriting (5) in the context of a Cartesian framework, with effective conductivity *vectors* indexed to indicate the distinct conductive properties of each face, and recalling that total source current $I_v V = I$, we have

$$\begin{aligned}\left(\acute{\mathbf{o}}^{x}\nabla\acute{\mathrm{o}}\cdot\mathbf{S}^{x}\right)_{i-\frac{1}{2},j,k}-\left(\acute{\mathbf{o}}^{x}\nabla\acute{\mathrm{o}}\cdot\mathbf{S}^{x}\right)_{i+\frac{1}{2},j,k}+\left(\acute{\mathbf{o}}^{y}\nabla\acute{\mathrm{o}}\cdot\mathbf{S}^{y}\right)_{i,j-\frac{1}{2},k}-\left(\acute{\mathbf{o}}^{y}\nabla\acute{\mathrm{o}}\cdot\mathbf{S}^{y}\right)_{i,j+\frac{1}{2},k}+\\ \left(\acute{\mathbf{o}}^{z}\nabla\acute{\mathrm{o}}\cdot\mathbf{S}^{z}\right)_{i,j,k-\frac{1}{2}}-\left(\acute{\mathbf{o}}^{z}\nabla\acute{\mathrm{o}}\cdot\mathbf{S}^{z}\right)_{i,j,k+\frac{1}{2}}=I_{i,j,k},\end{aligned} \tag{17}$$

which describes the flux out of voxel (*i, j, k*) through its six faces. Adhering to the form of (16), the expanded expression for the second term of (17), flux through face (*i+½, j, k*) is

$$\left(\acute{\mathbf{o}}^{x}\nabla\acute{\mathrm{o}}\cdot\mathbf{S}^{x}\right)_{i+\frac{1}{2},j,k}=h\left\{\begin{array}{l}\acute{o}^{xx}_{i+\frac{1}{2},j,k}\left(\acute{\mathrm{o}}_{i+1}-\acute{\mathrm{o}}_{i}\right)_{j,k}+\\ \acute{o}^{xy}_{i+\frac{1}{2},j,k}\left(\acute{\mathrm{o}}_{j+\frac{1}{2}}-\acute{\mathrm{o}}_{j-\frac{1}{2}}\right)_{i+\frac{1}{2},k}+\\ \acute{o}^{xz}_{i+\frac{1}{2},j,k}\left(\acute{\mathrm{o}}_{k+\frac{1}{2}}-\acute{\mathrm{o}}_{k-\frac{1}{2}}\right)_{i+\frac{1}{2},j}\end{array}\right\}. \tag{18}$$

Therefore, the flux through any voxel face depends on the potential, ψ, at six EFVM grid points. Two of these potential variables are located at nodes, one being the node (*i, j, k*) itself, and the node of an adjacent voxel – node (*i+1, j, k*). The coefficient associated with the potential difference between these two nodes is the principal effective conductivity value, $\acute{o}^{xx}_{i+\frac{1}{2},j,k}$. It is now clear that the remaining four potential variables involved in calculation of flux are located at voxel edge midpoints – (*i+½, j±½, k*) and (*i+½, j, k±½*). These voxel edge variables are introduced into the system as additional nodes. In this work, these new edge nodes are referred to as *internodes*, which are

indicated by gray circles in all figures (see Figure 2-3). The coefficients associated with potential differences between these two pairs of internodes are the coupled effective conductivity values $\acute{o}^{xy}_{i+1/2,j,k}$ and $\acute{o}^{xz}_{i+1/2,j,k}$. As such, the four internode potentials involved in calculating flux through a voxel face, which are not part of the basic FVM, account for the conductive coupling between volume dimensions.

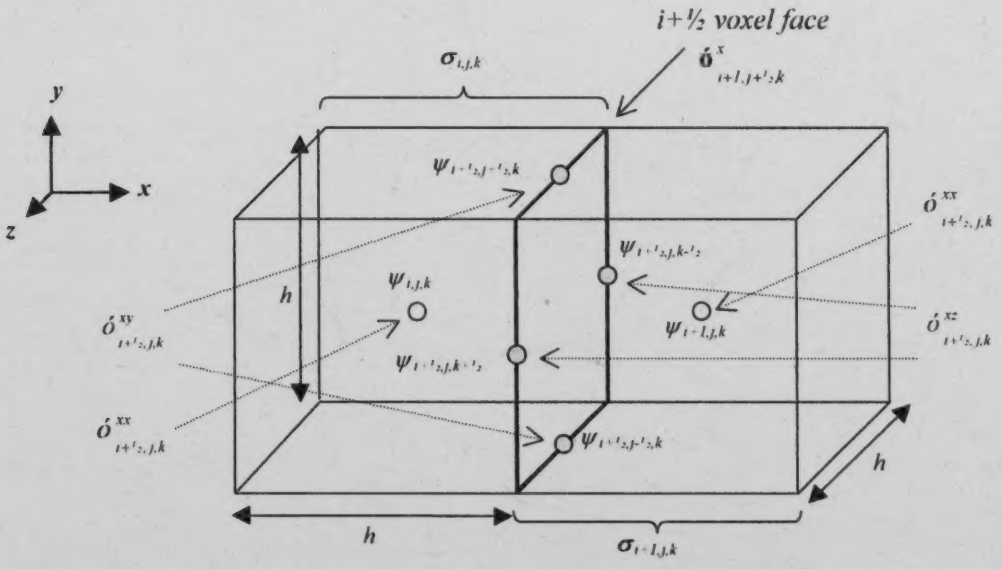

Figure 2-3: Two nodes (white circles) and four internodes (gray circles) involved in calculating the flux through voxel face ($i+½$, j, k) (18). The coefficients associated with the three pairs of potential variables, ψ, in (18) are elements of $\acute{\mathbf{o}}^{x}_{i+1/2,j,k}$, the effective conductivity vector of the voxel face. The coefficient of the potential difference between nodes is the principal effective conductivity value, $\acute{o}^{xx}_{i+1/2,j,k}$, whereas the coefficients of the potential differences between internodes are the coupled effective conductivity values, $\acute{o}^{xy}_{i+1/2,j,k}$ and $\acute{o}^{xz}_{i+1/2,j,k}$.

Equations similar to (18), for current flowing out through the other five faces of voxel (i, j, k), sum according to (17) to give the complete expression for total source current inside the cell,

$$
\begin{aligned}
&\acute{o}^{xx}_{i+\frac{1}{2},j,k}\left(\varnothing_i-\varnothing_{i+1}\right)_{j,k}+\acute{o}^{xy}_{i+\frac{1}{2},j,k}\left(\varnothing_{j-\frac{1}{2}}-\varnothing_{j+\frac{1}{2}}\right)_{i+\frac{1}{2},k}+\acute{o}^{xz}_{i+\frac{1}{2},j,k}\left(\varnothing_{k-\frac{1}{2}}-\varnothing_{k+\frac{1}{2}}\right)_{i+\frac{1}{2},j}+\\
&\acute{o}^{xx}_{i-\frac{1}{2},j,k}\left(\varnothing_i-\varnothing_{i-1}\right)_{j,k}+\acute{o}^{xy}_{i-\frac{1}{2},j,k}\left(\varnothing_{j+\frac{1}{2}}-\varnothing_{j-\frac{1}{2}}\right)_{i-\frac{1}{2},k}+\acute{o}^{xz}_{i-\frac{1}{2},j,k}\left(\varnothing_{k+\frac{1}{2}}-\varnothing_{k-\frac{1}{2}}\right)_{i-\frac{1}{2},j}+\\
&\acute{o}^{yy}_{i,j+\frac{1}{2},k}\left(\varnothing_j-\varnothing_{j+1}\right)_{i,k}+\acute{o}^{xy}_{i,j+\frac{1}{2},k}\left(\varnothing_{i-\frac{1}{2}}-\varnothing_{i+\frac{1}{2}}\right)_{j+\frac{1}{2},k}+\acute{o}^{yz}_{i,j+\frac{1}{2},k}\left(\varnothing_{k-\frac{1}{2}}-\varnothing_{k+\frac{1}{2}}\right)_{i,j+\frac{1}{2}}+\\
&\acute{o}^{yy}_{i,j-\frac{1}{2},k}\left(\varnothing_j-\varnothing_{j-1}\right)_{i,k}+\acute{o}^{xy}_{i,j-\frac{1}{2},k}\left(\varnothing_{i+\frac{1}{2}}-\varnothing_{i-\frac{1}{2}}\right)_{j-\frac{1}{2},k}+\acute{o}^{yz}_{i,j-\frac{1}{2},k}\left(\varnothing_{k+\frac{1}{2}}-\varnothing_{k-\frac{1}{2}}\right)_{i,j-\frac{1}{2}}+\\
&\acute{o}^{zz}_{i,j,k+\frac{1}{2}}\left(\varnothing_k-\varnothing_{k+1}\right)_{i,j}+\acute{o}^{xz}_{i,j,k+\frac{1}{2}}\left(\varnothing_{i-\frac{1}{2}}-\varnothing_{i+\frac{1}{2}}\right)_{j,k+\frac{1}{2}}+\acute{o}^{yz}_{i,j,k+\frac{1}{2}}\left(\varnothing_{j-\frac{1}{2}}-\varnothing_{j+\frac{1}{2}}\right)_{i,k+\frac{1}{2}}+\\
&\acute{o}^{zz}_{i,j,k-\frac{1}{2}}\left(\varnothing_k-\varnothing_{k-1}\right)_{i,j}+\acute{o}^{xz}_{i,j,k-\frac{1}{2}}\left(\varnothing_{i+\frac{1}{2}}-\varnothing_{i-\frac{1}{2}}\right)_{j,k-\frac{1}{2}}+\acute{o}^{yz}_{i,j,k-\frac{1}{2}}\left(\varnothing_{j+\frac{1}{2}}-\varnothing_{j-\frac{1}{2}}\right)_{i,k-\frac{1}{2}}=\frac{I_{i,j,k}}{h}.
\end{aligned}
\tag{19}
$$

This equation is a linear combination of potential differences between the central node (i, j, k) and six adjacent nodes ($i\pm1$, j, k), (i, $j\pm1$, k), (i, j, $k\pm1$), plus 12 potential differences between internode pairs on opposing voxel edges, ($i\pm½$, $j\pm½$, k), (i, $j\pm½$, $k\pm½$), ($i\pm½$, j, $k\pm½$). That is, the total source current inside a voxel of anisotropic conductivity depends on 19 potential variables in all – seven nodes and 12 internodes (see Figure 2-4). Due to the potential difference structure of (19), when the equation is rearranged as a linear combination of individual potential variables, its coefficients add up to zero. This is an important property of the EFVM coefficient matrix (see Appendix A).

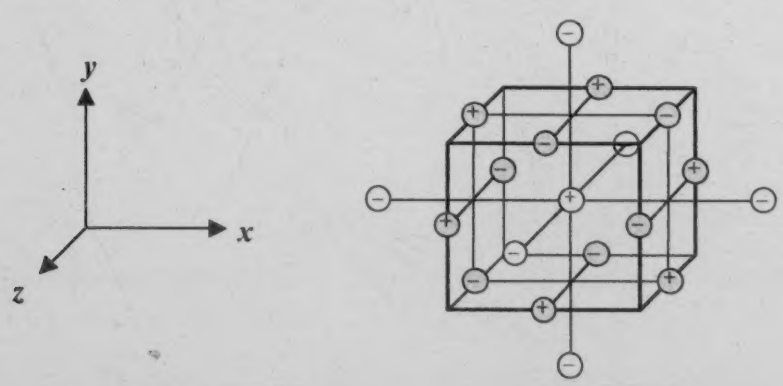

Figure 2-4: The locations of 19 discrete potentials involved in calculating the total source current inside a voxel (19) and the signs associated with the potential difference pairings (pairing lines on front and back faces are omitted for clarity). Seven are nodes at the voxel and its six neighbours. The other 12 are internodes located at the voxel edge midpoints.

Note that for a voxel conductivity tensor with null off-diagonal elements,

$$\mathbf{ó} = \begin{bmatrix} ó^{xx} & 0 & 0 \\ 0 & ó^{yy} & 0 \\ 0 & 0 & ó^{zz} \end{bmatrix}, \tag{20}$$

only the six left-most tensor values in (19) are nonzero, leaving precisely the orthotropic nodal equation of the FVM, as derived in [9],

$$\begin{aligned} & ó^{xx}_{i+\frac{1}{2},j,k}\left(ø_i - ø_{i+1}\right)_{j,k} + ó^{xx}_{i-\frac{1}{2},j,k}\left(ø_i - ø_{i-1}\right)_{j,k} + ó^{yy}_{i,j+\frac{1}{2},k}\left(ø_j - ø_{j+1}\right)_{i,k} + \\ & ó^{yy}_{i,j-\frac{1}{2},k}\left(ø_j - ø_{j-1}\right)_{i,k} + ó^{zz}_{i,j,k+\frac{1}{2}}\left(ø_k - ø_{k+1}\right)_{i,j} + ó^{zz}_{i,j,k-\frac{1}{2}}\left(ø_k - ø_{k-1}\right)_{i,j} = \frac{I_{i,j,k}}{h}. \end{aligned} \tag{21}$$

From (21) it is easy to see how the FVM, in its original form, accommodates orthotropic anisotropy by allowing each voxel to assume three distinct conductivity values in the x, y, and z directions. Voxel conductivity is isotropic when $\sigma_{xx} = \sigma_{yy} = \sigma_{zz}$. Either scenario results in nodal equations with exactly seven variables, and thus a linear system coefficient matrix with seven nonzero values (six off-diagonal elements) per row.

Returning to the EFVM, one might assume that a discrete internodal potential could be expressed as a weighted average of its four diagonally adjacent nodal potentials (see Figure 2-5). Then the EFVM equation for flux through a voxel face (18) could be modified to include ten *nodal* potential variables, avoiding the need for an internode framework. However, it is clear that (19), which relates adjacent nodal potentials in a generally anisotropic conductor model, is similarly applicable to internodes. Therefore, averaging potentials at neighbouring nodes in order to compute internode potentials is not an option. Rather, like nodal potentials, internodal potentials depend on a combination of potentials at surrounding nodes *and* internodes. It follows that additional linear equations

must be incorporated into the system to account for the potential at each internode. In order to apply (19) to internodes, we need to define *intervoxels,* which have the same dimensions as voxels and are centred on every internode.

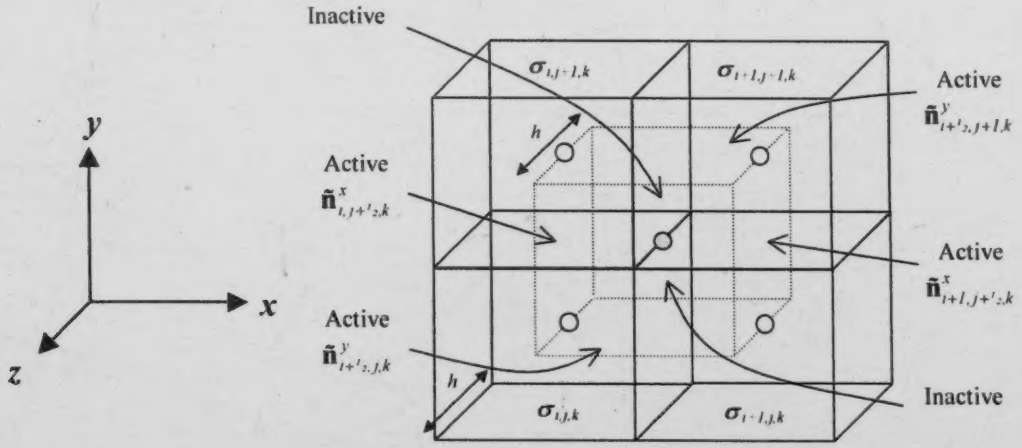

Figure 2-5: Four voxels (solid outlines) in the *x-y* plane and their shared intervoxel (dotted outline). The internode is involved in the equations that sum flux through each of the four shared voxel faces (in *x* or *y* directions), as well as the equations that sum flux through the active intervoxel faces. The effective conductivity vectors ($\tilde{\mathbf{n}}^{x}_{i+1,j+1/2,k}$, $\tilde{\mathbf{n}}^{x}_{i,j+1/2,k}$, $\tilde{\mathbf{n}}^{y}_{i+1/2,j+1,k}$, and $\tilde{\mathbf{n}}^{y}_{i+1/2,j,k}$) of the four active intervoxel faces are combinations of elements from the conductivity tensors, $\acute{o}$, of the two voxels that are straddled by each active intervoxel face. The two inactive intervoxel faces are shown here as the front and back intervoxel faces.

As mentioned, the use of internodes in the EFVM can account for conductive coupling between each pair of dimensions (*xy*, *yz*, and *xz* off-diagonal tensor values). It is consistent with this concept (and in agreement with (19), which includes potential variables at voxel edge midpoints) that every intervoxel is composed of a set of four quarter-voxels that combine in one of three planar orientations (*x-y*, *y-z*, or *x-z*). Note that the existence of a current source in the middle of a voxel does not contribute to the *net* flux in or out of any overlapping intervoxel, since nodes are located at intervoxel edges,

not within the boundary of the intervoxel volume (see Figure 2-5). This means that nodal current sources and sinks do not affect the linear equations used to describe total source current at internodes, and vice-versa.

Current flows through four of six intervoxel faces from within the quartet of voxels, with flux through each face passing on both sides of a tissue boundary. In other words, what we call the four a*ctive* intervoxel faces are centred on and orthogonal to each of the shared voxel faces inside the quartet. The other two intervoxel faces are said to be *inactive*. Each of these inactive faces is aligned with and centred on the junction of four outer voxel faces (see Figure 2-5).

Of course, current *does* flow through an inactive face, by virtue of the fact that we calculate flux through the four *voxel* faces on which the inactive intervoxel face is centred. However, flux through inactive faces is not included in the summation of intervoxel source current because, due to the configuration of eight partial voxels separating the two internodes on either side an inactive face, the conductivity between those two internodes is effectively zero. From another perspective, the conductive coupling between the two dimensions in a plane of voxels – which is accounted for by the intervoxel potentials inside that layer – is not directly related to current flow normal to that plane. Thus, the total source current inside an intervoxel depends on 17 potential variables in all – five nodes and 12 internodes.

To avoid confusion with voxel conductivity tensors, intervoxel conductivities are represented by the symbol ρ. Similar to the concept of effective conductivity of voxel faces, the flux through an active intervoxel face is characterized by an *intervoxel face effective conductivity vector*. This is some combination (to be defined later) of elements

in the conductivity tensors of the two voxels straddled by each active intervoxel face. Like the effective conductivity vector of a voxel face, the intervoxel face effective conductivity vector is comprised of a principal conductivity value and two coupled values.

The linear equations governing the flux through active intervoxel faces have the same form as those for voxel faces. For example, the expression for flux through face ($i+1$, $j+½$, k) in the x direction is just the same as (18) but with coefficients extracted from an intervoxel face effective conductivity vector $\tilde{\mathbf{n}}^{x}_{i+1,j+½,k}$, and all i and j indices shifted by $+½$,

$$\left(\tilde{\mathbf{n}}^{x}\nabla\phi\cdot\mathbf{S}^{x}\right)_{i+1,j+½,k} = h\left\{\begin{array}{l}\tilde{n}^{xx}_{i+1,j+½,k}\left(\phi_{i+1½}-\phi_{i+½}\right)_{j+½,k}+\\ \tilde{n}^{xy}_{i+1,j+½,k}\left(\phi_{j+1}-\phi_{j}\right)_{i+1,k}+\\ \tilde{n}^{xz}_{i+1,j+½,k}\left(\phi_{k+½}-\phi_{k-½}\right)_{i+1,j+½}\end{array}\right\}. \tag{22}$$

The flux through any active intervoxel face depends on the potential, ψ, at six EFVM grid points. These are the same six *relative* locations as in the case of flux through a *voxel* face. Two of these potential variables are located at nodes that are situated on two of the intervoxel face edges – ($i+1$, j, k) and ($i+1$, $j+1$, k) in the case of (22). The coefficient associated with the potential difference between these two nodes is the *in-plane* coupled effective conductivity value. In this case, the intervoxel exists in an x-y plane, so the coefficient for these nodal terms is denoted by $\tilde{n}^{xy}_{i+1,j+½,k}$.

The remaining four potential variables involved in calculation of flux through an intervoxel face are located at internodes. Two of these internodes belong to the intervoxels that share the face of interest, ($i+½$, $j+½$, k) and ($i+1½$, $j+½$, k) in (22). The

coefficient associated with the potential difference between this pair of internodes is the principal effective conductivity value, $\tilde{n}^{xx}_{i+1,j+1/2,k}$ in this case. The other pair of internode potential variables are located on two of the face edges, straddling the intervoxel plane – $(i+1,\ j+½,\ k±½)$ in the case of (22). The coefficient associated with the potential difference between these two internodes is the *out-of-plane* coupled effective conductivity value, here $\tilde{n}^{xz}_{i+1,j+1/2,k}$ (see Figure 2-6). The details of intfervoxel flux equations described above are similarly true for current flow in the y or z directions, and are applied to all intervoxels in the anisotropic head model. Of course, the intervoxel indices and directions associated with inter-dimensional coupling need to be adjusted according to the intervoxel location and planar orientation of its constituent voxel quartet.

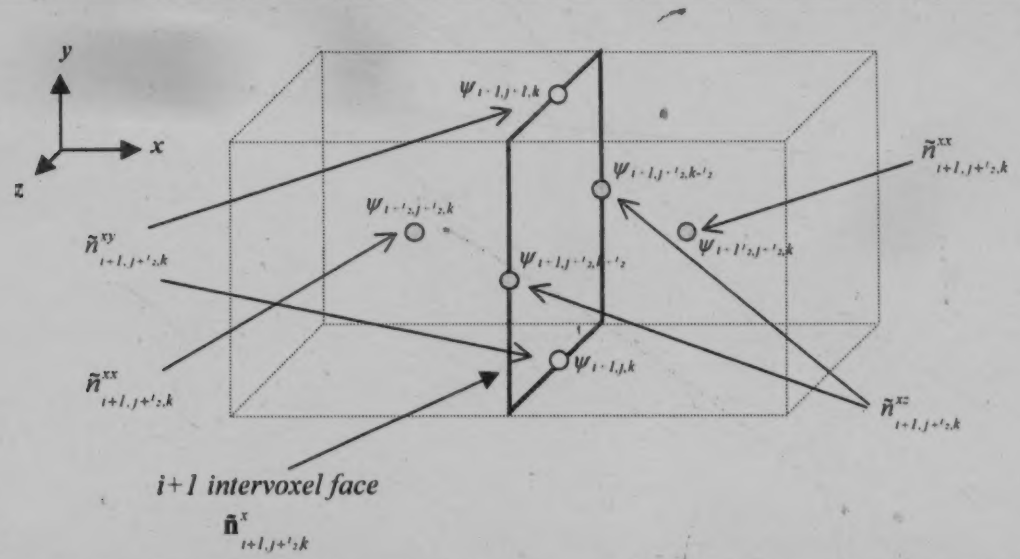

Figure 2-6: Two nodes and four internodes involved in calculating the flux out of an *x-y* intervoxel ($i+½$, $j+½$, k) through the active face ($i+1$, $j+½$, k) (22). The coefficients of the six potential variables, ψ, in (22) are elements of the effective conductivity vector $\tilde{\mathbf{n}}^{x}_{i+1,j+1/2,k}$. Potential difference between the two nodes is associated with the in-plane coupled effective conductivity value, $\tilde{n}^{xy}_{i+1,j+1/2,k}$. Potential difference between the pair of in-plane internodes is associated with the principal effective conductivity value, $\tilde{n}^{xx}_{i+1,j+1/2,k}$. Potential difference between the pair of out-of-plane internodes is associated with the out-of-plane coupled effective conductivity value, $\tilde{n}^{xz}_{i+1,j+1/2,k}$.

At this stage, it is necessary to define effective conductivity vectors, which constitute a combination of conductivity tensor values from both sides of a cell face. We follow the flux conservation method outlined in [4] and [9], but here the derivation is expanded to include generalized voxel anisotropy. There is an inherent difference between the definitions of effective conductivity for voxel and intervoxel faces. This is because each voxel is composed of a single conductivity tensor, whereas every intervoxel is, by definition, a combination of four voxels (see Figure 2-5).

We begin by examining the voxel face effective conductivity vector in an orthogonal coordinate system *u-v-w*, where basis vectors **u**, **v**, and **w** obey the relationship

$\mathbf{u} \times \mathbf{v} = \mathbf{w}$. This system is used to maintain generality in deriving the effective conductivity vectors of (inter)voxel faces that are normal to x, y, or z. Flux from voxel a into voxel b through face ab is described by an expression similar to (18),

$$\left(\acute{\mathbf{o}}^{uu}\nabla\phi \cdot \mathbf{S}^{u}\right)_{ab} = h\left\{\acute{o}^{uu}_{ab}\left(\phi_a - \phi_b\right) + \acute{o}^{uv}_{ab}\left(\phi_A - \phi_B\right) + \acute{o}^{uw}_{ab}\left(\phi_C - \phi_D\right)\right\}. \qquad (23)$$

Let us revisit the concept of a secondary cell, which is centred between adjacent voxels a and b. We apply (23) to calculate the flux in the u direction through the secondary cell in terms of the nodal potentials of the two primary cells (ψ_a and ψ_b) and the four internodal potentials (ψ_A, ψ_B, ψ_C, and ψ_D) around the edges of the shared face (see Figure 2-7). However, owing to the tissue discontinuity within the secondary cell, (23) cannot be applied directly. Thus, we define the current flow twice, based on the conductivity tensor of each half of the secondary cell, knowing that fluxes, J^+ and J^-, on either side of the tissue interface are exactly equal [9]. That is,

$$J^{+} = \left(\acute{\mathbf{o}}^{uu}\nabla\phi \cdot \mathbf{S}^{u}\right)_{a} = h\left\{2\acute{o}^{uu}_{a}\left(\phi_a - \phi^{*}\right) + \acute{o}^{uv}_{a}\left(\phi_A - \phi_B\right) + \acute{o}^{uw}_{a}\left(\phi_C - \phi_D\right)\right\}, \qquad (24)$$

and

$$J^{-} = \left(\acute{\mathbf{o}}^{uu}\nabla\phi \cdot \mathbf{S}^{u}\right)_{b} = h\left\{2\acute{o}^{uu}_{b}\left(\phi^{*} - \phi_b\right) + \acute{o}^{uv}_{b}\left(\phi_A - \phi_B\right) + \acute{o}^{uw}_{b}\left(\phi_C - \phi_D\right)\right\}, \qquad (25)$$

where ϕ^{*} is the intermediate potential at the boundary of the tissue interface. In (24) and (25), the principal conductivity values are multiplied by a factor of two to compensate for the half distances between nodes a and b. Equating the right hand sides of (24) and (25) gives

$$\phi^{*} = \frac{\acute{o}^{uu}_{a}\phi_a + \acute{o}^{uu}_{b}\phi_b + \tfrac{1}{2}\left(\acute{o}^{uv}_{a} - \acute{o}^{uv}_{b}\right)\left(\phi_A - \phi_B\right) + \tfrac{1}{2}\left(\acute{o}^{uw}_{a} - \acute{o}^{uw}_{b}\right)\left(\phi_C - \phi_D\right)}{\acute{o}^{uu}_{a} + \acute{o}^{uu}_{b}}. \qquad (26)$$

Then by substituting (26) into (24) or (25) we find that

$$J^{+} = J^{-} = \left(\acute{o}^{u}\nabla\phi \cdot \mathrm{S}^{u}\right)_{ab} = h\left\{\begin{array}{l} 2\dfrac{\acute{o}_a^{uu}\acute{o}_b^{uu}}{\acute{o}_a^{uu}+\acute{o}_b^{uu}}\left(\phi_a-\phi_b\right)+ \\ \dfrac{\acute{o}_a^{uv}\acute{o}_b^{uu}+\acute{o}_b^{uv}\acute{o}_a^{uu}}{\acute{o}_a^{uu}+\acute{o}_b^{uu}}\left(\phi_A-\phi_B\right)+ \\ \dfrac{\acute{o}_a^{uw}\acute{o}_b^{uu}+\acute{o}_b^{uw}\acute{o}_a^{uu}}{\acute{o}_a^{uu}+\acute{o}_b^{uu}}\left(\phi_C-\phi_D\right) \end{array}\right\}. \tag{27}$$

Comparing (27) to (23), it is clear that the principal value in the effective conductivity vector of voxel face *ab* is

$$\acute{o}_{ab}^{uu} = 2\frac{\acute{o}_a^{uu}\acute{o}_b^{uu}}{\acute{o}_a^{uu}+\acute{o}_b^{uu}}. \tag{28}$$

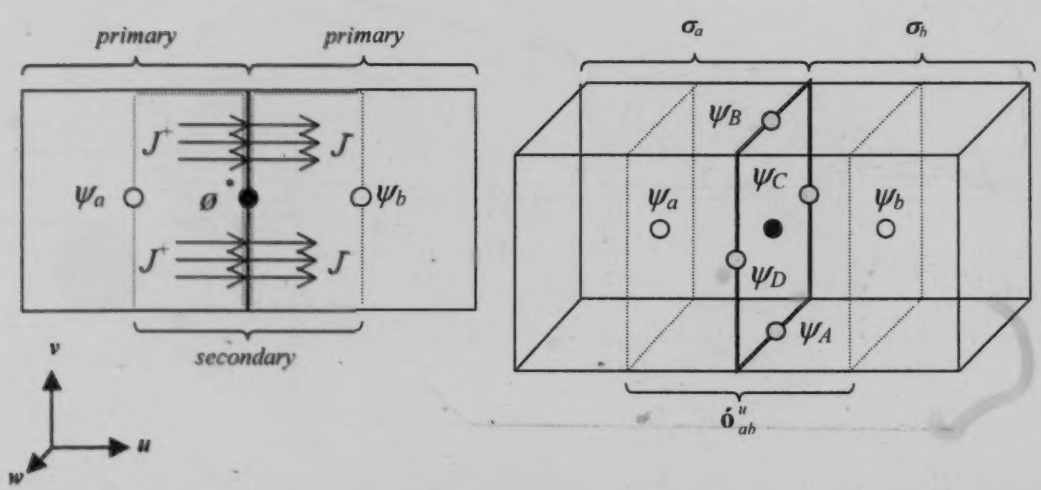

Figure 2-7: Current flow in the *u* direction through the shared face *ab* (bold outline) of two voxels *a* and *b*. (23) is applied to both halves of the secondary cell (dotted outlines) separately, accounting for the conductive discontinuity, σ_a meets σ_b. The black dot is an intermediate potential used to describe J^+ and J^- separately. Flux on either side of the face *ab* is exactly equal ($J^+ = J^-$). The effective conductivity vector of the voxel face, $\acute{o}_{ab}^{u}$, follows from this equality.

The principal element of any voxel face effective conductivity vector takes the general form of (28) where *a* and *b* are the indices of adjacent voxels and *u* is the direction in which they are aligned. This result is consistent with the effective

conductivity derived for the FVM in [4] and [9], which is just a series combination (reciprocal sum) of the principal conductivities of two half-voxels. Also, since conductivity is strictly a positive quantity, the diagonal values in any tensor are always positive, therefore, $\acute{o}_{ab}^{uu}$ is always positive.

Again, comparing (27) to (23), the *uv* coupled value in the effective conductivity vector of voxel face *ab* is

$$\acute{o}_{ab}^{uv} = \frac{\acute{o}_a^{uv}\acute{o}_b^{uu} + \acute{o}_b^{uv}\acute{o}_a^{uu}}{\acute{o}_a^{uu} + \acute{o}_b^{uu}}, \tag{29}$$

and the *uw* coupled value is

$$\acute{o}_{ab}^{uw} = \frac{\acute{o}_a^{uw}\acute{o}_b^{uu} + \acute{o}_b^{uw}\acute{o}_a^{uu}}{\acute{o}_a^{uu} + \acute{o}_b^{uu}}. \tag{30}$$

where *v* and *w* are the dimensions in which the two pairs of internode potential variables are offset from the face centre (see Figure 2-7). Note that in the case of orthotropic conductivities (diagonal tensors) at voxels *a* and *b*, both coupled values in the effective conductivity vector of their shared face vanish, as expected. Also, in the case that voxel *a* or *b* has an all zero conductivity tensor, the effective conductivity vector of the two is null, and no current will pass through their shared face. Thus, a layer of 'air' voxels surrounding the volume conductor model will guarantee satisfaction of the Neumann boundary condition (4).

Next, we examine the effective conductivity vector of active intervoxel faces by considering flux in the *v* direction from intervoxel *A* into intervoxel *B* through active face *AB*. Adapting (22) for this scenario gives,

$$\left(\tilde{\mathbf{n}}^v \nabla \phi \cdot \mathbf{S}^v\right)_{AB} = h\left\{\tilde{n}_{AB}^{vv}\left(\phi_A - \phi_B\right) + \tilde{n}_{AB}^{uv}\left(\phi_a - \phi_b\right) + \tilde{n}_{AB}^{vw}\left(\phi_C - \phi_D\right)\right\}. \tag{31}$$

The two upper and lower half-intervoxels on either side of face *AB* are actually composed of the left and right half-voxels *a* and *b* (see Figure 2-8). We apply (31) to calculate the flux through face *AB* in terms of one pair of nodal potentials (ψ_a and ψ_b) and two pairs of internodal potentials (ψ_A, ψ_B, ψ_C, and ψ_D). However, since there is a tissue discontinuity (σ_a meets σ_b) perpendicular to intervoxel face *AB*, (31) cannot be applied directly. Thus, we divide the face *AB* into two halves and calculate the flux twice, based on the conductivity tensors of the two voxels, *a* and *b*, which meet at the midline of the face *AB*. That is,

$$J^L = \left(\acute{\mathbf{o}}^v \nabla \acute{o} \cdot \mathbf{S}^v\right)_a = h\left\{\acute{o}_a^{vv}\left(\acute{o}_A - \acute{o}_B\right) + \acute{o}_a^{wv}\left(\acute{o}_a - \acute{o}^*\right) + \acute{o}_a^{wv}\left(\acute{o}_C - \acute{o}_D\right)\right\}, \tag{32}$$

and

$$J^R = \left(\acute{\mathbf{o}}^v \nabla \acute{o} \cdot \mathbf{S}^v\right)_b = h\left\{\acute{o}_b^{vv}\left(\acute{o}_A - \acute{o}_B\right) + \acute{o}_b^{wv}\left(\acute{o}^* - \acute{o}_b\right) + \acute{o}_b^{wv}\left(\acute{o}_C - \acute{o}_D\right)\right\}, \tag{33}$$

Fluxes J^L and J^R, on either side of the tissue discontinuity sum to equal the overall flux through face *AB*. In this case, addition of the two half fluxes accounts for the half distance between nodes *a* and *b*. That is,

$$J^L + J^R = \left(\tilde{\mathbf{n}}^v \nabla \acute{o} \cdot \mathbf{S}^v\right)_{AB} = h\begin{Bmatrix}\left(\acute{o}_a^{vv} + \acute{o}_b^{vv}\right)\left(\acute{o}_A - \acute{o}_B\right) + \\ \acute{o}_a^{wv}\acute{o}_a - \acute{o}_b^{wv}\acute{o}_b + \left(\acute{o}_b^{wv} - \acute{o}_a^{wv}\right)\acute{o}^* \\ \left(\acute{o}_a^{vw} + \acute{o}_b^{vw}\right)\left(\acute{o}_C - \acute{o}_D\right)\end{Bmatrix}. \tag{34}$$

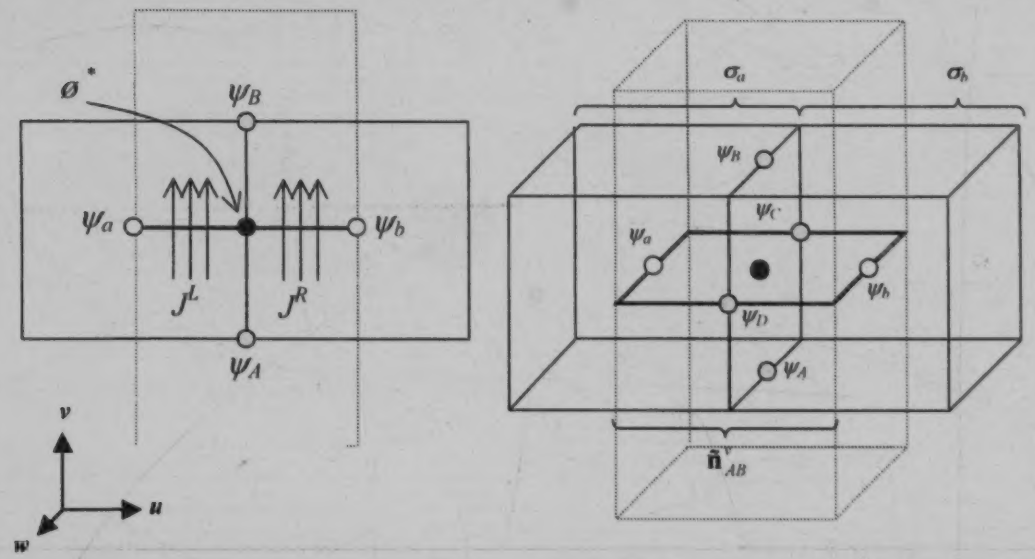

Figure 2-8: Current flow in the v direction through the shared active face AB (bold outline) of two intervoxels A and B (dotted outlines). (31) is applied to the left and right halves of face AB separately, accounting for the two voxel (solid outlines) conductivities, σ_a and σ_b. The black dot is an intermediate potential used to describe J^L and J^R separately. Flux into intervoxel B from the left and right halves of face AB sum to equal the total flux ($J = J^L + J^R$). The effective conductivity vector of the active intervoxel face, $\tilde{\mathbf{n}}^v_{AB}$, follows from this addition.

Previously we derived the equation describing ϕ^* (26), the intermediate discrete potential on voxel face ab. By substituting (26) into (34) we find that

$$\left(\tilde{\mathbf{n}}^v \nabla\phi \cdot \mathbf{S}^v\right)_{AB} = h\left\{\begin{array}{c} \left(\acute{o}_a^{vv} + \acute{o}_b^{vv} - \frac{\frac{1}{2}\left(\acute{o}_a^{uv} - \acute{o}_b^{uv}\right)^2}{\acute{o}_a^{uu} + \acute{o}_b^{uu}}\right)\left(\phi_A - \phi_B\right) + \\ \frac{\acute{o}_a^{uv}\acute{o}_b^{uu} + \acute{o}_b^{uv}\acute{o}_a^{uu}}{\acute{o}_a^{uu} + \acute{o}_b^{uu}}\left(\phi_a - \phi_b\right) + \\ \left(\acute{o}_a^{vw} + \acute{o}_b^{vw} - \frac{\frac{1}{2}\left(\acute{o}_a^{uv} - \acute{o}_b^{uv}\right)\left(\acute{o}_a^{uw} - \acute{o}_b^{uw}\right)}{\acute{o}_a^{uu} + \acute{o}_b^{uu}}\right)\left(\phi_C - \phi_D\right) \end{array}\right\}. \qquad (35)$$

Comparing (35) to (31), it is clear that the principal value in the effective conductivity vector of face AB is

$$\tilde{n}_{AB}^{vv} = \acute{o}_a^{vv} + \acute{o}_b^{vv} - \frac{\frac{1}{2}\left(\acute{o}_a^{uv} - \acute{o}_b^{uv}\right)^2}{\acute{o}_a^{uu} + \acute{o}_b^{uu}}, \tag{36}$$

The principal effective conductivity value of any active intervoxel face takes the general form of (36), where *A* and *B* are the indices of adjacent intervoxels, and *v* is the direction in which they are aligned. *a* and *b* are the indices of the voxels inside which the face *AB* exists, and *u* is the direction in which the voxels are aligned. That is, intervoxels *A* and *B* exist in a *u*-*v* plane (see Figure 2-8). Note that in the case of orthotropic conductivities at voxels *a* and *b*, the principal elements of the intervoxel face effective conductivity vector reduce to a parallel combination (arithmetic sum) of the conductivities of half-voxels *a* and *b*. Also, for realistic conductivity tensors, the diagonal (principal) values are generally 5 to 30 times larger than the off-diagonal (coupled) tensor values. Thus $\tilde{n}_{AB}^{vv}$ is always positive.

Again comparing (35) to (31), the *u*-*v* (in-plane) coupled value in the effective conductivity vector of face *AB* is

$$\tilde{n}_{AB}^{uv} = \frac{\acute{o}_a^{uv}\acute{o}_b^{uu} + \acute{o}_b^{uv}\acute{o}_a^{uu}}{\acute{o}_a^{uu} + \acute{o}_b^{uu}}. \tag{37}$$

Recall that this intervoxel face effective conductivity vector element is the coefficient associated with the potential difference between the pair of nodes involved in intervoxel flux equations such as (31) (see Figure 2-6). Note that (37) is identical to the equation for *coupled* values in the *voxel* effective conductivity vector face *ab*, $\acute{o}_{ab}^{uv}$ (29) and $\acute{o}_{ab}^{uv}$ (30).

Finally, comparing (35) to (31), the *v*-*w* (out-of-plane) coupled value in the effective conductivity vector of face *AB* is

$$\tilde{n}_{AB}^{vw} = \acute{o}_a^{vw} + \acute{o}_b^{vw} - \frac{½\left(\acute{o}_a^{uv} - \acute{o}_b^{uv}\right)\left(\acute{o}_a^{uw} - \acute{o}_b^{uw}\right)}{\acute{o}_a^{uu} + \acute{o}_b^{uu}}. \tag{38}$$

This intervoxel face effective conductivity vector element is the coefficient associated with the potential difference between the pair of internodes involved in intervoxel flux equations such as (31). These are the internodes that are located on the two outer edges of the intervoxel face of interest (see Figure 2-6). In the case of orthotropic conductivities at voxels *a* and *b*, the coupled (both in-plane and out-of-plane) values in the effective conductivity vector of the face *AB* (which exists inside *a* and *b*) vanish, as expected.

Recall that directions *u*-*v*-*w* are generalized representations of representations of Cartesian dimensions *x*-*y*-*z*, not necessarily respectively. As such, the general expressions derived for face effective conductivity values, (28) through (30) and (36) through (38), encompass the *x*-*y*-*z* conductive properties of all voxels and intervoxels in the *i*, *j*, *k* coordinate grid.

Returning to *x*-*y*-*z* dimensions, we are now prepared to draft the linear equation for total flux out of intervoxel ($i+½$, $j+½$, k). Usually, the total source current in every intervoxel is zero, since it is more intuitive and convenient to place current sources at nodes in the centres of voxels, rather than at internodes on voxel edges. The internode equation at ($i+½$, $j+½$, k) is similar to its nodal counterpart at (i, j, k), (19), except that the linear coefficients are intervoxel effective conductivity values (for only four faces), and all *i* and *j* indices are shifted by +½,

$$\begin{aligned}
&\tilde{n}^{xx}_{i+\frac{1}{2},j,k}\left(\varphi_{i+1\frac{1}{2}}-\varphi_{i+\frac{1}{2}}\right)_{j+\frac{1}{2},k}+\tilde{n}^{xy}_{i+1,j+\frac{1}{2},k}\left(\varphi_{j+1}-\varphi_{j}\right)_{i+1,k}+\tilde{n}^{xz}_{i+1,j+\frac{1}{2},k}\left(\varphi_{k+\frac{1}{2}}-\varphi_{k-\frac{1}{2}}\right)_{i+1,j+\frac{1}{2}}+\\
&\tilde{n}^{xx}_{i,j+\frac{1}{2},k}\left(\varphi_{i-\frac{1}{2}}-\varphi_{i+\frac{1}{2}}\right)_{j+\frac{1}{2},k}+\tilde{n}^{xy}_{i,j+\frac{1}{2},k}\left(\varphi_{j}-\varphi_{j+1}\right)_{i,k}+\tilde{n}^{xz}_{i,j+\frac{1}{2},k}\left(\varphi_{k-\frac{1}{2}}-\varphi_{k+\frac{1}{2}}\right)_{i,j+\frac{1}{2}}+\\
&\tilde{n}^{yy}_{i+\frac{1}{2},j+1,k}\left(\varphi_{j+1\frac{1}{2}}-\varphi_{j+\frac{1}{2}}\right)_{i+\frac{1}{2},k}+\tilde{n}^{xy}_{i+\frac{1}{2},j+1,k}\left(\varphi_{i+1}-\varphi_{i}\right)_{j+1,k}+\tilde{n}^{yz}_{i+\frac{1}{2},j1,k}\left(\varphi_{k+\frac{1}{2}}-\varphi_{k-\frac{1}{2}}\right)_{i+\frac{1}{2},j+1}+\\
&\tilde{n}^{yy}_{i+\frac{1}{2},j,k}\left(\varphi_{j-\frac{1}{2}}-\varphi_{j+\frac{1}{2}}\right)_{i+\frac{1}{2},k}+\tilde{n}^{xy}_{i+\frac{1}{2},j,k}\left(\varphi_{i}-\varphi_{i+1}\right)_{j,k}+\tilde{n}^{yz}_{i+\frac{1}{2},j,k}\left(\varphi_{k-\frac{1}{2}}-\varphi_{k+\frac{1}{2}}\right)_{i+\frac{1}{2},j}=0.
\end{aligned} \tag{39}$$

(19) and (39) are applied respectively to every node and internode in the EFVM head model to compile the full system of linear equations. The absolute indices of any grid point are appropriately shifted by some multiple of ±½ such that (i, j, k) or $(i+½, j+½, k)$ represent the centre of the voxel or intervoxel, respectively.

Now we should consider the effective conductivity vectors of voxel and intervoxel faces in a new light. That is, the interface of any two voxels in the EFVM is the location of three orthogonal cell faces. The cell face aligned with the tissue boundary is obviously a voxel face, whereas the two orthogonal cell faces belong to two different intervoxels (see Figure 2-9). All three faces derive their effective conductivity vectors from a combination of tensor values belonging to the two adjacent voxels. In this way, any pair of voxels combine to give an *effective conductivity tensor* which governs the flow of current through one voxel face and two intervoxel faces. For example, where voxel (i, j, k) meets voxel $(i+1, j, k)$ we have the effective conductivity tensor

$$\dot{\mathbf{o}}_{i+\frac{1}{2},j,k}=\begin{bmatrix}\dot{o}^{xx}_{i+\frac{1}{2},j,k} & \dot{o}^{xy}_{i+\frac{1}{2},j,k} & \dot{o}^{xz}_{i+\frac{1}{2},j,k}\\ \tilde{n}^{xy}_{i+\frac{1}{2},j,k} & \tilde{n}^{yy}_{i+\frac{1}{2},j,k} & \tilde{n}^{yz}_{i+\frac{1}{2},j,k}\\ \tilde{n}^{xz}_{i+\frac{1}{2},j,k} & \tilde{n}^{yz}_{i+\frac{1}{2},j,k} & \tilde{n}^{zz}_{i+\frac{1}{2},j,k}\end{bmatrix}=$$

$$\begin{bmatrix}\dfrac{\dot{o}^{xx}_{i,j,k}\dot{o}^{xx}_{i+1,j,k}}{\dot{o}^{xx}_{i,j,k}+\dot{o}^{xx}_{i+1,j,k}} & \dfrac{\dot{o}^{xy}_{i,j,k}\dot{o}^{xx}_{i+1,j,k}+\dot{o}^{xy}_{i+1,j,k}\dot{o}^{xx}_{i,j,k}}{\dot{o}^{xx}_{i,j,k}+\dot{o}^{xx}_{i+1,j,k}} & \dfrac{\dot{o}^{xz}_{i,j,k}\dot{o}^{xx}_{i+1,j,k}+\dot{o}^{xz}_{i+1,j,k}\dot{o}^{xx}_{i,j,k}}{\dot{o}^{xx}_{i,j,k}+\dot{o}^{xx}_{i+1,j,k}}\\ \dfrac{\dot{o}^{xy}_{i,j,k}\dot{o}^{xx}_{i+1,j,k}+\dot{o}^{xy}_{i+1,j,k}\dot{o}^{xx}_{i,j,k}}{\dot{o}^{xx}_{i,j,k}+\dot{o}^{xx}_{i+1,j,k}} & \dot{o}^{xy}_{i,j,k}+\dot{o}^{xy}_{i+1,j,k}-\dfrac{½\left(\dot{o}^{xy}_{i,j,k}-\dot{o}^{xy}_{i+1,j,k}\right)^2}{\dot{o}^{xx}_{i,j,k}+\dot{o}^{xx}_{i+1,j,k}} & \dot{o}^{yz}_{i,j,k}+\dot{o}^{yz}_{i+1,j,k}-\dfrac{½\left(\dot{o}^{xy}_{i,j,k}-\dot{o}^{xy}_{i+1,j,k}\right)\left(\dot{o}^{xz}_{i,j,k}-\dot{o}^{xz}_{i+1,j,k}\right)}{\dot{o}^{xx}_{i,j,k}+\dot{o}^{xx}_{i+1,j,k}}\\ \dfrac{\dot{o}^{xz}_{i,j,k}\dot{o}^{xx}_{i+1,j,k}+\dot{o}^{xz}_{i+1,j,k}\dot{o}^{xx}_{i,j,k}}{\dot{o}^{xx}_{i,j,k}+\dot{o}^{xx}_{i+1,j,k}} & \dot{o}^{xz}_{i,j,k}+\dot{o}^{xz}_{i+1,j,k}-\dfrac{½\left(\dot{o}^{xy}_{i,j,k}-\dot{o}^{xy}_{i+1,j,k}\right)\left(\dot{o}^{xz}_{i,j,k}-\dot{o}^{xz}_{i+1,j,k}\right)}{\dot{o}^{xx}_{i,j,k}+\dot{o}^{xx}_{i+1,j,k}} & \dot{o}^{zz}_{i,j,k}+\dot{o}^{zz}_{i+1,j,k}-\dfrac{½\left(\dot{o}^{xz}_{i,j,k}-\dot{o}^{xz}_{i+1,j,k}\right)^2}{\dot{o}^{xx}_{i,j,k}+\dot{o}^{xx}_{i+1,j,k}}\end{bmatrix} \tag{40}$$

Each row of the tensor corresponds to an effective conductivity vector of one of these faces. In this case, the voxel face vector is in the top row since the voxels are aligned in the x direction. Vectors for the two orthogonal intervoxel faces have similar constructions to each other, with the principal conductivity values on the tensor diagonal. Furthermore, the tensor is symmetric, and considering the expected properties of principal and coupled conductivity tensor elements, it can be shown to be positive definite.

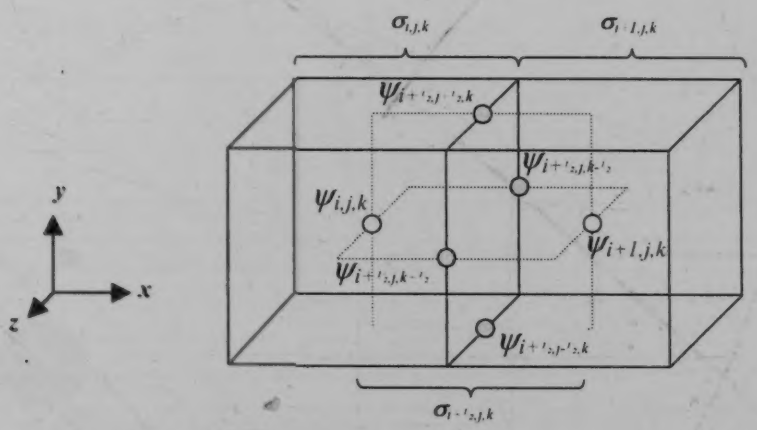

Figure 2-9: Three orthogonal cell faces – one voxel face (solid square), one *xy* intervoxel face (horizontal dotted square), and one xz intervoxel face (vertical dotted square) – through which flux is governed by the effective conductivity tensor $\sigma_{i+\frac{1}{2},j,k}$ (40).

The coefficient matrix associated with any system of linear equations is symmetric if and only if physical system is reciprocal [24]. Reciprocity, which is an inherent property of any linear volume conductor model, can be shown for the EFVM coefficient matrix by observing two characteristics of the effective conductivity values in (40). First, we note that by exchanging the conductivity tensors of two adjacent voxels ($\sigma_{i,j,k} \leftrightarrow \sigma_{i+1,j,k}$), the elements of their effective conductivity tensor $\sigma_{i+\frac{1}{2},j,k}$ are unchanged. Thus, conductive properties of any voxel or intervoxel face are equal as seen from either side, proving

symmetry amongst all the nodal equations, and independently, symmetry amongst all the internodal equations. The second characteristic that is required to prove symmetry in the EFVM system is reciprocity of nodal and internodal equations with respect to each other. This is demonstrated by the symmetry observed in the effective conductivity tensor (40). Namely, $\acute{o}^{xy}_{i+\frac{1}{2},j,k} = \tilde{n}^{xy}_{i+\frac{1}{2},j,k}$ and $\acute{o}^{xz}_{i+\frac{1}{2},j,k} = \tilde{n}^{xz}_{i+\frac{1}{2},j,k}$ for a pair of voxels aligned in the x direction. In words, within the linear equation describing flux through a voxel face (18), there is a coefficient associated with each of the two pairs of internode potential variables (Figure 2-3). These coefficients are identical to those belonging to the pair of nodal potential variables that show up in the two linear equations describing flux through the orthogonal intervoxel faces (Figure 2-6). Thus the EFVM linear system of equations is fully symmetric.

B. Volume Decomposition Algorithm

The EFVM system is represented in matrix form by the simple expression

$$\mathbf{A}_{N\times N} \cdot \mathbf{v}_{N\times 1} = \mathbf{b}_{N\times 1}, \tag{41}$$

where **A** is the matrix of coefficients of equations (19) and (39), **v** is the vector of discrete potentials, ψ, at every node and internode, **b** is the vector of total source current in each voxel or intervoxel, and N is the total number of (inter)nodes. **b** is zero at all positions corresponding to internodes, and has nonzero elements only at nodes where a current source and sink drives the forward solution. The highly vectorized volume decomposition algorithm used in this research to translate a discritized volume conductor into its EFVM system of equations is shown in Appendix B.

C. Reciprocity and the Lead Field Matrix

As shown at the end of Section II-A, the EFVM coefficient matrix is always symmetric, which not only makes it amenable to efficient solution techniques such as the Conjugate Gradient Method (to be discussed in Section II-D1), it also reflects the reciprocal nature of the linear conductor model. This means that placing a dipole source across any two nodes and measuring the potential difference across a second pair of nodes provides a result that is *exactly* equivalent to performing the experiment in reverse. The potential measured across the first pair of nodes, while forcing the source across the second pair, will be identical to the measurement obtained in the original scenario.

Reciprocity is an inherent property of any linear volume conductor model, and an important principle with respect to the inverse problem in EEG. This feature provides the opportunity to compile a complete lead field matrix (LFM: the input-output relationship between every possible current source and its resulting surface potentials) for a patient-specific conductor model by computing a forward solution once for each measurement lead [24]. To obtain the LFM *without* using reciprocity, the forward solution must be solved millions of times – once for each orientation of candidate current source inside the volume [6], [11], [13]. The LFM is a prerequisite for obtaining an inverse solution, and depends only on the head model and the electrode montage. Therefore, the forward data for a patient-specific head model can be used repeatedly to localize any number of source configurations from various EEG recording samples, by any discrete volume localization method. The bulk of the computational workload needs to be performed only once per patient [12], [25], [26].

For the purpose of compiling the LFM of a patient-specific EFVM head model, one forward solution is computed for each electrode pair by forcing a current source, I, at a single node that represents the active electrode and a current sink, $-I$, at the node that represents the reference electrode. The potential field for that lead is obtained by extracting the node components of the solution vector, $\mathbf{v}$, to give a solution subset $\mathbf{v}_{nodes}$. Taking the 3-D gradient of the potential at each voxel gives the electric field produced in the conductor by stimulation of the lead [13], also known as the lead sensitivity. A single direction of the gradient is calculated as the potential difference between two nodes on either side of the voxel of interest. Horizontal concatenation of the electric fields of all leads yields the complete LFM.

D. Solving the Forward Problem

1) The Conjugate Gradient Method: We rely on an iterative approach known as the Conjugate Gradient Method (CGM), used to solve the EFVM system of linear equations. $\mathbf{A}$ is sparse with generally 19 (nodal equations) or 17 (internodal equations) nonzero elements per row. Furthermore, the coefficient matrix is symmetric positive semidefinite. These matrix attributes are necessary for employment of the CGM. Since $\mathbf{A}$ is singular, the solution to which the CGM converges will not be unique. Indeed, it depends on the initial solution estimate provided to the solver program [27]. However, this lack of uniqueness (with respect to the *node* potentials) is easily rectified by subtracting a constant value from the entire solution vector such that the potential of the node deemed to be the reference becomes zero. For some other solution methods, positive definiteness of $\mathbf{A}$ may be required [22]. In this case, $\mathbf{A}$ can be deflated by removal of a combination of variables, yielding a symmetric positive definite coefficient matrix $\mathbf{A}_d$. Proof of

positive semidefiniteness of **A** and positive definiteness of $\mathbf{A}_d$ is given in Appendix A.

The CGM is an iterative technique designed to achieve the solution result using a number of steps that is no more than the dimension of the matrix itself. In practice though, the number of iterations may not need to be so large. Iterations need to be carried out only until the mean squared difference between **A** **v** and the input vector **b** is less than some tolerance value å. That is,

$$\|\mathbf{A}\cdot\mathbf{v}-\mathbf{b}\|_2 < \varepsilon. \tag{42}$$

Previous work with the FVM has shown that a tolerance value of $\varepsilon = 10^{-10}$ or less gives minimum error when comparing potentials on the surface of a discretized inhomogeneous sphere to those calculated by a gold standard analytical model [28]. Therefore we assume that this convergence criterion will provide a solution vector, **v**, of acceptable accuracy for the purposes of source localization by lead field analysis.

For a typical head model, the total number of (inter)nodes will be slightly more than 4 times the number of original voxels. (Exactly 4 times if the domain were infinite.) Admittedly, this imposes a significant cost increase in terms of data storage and computational load. However, decreasing the spatial resolution of the head model by a factor of $\sqrt[3]{4} \approx 1.6$ can reverse the four-fold growth in the number of variables. In fact, from a practical perspective, the maximum slice thickness of DTI is currently about 3 mm for most scanners. Constructing a patient-specific head model from a $(3\text{ mm})^3$ data set would yield a numerical model of no more than 200,000 voxels, which corresponds to an EFVM system of about 800,000 variables. A forward solution of this size does not present any significant challenge since we make use of the highly efficient polynomial preconditioned CGM [29]. A symmetric system of linear equations with around *four*

million variables can be solved in about two hours on an UltraSparc II 296 MHz processor with 1.2 GB RAM. Furthermore, it is reasonable to assume that as developing technology allows for higher MRI gradient field strengths, improving the spatial resolution of DTI, so will more powerful processors become increasingly accessible.

Incidentally, in two-dimensional space, by neglecting the z dimension, (18) reduces to a four-variable equation depending on two potentials at nodes (pixel centres) and two potentials at internodes (pixel corners). Therefore (19) and (39) reduce to nine variables each. In this case, there is only one type of internode accounting for xy inter-dimensional coupling, and the total number of (inter)nodes is just over twice the number of pixels in the head model slice. In this case, there are no inactive interpixel faces, since there is no third dimension to confuse the issue of conductive coupling. Validation experiments described in Section II-E2 were performed in two dimensions on an axial DTI slice.

2) Preconditioning: One of the major parameters that influences the effectiveness of the CGM is the ratio of the largest eigenvalue of **A** to the smallest one, often referred to as the *condition number* of **A**. The closer the condition number is to one the more quickly the iterative process converges. The process of improving the condition number of a matrix is known as *preconditioning*. Prior to or during solution, preconditioning operations can be performed on **A**. Many such methods are available, but two that applicable and suitable to improve the condition of the extraordinarily large system (41) are Jacobi preconditioning and polynomial preconditioning with Chebyshev polynomials. These methods are applied to all solutions of EFVM systems in this research and are described in detail in [29].

E. Verification Experiments

1) Comparison to Analytical Solution: Validity of the numerical model for electrostatic potential in an anisotropic medium developed in this work was verified by comparison to analytical solutions of Laplace's equation for homogenous and inhomogeneous conductors. Laplace's equation is just a special case of Poisson's equation (1) in the absence of any current source. For homogeneous anisotropic media whose conductivity tensor obeys the relation

$$\acute{o}^{xx} + \acute{o}^{yy} + \acute{o}^{zz} + 2\left(\acute{o}^{xy} + \acute{o}^{yz} + \acute{o}^{xz}\right) = 0, \tag{43}$$

the solution to Laplace's equation has the form

$$o = o_0 e^{x+y+z}. \tag{44}$$

This is also the form of solution for inhomogeneous anisotropic media whose conductivity tensors are given by

$$\acute{\mathbf{o}}_{inhomogeneous}(x,y,z) = \acute{\mathbf{o}}_{homogeneous}\, e^{x+y+z} = \begin{bmatrix} \acute{o}^{xx}e^{x+y+z} & \acute{o}^{xy}e^{x+y+z} & \acute{o}^{xz}e^{x+y+z} \\ \acute{o}^{xy}e^{x+y+z} & \acute{o}^{yy}e^{x+y+z} & \acute{o}^{yz}e^{x+y+z} \\ \acute{o}^{xz}e^{x+y+z} & \acute{o}^{yz}e^{x+y+z} & \acute{o}^{zz}e^{x+y+z} \end{bmatrix}, \tag{45}$$

with the elements of $\sigma_{homogeneous}$ governed by (43) [7].

An EFVM model with these specifications was generated in the form of a unit cube and forced potential boundary conditions were set according to (44). The Dirichlet boundary conditions on all outer faces of the cube were achieved by generating a vector of appropriate potentials at every outermost node and internode, with null potential elsewhere. Multiplying that vector by the EFVM system coefficient matrix, **A**, gives the volume current induced throughout the model by the desired boundary potentials. Subtraction of the resulting current vector from the actual (all zero) current source vector,

and removing the boundary equations from the system sets up a scenario where boundary potentials are fixed, but all inner potentials are determined by solution of the reduced system of equations.

This validation experiment was performed for several homogeneous and inhomogeneous unit cubes divided into various numbers of voxels. The conductivity values of (45) were designated as $\sigma_{xx} = 1$, $\sigma_{yy} = 1.5$, $\sigma_{zz} = 2$, $\sigma_{xy} = -0.25$, $\sigma_{yz} = -1.25$, and $\sigma_{xz} = -0.75$ in accordance with (43). Potential profiles calculated across the non-boundary nodes were compared to those generated according to the analytical formula (44). Comparisons are discussed in the Results section.

2) Realistic Model Comparison: To assess the importance, with respect to EEG source localization, of modeling anisotropic conductive properties of head tissue accurately, EFVM experiments were performed using DTI data acquired from the head of a human subject. Several comparisons were made between results obtained by the EFVM to those gathered by applying the isotropic FVM to the same head. One axial slice with $(1.72 \text{ mm})^2$ in-plane resolution (zero-fill interpolated to 0.86 mm) and 3 mm slice thickness was selected on which to perform these experiments in two dimensions.

Previously it was asserted that for any voxel of tissue, the conductivity tensor, $\boldsymbol{\sigma}$, can be approximated as being directly proportional to the diffusion tensor, $\mathbf{D}$ (9). For simplicity we assumed a scaling factor of 0.736 S s/mm^3. We adopted this value from [18], recognizing that the scaling of conductivities is actually unimportant to the purpose of this experiment, since for simulated cortical sources only the relative anisotropy and ratio of conductivities throughout the head volume are relevant. (Discussion of realistic scaling can be found in [16] and [18]). Thus, conductivity tensor values were scaled

directly from the DTI data with two noteworthy adjustments: 1) DTI provides a 3 by 3 tensor at every pixel in the selected axial slice. In order to build a 2-D model, the third dimension (z) of each tensor was discarded. 2) In the air region surrounding the head there were some nonzero diffusion tensor values due to noise. These were removed so that finite conductivities existed only at pixels corresponding to head tissue.

In addition to the anisotropic model, two isotropic models were constructed from the same data set. For one, the average of the 3-D tensor eigenvalues (trace divided by three) was taken as the conductivity of each pixel. We call this isotropic version the *trace* model. The second isotropic model was created by manually segmenting a T1-weighted image of the same axial slice according to tissue type and assigning a characteristic conductivity to each group (bone, CSF, gray matter, white matter, and other). Call this isotropic version the *segmented* model. In this case, tissue conductivities were estimated by averaging the "trace" values across all pixels of a given type. This method of assigning conductivities, as opposed to using values from literature, was used to provide a fair comparison between the three models.

For every pixel, the difference in tissue conductivity between the anisotropic and trace models was estimated by

$$\%Difference = \frac{\ddot{e}_{max} - trace(\dot{o})}{\ddot{e}_{max}} \times 100\%, \quad trace(\dot{o}) = \frac{\ddot{e}_1 + \ddot{e}_2 + \ddot{e}_3}{3}, \tag{46}$$

where λ_n are the 3-D tensor eigenvalues, and λ_{max} is the largest of these. The percent difference averaged over all tissue groups is given in TABLE 2-1, which also lists the characteristic conductivity assigned to each of the five tissue types in the segmented model. It should be noted that the manual process of tissue categorization, which is imprecise at best, imposes a heavy bias on these averaged conductivity values. However,

their accuracy relative to the conductivity distributions in the anisotropic and trace models is adequate for the purpose of this investigation.

TABLE 2-1

AVERAGE PERCENT CONDUCTIVITY DIFFERENCE IN THE ANISOTROPIC VERSUS THE TRACE MODEL AND THE CHARACTERISTIC CONDUCTIVITIES ASSIGNED TO TISSUE TYPES IN THE SEGMENTED MODEL

	Trace vs. Aniso.	Segmented
Tissue Type	Percent Difference	S/m
Bone	3.2%	0.018
CSF	11.2%	1.210
Gray Matter	10.3%	0.489
White Matter	31.3%	0.393
Scalp	24.1%	0.402

In three dimensions, the anisotropic diffusion in a voxel is often represented graphically by an ellipsoid, where the eccentricity of its shape is indicative of relative diffusivity in three principal (orthogonal) directions, that is, the relative magnitude of tensor eigenvalues [20]. Here, 2-D conductive anisotropy is shown by ellipses overlaid on each pixel of a T1-weighted MRI that shows the structural features of the axial plane selected for these modeling experiments (see Figure 2-10).

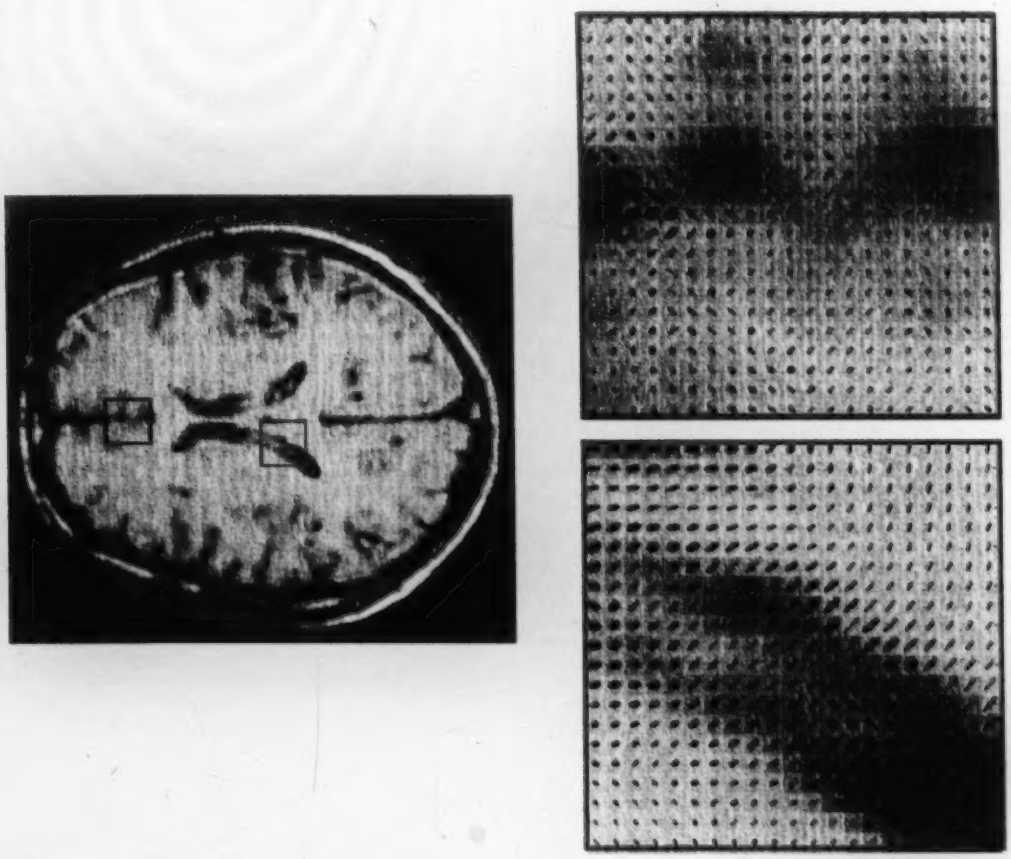

Figure 2-10: Conductive anisotropy shown by ellipses overlaid on each pixel of a T1-weighted MRI. Larger ellipse area indicates higher overall conductivity and ellipse elongation is indicative of anisotropy.

a) Lead Field Calculations: Using the decomposition algorithm shown in Appendix B, the time required to build the coefficient matrices (one for each model type) was about half a second for the FVM (33318 nodes) and on the order of thirty seconds for the EFVM (67050 total nodes) in MATLAB on a 1.4GHz PC with 128 MB RAM. LFMs were compiled for the three models by defining 7 electrode leads around the edge of the axial slice and computing of one forward solution per lead, with a source/sink magnitude of ±1 mA at the active and reference electrodes, respectively. Jacobi preconditioning was

implemented in MATLAB. The polynomial preconditioning coefficients that are read as inputs to the solver program [29] were also generated using MATLAB. The polynomial preconditioned CGM solver was programmed and compiled using C for increased computational and data input/output efficiency

b) Simulated EEG: 24 cortical current dipole sources were designated with various locations and orientations throughout the axial slice to represent possible epileptogenic foci. By the LFM compilation technique described in Section II-C, dipoles are implemented as a current source and sink at nodes straddling a central voxel, defined to be the source focus. In accordance with the reciprocity theorem, for a single dipole, the induced potentials across all leads were given by the LFM values corresponding to the x and y coordinates of the designated dipole location. Arbitrary dipole orientations were achieved by taking a linear combination of the x and y LFM components. A set of electrode potential vectors was produced for each of the three models. The 7 electrodes and 24 dipole locations are shown in Figure 2-11. The electrode montage was designed to provide denser spatial sampling near the front of the head in order to illustrate the effect of bioelectric conductor modeling errors with respect to proximity of field measurements.

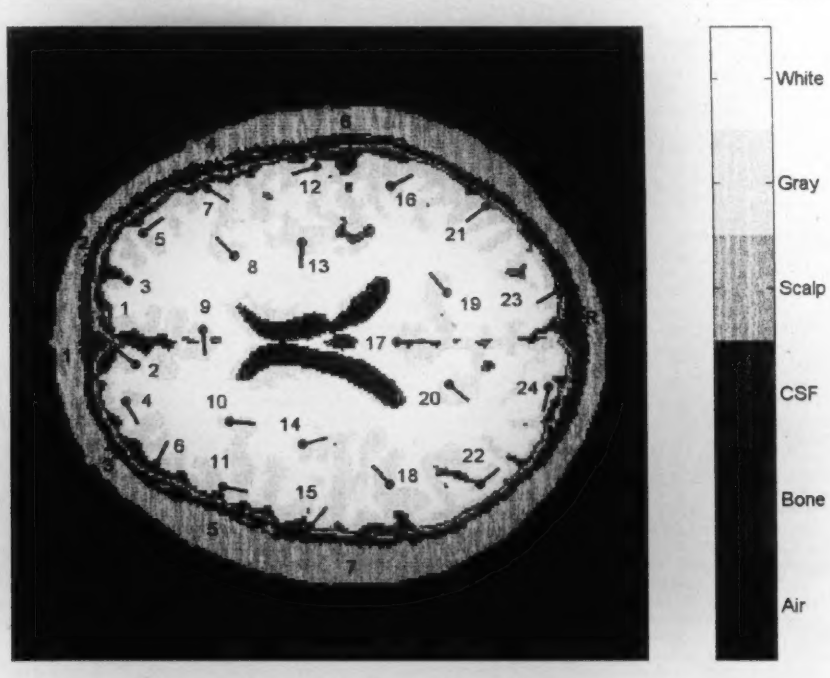

Figure 2-11: Seven electrode leads (R = reference electrode) and 24 cortical dipoles defined for lead field analysis and localization experiments, overlaid on the tissue-segmented axial slice. The markers on the brain are the designated dipoles, which extend across three pixels. Adjoining lines show the orientation (but not the extent) of each source.

c) Dipole Localization: A dipole localization experiment was performed to simulate the situation where EEG potentials could be recorded from a patient's scalp and used to localize sources within a realistic, but isotropic numerical head model. The potentials from the scalp of the anisotropic slice were applied as inputs to localize the 24 dipole sources within the trace and segmented isotropic head models using an exhaustive search least-squared dipole fitting technique. Localization errors were measured in terms of displacement, orientation, and magnitude.

III. Results

A. Forward Solution Details

Specifics of the forward solution method were investigated for the 2-D realistic models only. The numerical implementation of Laplace's equation used for anisotropic conductor model verification (see Section II-E1) has a simple solution that varies smoothly in space. Quick convergence of the CGM toward its final solution is not indicative of situation encountered when modeling a realistic head volume conductor of complex geometry and tissue distribution.

In any forward solution of the FVM or EFVM, a reference node can be defined by deflation of the coefficient matrix **A** before solution, or by subtraction after solution (see Section II-D1). Indeed, the subtraction method is much less computationally intensive and experiments with both techniques showed that a deflated system actually requires a few more iterations to converge on a solution than does the undeflated system. Therefore, matrix deflation is *not* recommended for iterative solution techniques such as the CGM, which can be used on positive semidefinite systems (see Appendix A).

The upper spectral bounds of the FVM and EFVM Jacobi preconditioned coefficient matrices were 2.0 and 3.19, respectively (estimated using MATLAB built-in function 'eigs'). It was determined empirically that the polynomial preconditioned CGM converges in the fewest number of iterations when the upper spectral bound input parameter is taken as that estimated value, and the lower spectral bound is set to about 0.01 for all models. Parameter values less than 0.01 (closer to the *real* lower bound of **A**) result in slower CGM convergence [29].

The degree of polynomial preconditioning that provided solution convergence in the least amount of time was found to be about 9 for the FVM and 10 for the EFVM (see Figure 2-12). The two realistic isotropic (FVM) models, which were equal in size, but different in arrangement, had the same optimal degree of polynomial preconditioning and the same solve time per iteration. However, the segmented model required more iterations to converge. It should be noted however, that the rate of convergence for a given system varies slightly depending on the specific source vector **b**, and results given in Figure 2-12 are averaged over the 7 lead forward solutions. Also, the degree parameter is not of crucial importance to the speed of convergence, as long as it is not too high or too low where convergence may not occur or be very slow. It is recommended, therefore, that for a particular size of (E)FVM coefficient matrix, the optimal degree of polynomial preconditioning be estimated empirically and then used consistently regardless of the source vector or conductivity details of the model.

Average best time for a forward solution of the trace model was 26 seconds (122 iterations), 28 seconds for the segmented model (131 iterations), and 2 minutes 36 seconds (188 iterations) for the anisotropic model on an UltraSparc II 296 MHz processor with 1.2 GB RAM.

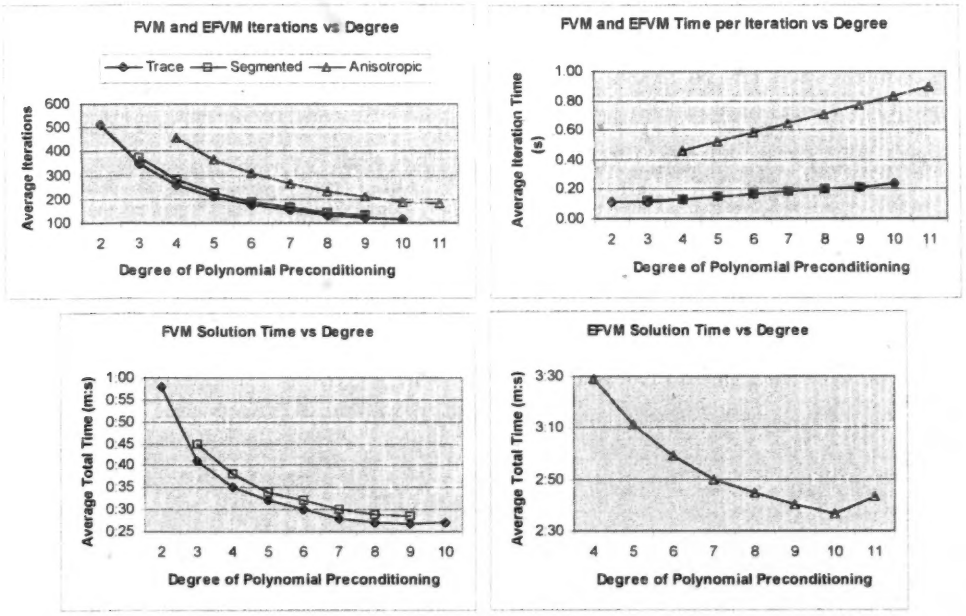

Figure 2-12: Polynomial preconditioned CGM convergence statistics for the anisotropic (EFVM), trace (FVM), and segmented (FVM) models. Ends of line graphs indicate no convergence at higher or lower degrees.

B. EFVM Verification Experiments

1) Comparison to Analytical Solution: Potential fields throughout an anisotropic unit cube calculated by the EFVM as compared to the known analytical solution of Laplace's equation are very accurate. In both the homogeneous and inhomogeneous cases, the numerical error computed at any single node is well under 0.2% for models of up to 41^3 voxels. Disagreement with the analytical solution tends to increase slightly with discretization level, but not to the extent that unacceptable errors would be expected in very large EFVM conductor models. Overall, errors are larger for the inhomogeneous anisotropic conductor. This effect is presumed to be due to effective conductivity tensor approximation at every voxel interface, which is not an issue for the homogeneous volume. L_2 norm and maximum percent error measures for all cases are displayed

graphically in Figure 2-13.

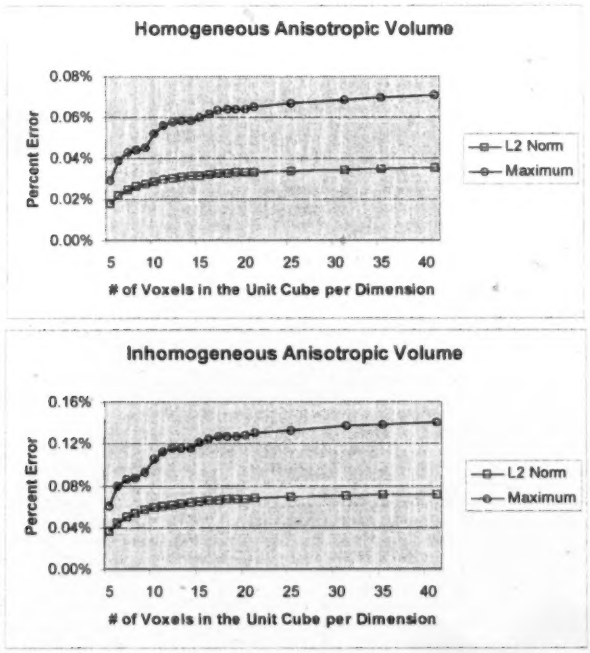

Figure 2-13: Error measures of non-boundary node potentials computed by the EFVM numerical model of Laplace's equation versus the known analytical solution inside a unit cube. Geometric mean vector distance and maximum single node percent errors are shown for various levels of discretization of homogeneous and inhomogeneous anisotropic volumes (total number of voxels in the unit cube = [voxels per dimension]^3).

2) Realistic Model Comparison

a) Lead Field Calculations: Isopotential contours of the potential field induced throughout the axial slice by stimulation of just one electrode pair (lead 3) and corresponding current paths are shown for each of the models in Figure 2-14. Note that the isopotential values indicated on each slice show a significantly different potential field distribution in each of the three models. Also, it is evident that tissue anisotropy (most notably in the white matter) causes curvature in the lines of current flow (A) which are not accounted for in the isotropic models (B and C).

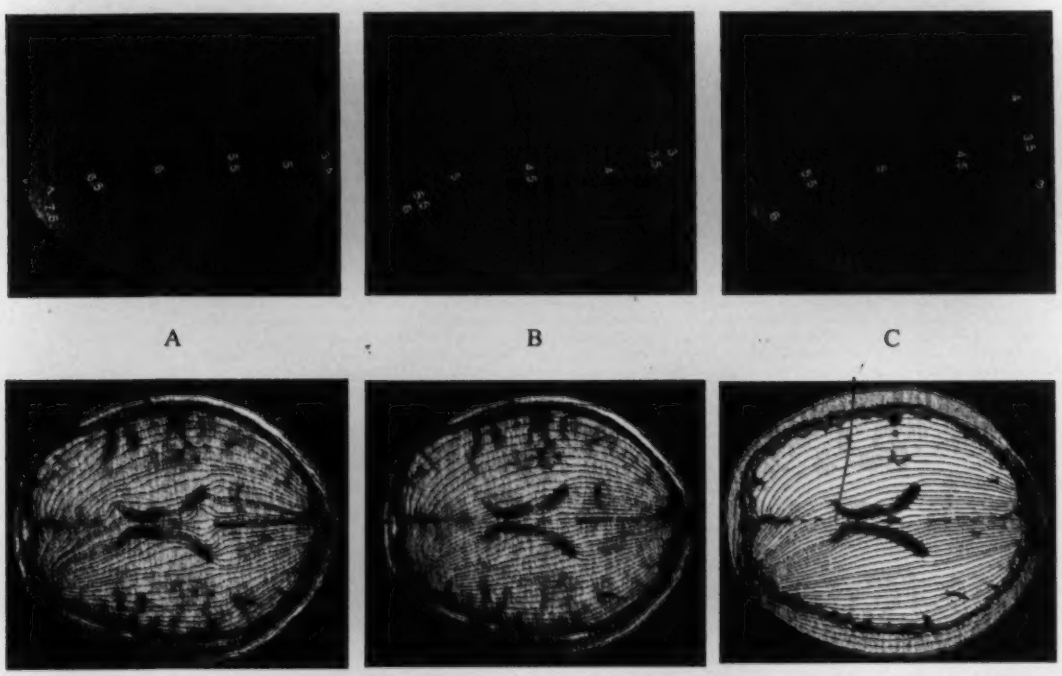

Figure 2-14: Isopotential contours in Volts (top row) and lines of current flow (bottom row) induced by stimulation of lead 3 for A) the anisotropic model, B) the trace model, and C) the segmented model. The three potential profiles have similar shapes (except in the case of the segmented model at the edges of the skull), but significantly different distributions with respect to magnitude. Lighter shading is indicative of higher potential. Differences between current paths in the three models are especially notable in regions of high anisotropy (white matter tracts surrounding the CSF).

b) Simulated EEG: The potentials induced at the electrodes of both isotropic models by each dipole source were calculated and compared to those extracted from the anisotropic head model. L_2 error norms of the isotropic model potential vectors are given in TABLE 2-2. For almost all dipoles, the electrode potentials induced in the segmented model differed more from the anisotropic model (with an average of 22.8%) than did electrode potentials computed using the trace model (average difference from anisotropic model was 10.3%). In both isotropic models, the most dramatic disagreements with the anisotropic model occurred for dipoles near the back of the head, which were not

spatially well sampled by the electrode configuration. Also, in the segmented model, large electrode potential discrepancies with respect to the anisotropic model were exhibited by superficial dipoles (near the skull) with radial orientation.

TABLE 2-2

ERROR NORMS OF ISOTROPIC ELECTRODE POTENTIAL VECTORS

	Trace vs. Anisotropic	Segmented vs. Anisotropic
Dipole	$\frac{\left\|\mathbf{v}_{el,\,Ani} - \mathbf{v}_{el,\,Tr}\right\|_2}{\left\|\mathbf{v}_{el,\,Ani}\right\|_2}$	$\frac{\left\|\mathbf{v}_{el,\,Ani} - \mathbf{v}_{el,\,Seg}\right\|_2}{\left\|\mathbf{v}_{el,\,Ani}\right\|_2}$
1	11.2%	17.3%
2	20.3%	26.1%
3	7.3%	16.6%
4	11.2%	27.1%
5	9.4%	11.3%
6	5.9%	56.7%
7	11.5%	35.1%
8	15.3%	11.5%
9	9.8%	15.8%
10	6.9%	19.2%
11	5.0%	13.6%
12	11.5%	15.1%
13	21.7%	26.2%
14	10.6%	14.4%
15	51.6%	59.9%
16	19.4%	20.4%
17	34.7%	36.8%
18	3.2%	27.7%
19	6.2%	11.2%
20	3.7%	5.2%
21	31.3%	98.9%
22	8.0%	7.9%
23	45.3%	45.4%
24	17.2%	49.4%
Average	10.3%	22.8%

c) Dipole Localization: The simulated electrode potentials generated by the anisotropic model were used to localize the 24 selected dipoles within the trace and segmented isotropic models. Localization errors measured in terms of displacement (mm), orientation (degrees), and magnitude (%) are listed in TABLE 2-3. Almost all dipoles were localized with less error in the trace model as compared to the segmented

model. Displacement error averaged across the 24 dipoles was 4.9 mm in the trace model and 7.7 mm in the segmented model. These results are shown graphically in Figure 2-15.

TABLE 2-3

DIPOLE LOCALIZATION ERRORS FOR SIMULATED SCALP POTENTIALS GENERATED BY ANISOTROPIC EFVM – LOCALIZED IN ISOTROPIC TRACE AND SEGMENTED MODELS

	Trace vs. Anisotropic			**Segmented vs. Anisotropic**		
Dipole	Disp. (mm)	Ori. (deg.)	Mag. (%)	Disp. (mm)	Ori. (deg.)	Mag. (%)
1	2.6	15.6	19.5	6.1	23.0	105.5
2	2.4	1.5	22.9	8.8	0.6	308.1
3	1.9	2.3	29.2	5.5	6.7	53.3
4	1.7	2.3	5.7	3.5	8.4	4.2
5	5.2	10.0	20.1	6.1	58.8	125.6
6	1.2	0.2	54.0	9.8	4.9	12.4
7	0.9	2.2	32.6	3.6	7.3	116.2
8	2.6	6.8	16.1	5.4	8.1	16.7
9	1.9	6.3	4.9	2.6	7.0	7.6
10	1.9	1.3	8.7	5.2	1.3	17.8
11	1.2	0.6	5.9	4.3	13.1	0.1
12	1.9	2.2	34.1	1.9	8.5	6.8
13	1.2	2.8	18.6	3.1	1.9	19.6
14	0.9	10.2	1.8	6.1	15.4	5.3
15	0.9	18.8	0.9	3.5	37.3	22.0
16	2.6	8.8	3.8	5.4	17.5	8.5
17	3.1	1.6	94.5	2.6	6.9	43.6
18	3.6	2.2	10.8	7.4	1.7	2.1
19	8.1	6.9	10.0	18.1	3.1	4.1
20	4.6	5.1	7.7	5.5	3.5	5.2
21	4.3	11.6	23.6	8.6	3.1	61.0
22	21.5	5.9	141.8	27.3	26.2	15.6
23	23.2	104.0	11.0	14.3	103.7	44.1
24	17.7	74.9	228.6	20.5	94.3	575.9
Average	4.9	12.7	33.6	7.7	19.3	65.9

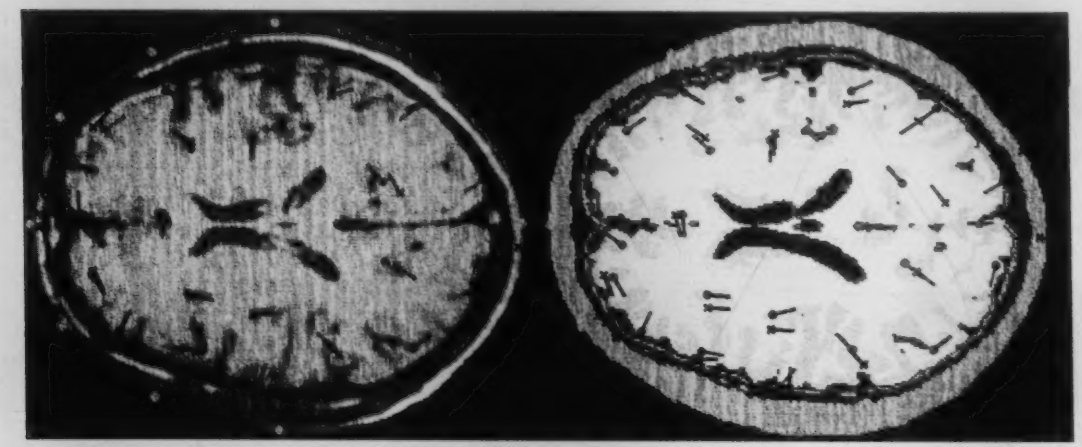

Figure 2-15: Dipole localization results from simulated electrode potentials generated by the anisotropic model used to localize 24 single dipole sources within the trace model (left) and segmented model (right). Actual dipoles marked with circles, estimated dipoles with crosses. Magnitude of localization errors is not shown.

In both isotropic models, as expected, dipole localization errors were significantly worse in regions of sparse spatial sampling by electrodes. Also, almost all dipoles were estimated to be more superficial than the actual source. In the trace model, quality of dipole localization was consistent for all dipole depths and orientations, and degraded only with distance from recording sites. In contrast, the segmented model generally gave better localization of deep radial, as compared to superficial radial, sources, which are farther removed from the dramatic conductive discontinuity of the skull. Deep and superficial tangential dipoles were localized equally well, except for in regions of sparse electrode sampling where localization was poor regardless of depth or orientation. It should be noted however, that even where several electrode lead fields overlap to give ample coverage, dipole estimation displacement errors were as high as 5.2 mm (dipole 5) in the trace model, and 9.8 mm (dipole 6) in the segmented model. This is an indication neglecting tissue anisotropy, and to a greater extent, the application of characteristic

conductivity values to segmented tissue regions may result in unreliable source localization.

Since the relationship between dipole parameters (location, orientation, and magnitude) and the electrode potentials induced by such a source is nonlinear, the error norms listed in TABLE 2-2 do not correlate well with dipole localization errors. Rather, localization accuracy is a function of the proximity between the true dipole source, and that hypothetical source which would best account for the potentials measured on the scalp. Nonetheless, a closer match between actual EEG measurements and electrode potentials computed by modeling a source near the true generator of recorded neural activity increases the chance that a small section of the brain will be correctly identified as the most likely focus. In such a case, the estimated source would be an adequate representation of reality for clinical purposes.

IV. Discussion

Results obtained through the two-dimensional EFVM experiments described above serve to illustrate the application of the EFVM to modeling anisotropic conductors, and provide insight about the expected problems with EEG source localization using unrealistically isotropic conductors. While the dipole localization errors shown here are not necessarily valid in a three-dimensional context, observable trends can be extended to provide a sense of what issues should be investigated in future 3-D modeling experiments. For example, we may speculate that the average dipole displacement error in a 3-D trace head model might be about 11 mm (or as much as 12 mm), and

approximately 20 mm (or as much as 31 mm) in a tissue-segmented isotropic head model.

Use of an isotropic conductor model for a system that is known to be anisotropic intuitively introduces error into a source localization procedure. Indeed we observed that the tensor trace model does not properly account for conduction effects in a realistically anisotropic head slice. This is consistent with results obtained by 3-D modeling of partially anisotropic volume conductors performed in [18] and [19]. However, segmentation of MRI by tissue type with uniform assignment of isotropic conductivity values to each tissue group, as is the usual method in EEG source localization, provides an even poorer conductor model for this purpose. Furthermore, unlike the segmented model described here, characteristic conductivities assigned to tissue-designated pixels are not usually obtained from patient-specific measurements, and as such are quite unreliable [18]. Thus, quantitative approximations of tissue conductivity should always be sought, whether or not the modeling procedure accounts for anisotropy.

DTI measures the net diffusion of water molecules through an imaging voxel over a short time frame. It should be understood that this macroscopic measurement of a microscopic process might yield misleading results. That is, there may be crossing fibres that can lead to apparently isotropic diffusion on a macroscopic level, giving a false impression of isotropic tissue. Therefore, in terms of accurately modeling anisotropic conductivity on a voxel scale, it is important to acquire the highest possible spatial resolution in all three dimensions (in-plane and slice thickness) so that DTI-based conductivity tensor estimations are of maximum benefit. Application of low resolution

or excessively noisy DTI data to the modeling of bioelectric conductors would likely reverse any accuracy gained from the inclusion of anisotropy in the head model.

V. Conclusions

By verification against a known analytical solution, we have confirmed that the EFVM conductor model gives a highly accurate representation of electrostatic conduction in an inhomogeneous anisotropic medium.

Utilization of DTI for quantifying patient-specific tissue conductivity tensors for use by the EFVM minimizes volume conductor modeling errors for EEG source localization. However, other unavoidable sources of error are always present. For example, EEG measurements themselves are always corrupted by noise, the digitization of electrode locations on the head model is subject to inaccuracy, and the unknown nature of cortical sources measured by EEG necessitates several modeling assumptions with respect to source configuration [24]. Further experimentation with 3-D anisotropic conductor models subject to non-ideal parameters (noise, unknown sources, etc.) would be useful to determine whether accurate modeling of conductor anisotropy is worthwhile in the context of realistic EEG source localization environment.

Although extension of the FVM to include generalized anisotropy increases the computational demand of the modeling procedure, it is still well within the capabilities of modern computer processors and can be performed in a reasonable amount of time for clinical application. With a pessimistic estimate of 2 hours per solution for a million voxel head model (four million variable EFVM solution), it would take about 4.5 days from the time of DTI acquisition to compile the LFM for a 50-lead EEG recording

montage, including all necessary pre- and post-processing. Usually, fewer electrodes are used and furthermore, given that every forward solution uses the same coefficient matrix, dedicated processors running in parallel could provide the entire LFM in little more than the time required for just one forward solution.

Whether working with an isotropic or anisotropic conductor model, it is advantageous to use DTI data to quantify patient-specific tissue conductivities throughout the head volume. This method is not only more accurate than previous modeling approaches, it also eliminates the need for tissue type segmentation of medical images – a nontrivial problem in itself [17].

References

[1] J. S. Ebersole, "Defining epileptogenic foci: past, present, and future," J. Clin. Neurophysiol., vol. 14, pp. 470-483, Nov. 1997.

[2] B. J. Roth, M. Balish, A. Gorbach, and S. Sato, "How well does a three-sphere model predict positions of dipoles in a realistically shaped head?", Electroencephalogr. Clin. Neurophysiol., vol. 87, pp. 175-184, Oct. 1993.

[3] B. N. Cuffin, D. L. Schomer, J. R. Ives, and H. Blume, "Experimental tests of EEG source localization accuracy in spherical head models," Clin. Neurophysiol., vol. 112, pp. 46-51, Jan. 2001.

[4] S. Abboud, Y. Eshel, S. Levy, and M. Rosenfeld, "Numerical calculation of the potential distribution due to dipole sources in a spherical model of the head, "Comput. Biomed. Res., vol. 27, pp. 441-455, Dec. 1994.

[5] L. Lemieux, A. McBride, and J. W. Hand, "Calculation of electrical potentials on the surface of a realistic head model by finite differences," Phys. Med. Biol., vol. 41, pp. 1079-1091, July 1996.

[6] P. Kauppinen, J. Hyttinen, P. Laarne, and J. Malmivuo, "A software implementation for detailed volume conductor modeling in electrophysiology using finite difference method," Comput. Methods Programs Biomed., vol. 58, pp. 191-203, Feb. 1999.

[7] H. I. Saleheen and K. T. Ng, "New finite difference formulations for general inhomogeneous anisotropic bioelectric problems," IEEE Trans. Biomed. Eng., vol. 44, pp. 800-809, Sept. 1997.

[8] P. Laarne, H. Eskola, J. Hyttinen, V. Suihko, and J. Malmivuo, "Validation of a detailed computer model for the electric fields in the brain," J. Med. Eng. Technol., vol. 19, pp. 84-87, Mar.-June 1995.

[9] M. Rosenfeld, R. Tanami, and S. Abboud, "Numerical solution of the potential due to sources in volume conductors with arbitrary geometry and conductivity," IEEE Trans. Biomed. Eng., vol. 43, pp. 679-689, July 1996.

[10] D. K. Cheng, *Field and Wave Electromagnetics*, 2nd ed. Reading, MA: Addison-Wesley, 1992.

[11] B. Vanrumste, G. Van Hoey, R. Van de Walle, M. R. D'Havé, I. A. Lemahieu, and P. A. Boon PA, "The Validation of the Finite Difference Method and Reciprocity for Solving the Inverse Problem in EEG Dipole Source Analysis," Brain Topogr., vol. 14, pp. 83-92, Winter 2001.

[12] H. Buchner, G. Knoll, M. Fuchs, A. Rienäcker, R. Beckmann, M. Wagner, J. Silny, and J. Pesch, "Inverse localization of electric dipole current sources in finite element models of the human head," Electroencephalogr. Clin. Neurophysiol., vol. 102, pp. 267-278, Apr. 1997.

[13] D. Weinstein, L. Zhukov, and C. Johnson, "Lead-field bases for electroencephalography source imaging," Ann. Biomed. Eng., vol. 28, pp.1059-1065, Sept. 2000.

[14] L. A. Geddes, L. E. Baker, "The specific resistance of biological material – a compendium of data for the biomedical engineer and physiologist," Med. Biol. Eng. Comput., vol. 5, pp. 271-293, May 1967.

[15] P. Laarne, P. Kauppinen, P. Hyttinen, J. Malmivuo, and H. Eskola, "Effects of tissue resistivities on electroencephalogram sensitivity distribution," Med. Biol. Eng. Comput., vol. 37, pp. 555-559, Sept. 1999.

[16] D. S. Tuch, V. J. Wedeen, A. M. Dale, J. S. George, and J. W. Belliveau, "Conductivity tensor mapping of the human brain using tensor MRI," Proc. Natl. Acad. Sci. U. S. A., vol. 98, pp. 11697-11701, Sept. 2001.

[17] M. Cercignani, M. Inglese, M. Siger-Zajdel, M. Filippi, "Segmenting brain white matter, gray matter and cerebro-spinal fluid using diffusion tensor-MRI derived indices," Magn. Reson. Imaging, vol. 19, pp. 1167-1172, Nov. 2001.

[18] J. Haueisen, D. S. Tuch, C. Ramon, P. H. Schimpf, V. J. Wedeen, J. S. George, and J. W. Belliveau, "The influence of brain tissue anisotropy on human EEG and MEG," Neuroimage vol. 15, pp. 159-166, Jan. 2002.

[19] G. Marin, C. Guerin, S. Baillet, L. Garnero, and G. Meunier, "Influence of skull anisotropy for the forward and inverse problem in EEG: simulation studies using FEM on realistic head models," Hum. Brain Mapp., vol. 6, pp. 250-269, 1998.

[20] C. Pierpaoli, P. Jezzard, P. J. Basser, A. Barnett, G. Di Chiro, "Diffusion tensor MR imaging of the human brain", Radiology, vol. 201, pp. 637-648, 1996.

[21] P. J. Basser, J. Mattiello, D. Le Bihan, "Estimation of the effective self-diffusion tensor from the NMR spin echo," J. Magn. Reson. B, vol. 103, pp. 247-254, 1994.

[22] K. A. Awada, D. R. Jackson, J. T. Williams, D. R. Wilton, S. B. Baumann, and A. C. Papanicolaou, "Computational aspects of finite element modeling in EEG source localization," IEEE Trans. Biomed. Eng., vol. 44, pp. 736-752, Aug. 1997.

[23] F. J. Asencor, M. Panizo, "Finite-Difference Operators in Anisotropic Inhomogeneous Dielectric: General Case," J. Comput. Phys., vol. 95, pp. 387-399, 1991.

[24] L. A. Neilson, Z. J. Koles, "The finite volume head model for EEG source localization," University of Alberta – Edmonton, 2002.

[25] C. M. Phillips, "Source estimation in EEG – combining anatomical and functional constraints," Sc.A.D thesis, Faculté des Sciences Appliquées, Université de Liège – Liège, 2001.

[26] P. Laarne, J. Hyttinen, S. Dodel, J. Malmivuo, and H. Eskola, "Accuracy of two dipolar inverse algorithms applying reciprocity for forward calculation," Comput. Biomed. Res., vol. 33, pp. 172-185, June 2000.

[27] Y. Saad, *Iterative Methods for Sparse Linear Systems*. Boston, MA: PWS-Kent., 1996.

[28] V. E. Agapov, "Numerical solution of the forward problem in electroencephalography," Ph.D. thesis, Department of Mathematical Sciences, University of Alberta – Edmonton, 2001.

[29] L. A. Neilson, Z. J. Koles, M. Kovalyov, "Accelerated forward solution of a high resolution volume conductor model by Chebyshev polynomial preconditioning," University of Alberta – Edmonton, 2003.

Appendix A: Positive Semidefiniteness of the EFVM Coefficient Matrix

The EFVM coefficient matrix **A** is positive semidefinite if for all nonzero vectors $\mathbf{v} \in \mathbf{R}$, $\mathbf{v}^T\mathbf{A}\mathbf{v} \geq 0$. The goal of the following text is to develop a concise expression for $\mathbf{v}^T\mathbf{A}\mathbf{v}$, which will show that **A** is indeed positive semidefinite, and how it can be deflated to yield a positive definite EFVM coefficient matrix. The linear equations that make up **A** can be divided into four categories: those that describe the total source current (**b** = **Av**) in voxels, and those that describe the total (usually zero) source current in the three types of intervoxels existing in *x*-*y*, *y*-*z*, and *x*-*z* planes. **A** is then expressed as

$$\mathbf{A} = \bigcup_{i=1}^{N_n} \mathbf{A}_{n_i} \cup \bigcup_{i=1}^{N_q} \mathbf{A}_{q_i} \cup \bigcup_{i=1}^{N_r} \mathbf{A}_{r_i} \cup \bigcup_{i=1}^{N_s} \mathbf{A}_{s_i}, \tag{A1}$$

where $\mathbf{A}_{n_i}$, $\mathbf{A}_{q_i}$, $\mathbf{A}_{r_i}$, and $\mathbf{A}_{s_i}$ are individual rows of A that correspond to voxel, *xy* intervoxel, *yz* intervoxel, and *xz* intervoxel equations, respectively. **A** is of dimension *N* by *N*, where $N = N_n + N_q + N_r + N_s$. Clearly, the vector **v** is composed of *N* potential variables, ψ, that are similarly indexed with subscripts *n*, *q*, *r*, and *s*, according to which type of node or internode potential they represent. It follows that

$$\mathbf{v}^T\mathbf{A}\mathbf{v} = \sum_{i=1}^{N_n} \psi_{n_i} \mathbf{A}_{n_i}\mathbf{v} + \sum_{i=1}^{N_q} \psi_{q_i} \mathbf{A}_{q_i}\mathbf{v} + \sum_{i=1}^{N_r} \psi_{r_i} \mathbf{A}_{r_i}\mathbf{v} + \sum_{i=1}^{N_s} \psi_{s_i} \mathbf{A}_{s_i}\mathbf{v}. \tag{A2}$$

Consider a single term in (A2), the total source current in the i^{th} voxel ($\mathbf{A}_{n_i}\mathbf{v} = \mathrm{b}_{n_i}$) multiplied by the potential of that node,

$$\phi_{n_i}\mathbf{A}_{n_i}\mathbf{v}=\phi_{n_i}\left\{\begin{array}{l}
\acute{o}^{xx}_{n_in_1}\left(\phi_{n_i}-\phi_{n_in_1}\right)+\acute{o}^{xy}_{n_in_1}\left(\phi_{n_iq_3}-\phi_{n_iq_1}\right)+\acute{o}^{xz}_{n_in_1}\left(\phi_{n_is_3}-\phi_{n_is_1}\right)+\\
\acute{o}^{xx}_{n_in_2}\left(\phi_{n_i}-\phi_{n_in_2}\right)+\acute{o}^{xy}_{n_in_2}\left(\phi_{n_iq_2}-\phi_{n_iq_4}\right)+\acute{o}^{xz}_{n_in_2}\left(\phi_{n_is_2}-\phi_{n_is_4}\right)+\\
\acute{o}^{yy}_{n_in_3}\left(\phi_{n_i}-\phi_{n_in_3}\right)+\acute{o}^{xy}_{n_in_3}\left(\phi_{n_iq_2}-\phi_{n_iq_1}\right)+\acute{o}^{yz}_{n_in_3}\left(\phi_{n_ir_3}-\phi_{n_ir_1}\right)+\\
\acute{o}^{yy}_{n_in_4}\left(\phi_{n_i}-\phi_{n_in_4}\right)+\acute{o}^{xy}_{n_in_4}\left(\phi_{n_iq_3}-\phi_{n_iq_4}\right)+\acute{o}^{yz}_{n_in_4}\left(\phi_{n_ir_2}-\phi_{n_ir_4}\right)+\\
\acute{o}^{zz}_{n_in_5}\left(\phi_{n_i}-\phi_{n_in_5}\right)+\acute{o}^{yz}_{n_in_5}\left(\phi_{n_ir_2}-\phi_{n_ir_1}\right)+\acute{o}^{xz}_{n_in_5}\left(\phi_{n_is_2}-\phi_{n_is_1}\right)+\\
\acute{o}^{zz}_{n_in_6}\left(\phi_{n_i}-\phi_{n_in_6}\right)+\acute{o}^{yz}_{n_in_6}\left(\phi_{n_ir_3}-\phi_{n_ir_4}\right)+\acute{o}^{xz}_{n_in_6}\left(\phi_{n_is_3}-\phi_{n_is_4}\right)
\end{array}\right\}. \quad \text{(A3)}$$

Effective conductivity values in (A3) have subscripts that indicate the 2 conductivity tensors involved. The first is n_i, the voxel of interest, and the second is n_f the adjacent voxel that shares face f with voxel n_i. Potential variables that have two subscripts are indexed relative to node n_i. For example, double subscript n_in_f refers to the node that is on the other side of face f from node n_i. n_iq_e refers to the e^{th} of 4 xy internodes surrounding voxel n_i, where nodes and internodes are numbered as shown in Figure 2-A1.

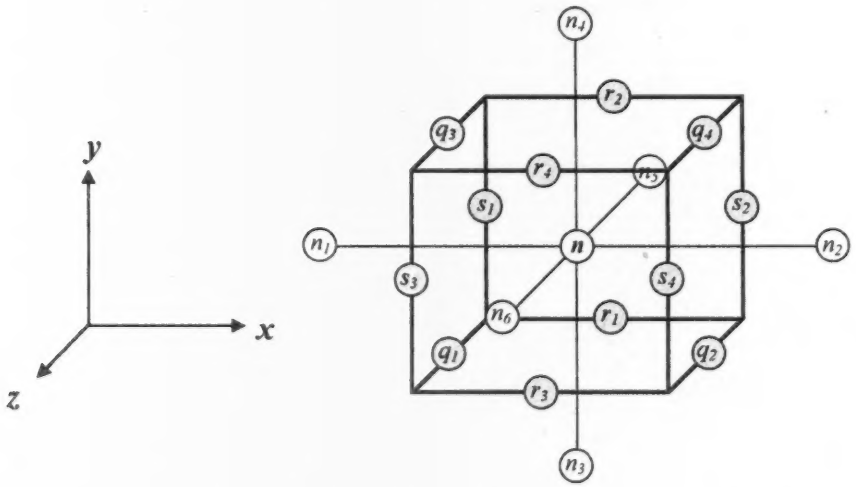

Figure 2-A1: System of potential variable relative indexing used for voxel equations such as (A3).

Equations similar to (A3) can be written for all of the other N_n-1 voxels in the model. These add up to form the first sum in (A2). In each of the single node expressions such

as (A3), for a principal conductivity term (left-most column) involving the indices n_i and n_f, $\phi_{n_i} \acute{o}^{pri}_{n_i n_f} \left(\phi_{n_i} - \phi_{n_i n_f} \right)$, there is an equation for an adjacent voxel that involves the term $\phi_{n_i n_f} \acute{o}^{pri}_{n_f n_i} \left(\phi_{n_i n_f} - \phi_{n_i} \right)$, where by the nature of effective conductivity values (see Section II-A), $\acute{o}^{pri}_{n_i n_f} = \acute{o}^{pri}_{n_f n_i}$. The sum of these reciprocal terms is $\acute{o}^{pri}_{n_i n_f} \left(\phi_{n_i} - \phi_{n_i n_f} \right)^2$. Likewise, for a coupled conductivity term in (A3) such as $\phi_{n_i} \acute{o}^{coup}_{n_i n_f} \left(\phi_{n_i q_a} - \phi_{n_i q_b} \right)$, there is an equation for an adjacent voxel that involves the term $\phi_{n_f} \acute{o}^{coup}_{n_f n_i} \left(\phi_{n_i q_b} - \phi_{n_i q_a} \right)$, where $\acute{o}^{coup}_{n_i n_f} = \acute{o}^{coup}_{n_f n_i}$. The sum of these two is $\acute{o}^{coup}_{n_i n_f} \left(\phi_{n_i} - \phi_{n_i n_f} \right) \left(\phi_{n_i q_a} - \phi_{n_i q_b} \right)$. Similar relationships exist for all variables in (A3). The first sum in (A2) is therefore conveniently written in terms of only the even-indexed voxel faces,

$$\sum_{i=1}^{N_n} \phi_{n_i} \mathbf{A}_{n_i} \mathbf{v} = \sum_{i=1}^{N_n} \left\{ \begin{array}{l} \acute{o}^{xx}_{n_i n_2} \left(\phi_{n_i} - \phi_{n_i n_2} \right)^2 + \acute{o}^{yy}_{n_i n_4} \left(\phi_{n_i} - \phi_{n_i n_4} \right)^2 + \acute{o}^{zz}_{n_i n_6} \left(\phi_{n_i} - \phi_{n_i n_6} \right)^2 + \\ \acute{o}^{xy}_{n_i n_2} \left(\phi_{n_i} - \phi_{n_i n_2} \right) \left(\phi_{n_i q_2} - \phi_{n_i q_4} \right) + \acute{o}^{xy}_{n_i n_4} \left(\phi_{n_i} - \phi_{n_i n_4} \right) \left(\phi_{n_i q_3} - \phi_{n_i q_4} \right) + \\ \acute{o}^{yz}_{n_i n_4} \left(\phi_{n_i} - \phi_{n_i n_4} \right) \left(\phi_{n_i r_2} - \phi_{n_i r_4} \right) + \acute{o}^{yz}_{n_i n_6} \left(\phi_{n_i} - \phi_{n_i n_6} \right) \left(\phi_{n_i r_3} - \phi_{n_i r_4} \right) + \\ \acute{o}^{xz}_{n_i n_2} \left(\phi_{n_i} - \phi_{n_i n_2} \right) \left(\phi_{n_i s_2} - \phi_{n_i s_4} \right) + \acute{o}^{xz}_{n_i n_6} \left(\phi_{n_i} - \phi_{n_i n_6} \right) \left(\phi_{n_i s_3} - \phi_{n_i s_4} \right) \end{array} \right\} . \quad \text{(A4)}$$

Next we examine an internode term in (A2), the total source current in the i^{th} xy intervoxel ($\mathbf{A}_{qi} \mathbf{v} = 0$) multiplied by the potential of that internode

$$\phi_{q_i} \mathbf{A}_{q_i} \mathbf{v} = \phi_{q_i} \left\{ \begin{array}{l} \tilde{n}^{xx}_{q_i q_1} \left(\phi_{q_i} - \phi_{q_i q_1} \right) + \tilde{n}^{xy}_{q_i q_1} \left(\phi_{q_i n_3} - \phi_{q_i n_1} \right) + \tilde{n}^{xz}_{q_i q_1} \left(\phi_{q_i r_3} - \phi_{q_i r_1} \right) + \\ \tilde{n}^{xx}_{q_i q_2} \left(\phi_{q_i} - \phi_{q_i q_2} \right) + \tilde{n}^{xy}_{q_i q_2} \left(\phi_{q_i n_2} - \phi_{q_i n_4} \right) + \tilde{n}^{xz}_{q_i q_2} \left(\phi_{q_i r_2} - \phi_{q_i r_4} \right) + \\ \tilde{n}^{yy}_{q_i q_3} \left(\phi_{q_i} - \phi_{q_i q_3} \right) + \tilde{n}^{xy}_{q_i q_3} \left(\phi_{q_i q_2} - \phi_{q_i q_1} \right) + \tilde{n}^{yz}_{q_i q_3} \left(\phi_{q_i s_3} - \phi_{q_i s_1} \right) + \\ \tilde{n}^{yy}_{q_i q_4} \left(\phi_{q_i} - \phi_{q_i q_4} \right) + \tilde{n}^{xy}_{q_i q_4} \left(\phi_{q_i n_3} - \phi_{q_i n_4} \right) + \tilde{n}^{yz}_{q_i q_4} \left(\phi_{q_i s_2} - \phi_{q_i s_4} \right) \end{array} \right\} . \quad \text{(A5)}$$

The subscripts used in (A5) are analogous to those in (A3) such that the intervoxel of interest is q_i and secondary indices are relative to it as illustrated in Figure 2-A2.

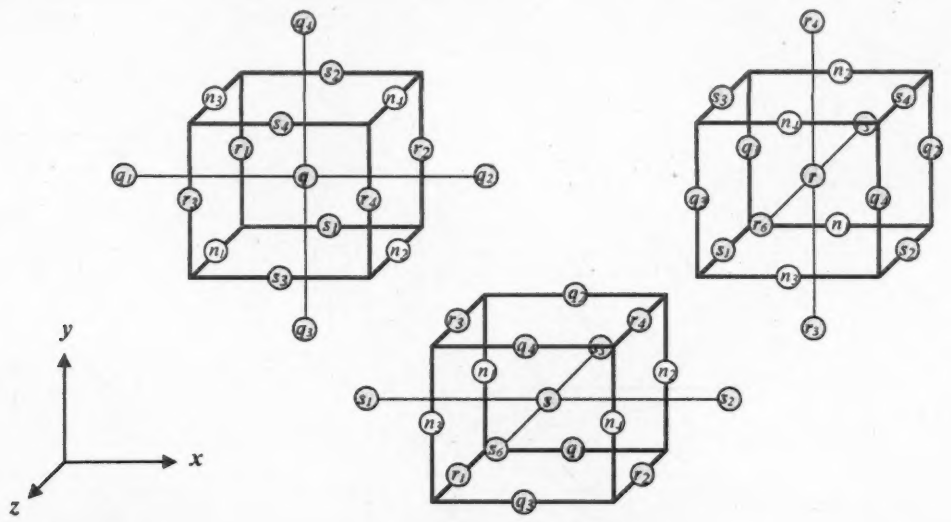

Figure 2-A2: System of potential variable relative indexing used for intervoxel equations such as (A5). The three cubes illustrate relative indexing in *xy* (central internode *q*), *yz* (central internode *r*), and *xz* (central internode *s*) intervoxels.

Equations similar to (A5) can be written for all of the other N_q-1 intervoxels in the model. These add up to form the second sum in (A2). In each of the single *xy* internode expressions such as (A5), for a principal conductivity term (left-most column) involving the indices q_i and q_f, $\varnothing_{q_i}\tilde{n}^{pri}_{q,q_f}\left(\varnothing_{q_i}-\varnothing_{q,q_f}\right)$, there is an equation for an adjacent *xy* intervoxel that involves the term $\varnothing_{q,q_f}\tilde{n}^{pri}_{q_f q_i}\left(\varnothing_{q,q_f}-\varnothing_{q_i}\right)$, where by the nature of effective conductivity values, $\tilde{n}^{pri}_{q,q_f}=\tilde{n}^{pri}_{q_f q_i}$. The sum of these reciprocal terms is $\tilde{n}^{pri}_{q,q_i^f}\left(\varnothing_{q_i}-\varnothing_{q,q_f}\right)^2$. Likewise, for a coupled conductivity term in (A5) such as $\varnothing_{q_i}\tilde{n}^{coup}_{q,q_f}\left(\varnothing_{q_i r_a}-\varnothing_{q_i r_b}\right)$, there is an equation for an adjacent voxel that involves the term $\varnothing_{q_f}\tilde{n}^{coup}_{q_f q_i}\left(\varnothing_{q_i r_b}-\varnothing_{q_i r_a}\right)$, where $\tilde{n}^{coup}_{q,q_f}=\tilde{n}^{coup}_{q_f q_i}$. The sum of these two is $\tilde{n}^{coup}_{q,q_f}\left(\varnothing_{a_i}-\varnothing_{a,a_f}\right)\left(\varnothing_{a_i r_a}-\varnothing_{a_i r_b}\right)$. Similar relationships exist for all variables in (A5). The

second sum in (A2) is therefore conveniently written in terms of only the even-indexed active *xy* intervoxel faces,

$$\sum_{i=1}^{N_q} \phi_{q_i} \mathbf{A}_{q_i} \mathbf{v} = \sum_{i=1}^{N_q} \left\{ \begin{array}{c} \tilde{n}^{xx}_{q_i q_2} \left(\phi_{q_i} - \phi_{q_i q_2} \right)^2 + \tilde{n}^{yy}_{q_i q_4} \left(\phi_{q_i} - \phi_{q_i q_4} \right)^2 + \\ \tilde{n}^{xy}_{q_i q_2} \left(\phi_{q_i} - \phi_{q_i q_2} \right)\left(\phi_{q_i n_2} - \phi_{q_i n_4} \right) + \tilde{n}^{xy}_{q_i q_4} \left(\phi_{q_i} - \phi_{q_i q_4} \right)\left(\phi_{q_i n_3} - \phi_{q_i n_4} \right) + \\ \tilde{n}^{yz}_{q_i q_4} \left(\phi_{q_i} - \phi_{q_i q_4} \right)\left(\phi_{q_i s_2} - \phi_{q_i s_4} \right) + \tilde{n}^{xz}_{q_i q_2} \left(\phi_{q_i} - \phi_{q_i q_2} \right)\left(\phi_{q_i r_2} - \phi_{q_i r_4} \right) \end{array} \right\}. \quad \text{(A6)}$$

Similarly for *yz* intervoxels, the third sum in (A2) is

$$\sum_{i=1}^{N_r} \phi_{r_i} \mathbf{A}_{r_i} \mathbf{v} = \sum_{i=1}^{N_r} \left\{ \begin{array}{c} \tilde{n}^{yy}_{r_i r_4} \left(\phi_{r_i} - \phi_{r_i r_4} \right)^2 + \tilde{n}^{zz}_{r_i r_6} \left(\phi_{r_i} - \phi_{r_i r_6} \right)^2 + \\ \tilde{n}^{xy}_{r_i r_4} \left(\phi_{r_i} - \phi_{r_i r_4} \right)\left(\phi_{r_i s_3} - \phi_{r_i s_4} \right) + \tilde{n}^{yz}_{r_i r_4} \left(\phi_{r_i} - \phi_{r_i r_4} \right)\left(\phi_{r_i n_2} - \phi_{r_i n_4} \right) + \\ \tilde{n}^{yz}_{r_i r_6} \left(\phi_{r_i} - \phi_{r_i r_6} \right)\left(\phi_{r_i n_3} - \phi_{r_i n_4} \right) + \tilde{n}^{xz}_{r_i r_6} \left(\phi_{r_i} - \phi_{r_i r_6} \right)\left(\phi_{r_i q_3} - \phi_{r_i q_4} \right) \end{array} \right\}, \quad \text{(A7)}$$

and for *xz* intervoxels, the fourth and final sum in (A2) is

$$\sum_{i=1}^{N_s} \phi_{s_i} \mathbf{A}_{s_i} \mathbf{v} = \sum_{i=1}^{N_s} \left\{ \begin{array}{c} \tilde{n}^{xx}_{s_i s_2} \left(\phi_{s_i} - \phi_{s_i s_2} \right)^2 + \tilde{n}^{zz}_{s_i s_6} \left(\phi_{s_i} - \phi_{s_i s_6} \right)^2 + \\ \tilde{n}^{xy}_{s_i s_2} \left(\phi_{s_i} - \phi_{s_i s_2} \right)\left(\phi_{s_i r_2} - \phi_{s_i r_4} \right) + \tilde{n}^{yz}_{s_i s_6} \left(\phi_{s_i} - \phi_{s_i s_6} \right)\left(\phi_{s_i q_3} - \phi_{s_i q_4} \right) + \\ \tilde{n}^{xz}_{s_i s_2} \left(\phi_{s_i} - \phi_{s_i s_2} \right)\left(\phi_{s_i n_2} - \phi_{s_i n_4} \right) + \tilde{n}^{xz}_{s_i s_6} \left(\phi_{s_i} - \phi_{s_i s_6} \right)\left(\phi_{s_i n_3} - \phi_{s_i n_4} \right) \end{array} \right\}, \quad \text{(A8)}$$

Now observe that all coupled conductivity terms in (A4) and (A6) through (A8) can be paired with an equivalent counterpart in one other of those equations to further reduce the complexity of the final expression for their sum, $\mathbf{v}^T\mathbf{A}\mathbf{v}$ (A2). For example, the first coupled conductivity term in (A4) for some voxel *i*, $\acute{o}^{xy}_{n_i n_2} \left(\phi_{n_i} - \phi_{n_i n_2} \right)\left(\phi_{n_i q_2} - \phi_{n_i q_4} \right)$, is equal to the second such term in (A6) for some *xy* intervoxel *j*, $\tilde{n}^{xy}_{q_j q_4} \left(\phi_{q_j} - \phi_{q_j q_4} \right)\left(\phi_{q_j n_3} - \phi_{q_j n_4} \right)$. This is true because face 2 of voxel *i* intersects orthogonally with some *xy* intervoxel face *j* (see Figure 2-A3). Hence $\acute{o}^{xy}_{n_i n_2} = \tilde{n}^{xy}_{q_j q_4}$ by the symmetry of effective conductivity tensors, as discussed in Section II-A.

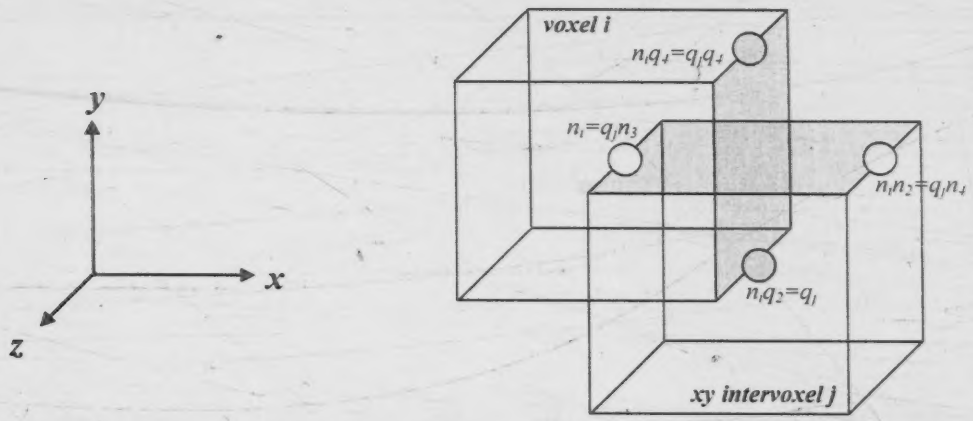

Figure 2-A3: Face 2 of voxel *i* (shaded vertical) intersects with face 4 of *xy* intervoxel *j*. Also, face 3 of voxel *i* intersects with face 1 of *xy* intervoxel *j*, but these odd numbered faces are accounted by reciprocity and do not appear in (A4) and (A6). Therefore, *i* and *j* have one term in common between (A4) and (A6).

Similar equalities can be stated for all 6 coupled conductivity terms in (A4) based on intersections of faces with all 3 types of intervoxels. These pairings account for the 2 in-plane coupled conductivity terms (those that involve nodes and internodes) in each of (A6) through (A8), leaving only the out-of-plane coupled conductivity terms (those that involve two pairs of internodes) unpaired as yet. There are 2 of these terms in each of (A6) through (A8), and each is equivalent to one term in one of the other two intervoxel types. For example, the first out-of-plane coupled conductivity term in (A6) for some *xy* intervoxel *i*, $\tilde{n}^{yz}_{q_iq_4}\left(\varnothing_{q_i}-\varnothing_{q_iq_4}\right)\left(\varnothing_{q_is_2}-\varnothing_{q_is_{2^*}}\right)$, is equal to the second such term in (A8) for some *xz* intervoxel *j*, $\tilde{n}^{yz}_{s_is_6}\left(\varnothing_{s_i}-\varnothing_{s_is_6}\right)\left(\varnothing_{s_iq_3}-\varnothing_{s_iq_4}\right)$, because face 4 of *xy* intervoxel *i* intersects orthogonally with some *xz* intervoxel face *j* (see Figure 2-A4).

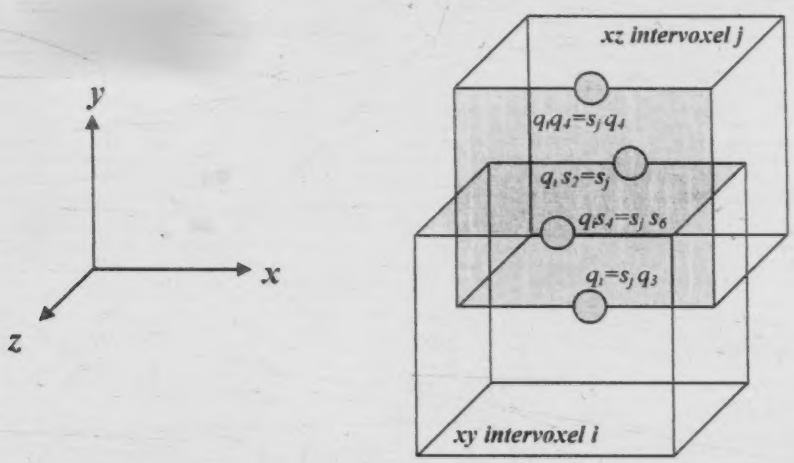

Figure 2-A4: Face 4 of *xy* intervoxel *i* (shaded vertical) intersects with face 6 of *xz* intervoxel *j*. Therefore, *i* and *j* have one term in common between (A6) and (A8).

A similar equality can be stated for the other out-of-plane coupled conductivity term in (A6) with one in (A7), based on the intersection of *xy* intervoxel face 2 with *yz* intervoxel face 6. The final pairing arises between terms in (A7) and (A8) due to the intersection of *yz* intervoxel face 4 with *xz* intervoxel face 2. Thus, all terms in (A4) and (A6) through (A8) are paired with an equivalent counterpart in one other of those equations giving a relatively expression for $\mathbf{v}^T\mathbf{A}\mathbf{v}$ as the term-paired version of the sum of (A4) and (A6) through (A8).

$$\mathbf{v}^{\mathrm{T}}\mathbf{A}\mathbf{v} = \sum_{i=1}^{N_n} \left\{ \begin{array}{l} \acute{o}^{xx}_{n_i n_2} \left(\phi_{n_i} - \phi_{n_i n_2}\right)^2 + \acute{o}^{yy}_{n_i n_4} \left(\phi_{n_i} - \phi_{n_i n_4}\right)^2 + \acute{o}^{zz}_{n_i n_6} \left(\phi_{n_i} - \phi_{n_i n_6}\right)^2 + \\ 2\left\{ \begin{array}{l} \acute{o}^{xy}_{n_i n_2} \left(\phi_{n_i} - \phi_{n_i n_2}\right)\left(\phi_{n_i q_2} - \phi_{n_i q_4}\right) + \acute{o}^{xy}_{n_i n_4} \left(\phi_{n_i} - \phi_{n_i n_4}\right)\left(\phi_{n_i q_3} - \phi_{n_i q_4}\right) + \\ \acute{o}^{yz}_{n_i n_4} \left(\phi_{n_i} - \phi_{n_i n_4}\right)\left(\phi_{n_i r_2} - \phi_{n_i r_4}\right) + \acute{o}^{yz}_{n_i n_6} \left(\phi_{n_i} - \phi_{n_i n_6}\right)\left(\phi_{n_i r_3} - \phi_{n_i r_4}\right) + \\ \acute{o}^{xz}_{n_i n_2} \left(\phi_{n_i} - \phi_{n_i n_2}\right)\left(\phi_{n_i s_2} - \phi_{n_i s_4}\right) + \acute{o}^{xz}_{n_i n_6} \left(\phi_{n_i} - \phi_{n_i n_6}\right)\left(\phi_{n_i s_3} - \phi_{n_i s_4}\right) \end{array} \right\} \end{array} \right\} + \quad \text{(A9)}$$

$$\sum_{i=1}^{N_q} \left\{ \tilde{n}^{xx}_{q_i q_2} \left(\phi_{q_i} - \phi_{q_i q_2}\right)^2 + \tilde{n}^{yy}_{q_i q_4} \left(\phi_{q_i} - \phi_{q_i q_4}\right)^2 + 2\tilde{n}^{yz}_{q_i q_4} \left(\phi_{q_i} - \phi_{q_i q_4}\right)\left(\phi_{q_i s_2} - \phi_{q_i s_4}\right) \right\} +$$

$$\sum_{i=1}^{N_r} \left\{ \tilde{n}^{yy}_{r_i r_4} \left(\phi_{r_i} - \phi_{r_i r_4}\right)^2 + \tilde{n}^{zz}_{r_i r_6} \left(\phi_{r_i} - \phi_{r_i r_6}\right)^2 + 2\tilde{n}^{xz}_{r_i r_6} \left(\phi_{r_i} - \phi_{r_i r_6}\right)\left(\phi_{r_i q_3} - \phi_{r_i q_4}\right) \right\} +$$

$$\sum_{i=1}^{N_s} \left\{ \tilde{n}^{xx}_{s_i s_2} \left(\phi_{s_i} - \phi_{s_i s_2}\right)^2 + \tilde{n}^{zz}_{s_i s_6} \left(\phi_{s_i} - \phi_{s_i s_6}\right)^2 + 2\tilde{n}^{xy}_{s_i s_2} \left(\phi_{s_i} - \phi_{s_i s_2}\right)\left(\phi_{s_i r_2} - \phi_{s_i r_4}\right) \right\}$$

The question of whether $\mathbf{v}^{\mathrm{T}}\mathbf{A}\mathbf{v} \geq 0$ has yet to be addressed. In order to do so, we need to examine the properties of the effective conductivity coefficients in (A9). They are expanded to give the complete expression for $\mathbf{v}^{\mathrm{T}}\mathbf{A}\mathbf{v}$ (A10). Note that in subsequent equations, conductivity symbols represent that of individual voxels, and not the effective conductivity of two voxels as before. For example, $\acute{o}^{xx}_{n_i n_2}$ refers to the principal conductivity value of the voxel that shares face 2 with voxel n_i, *no longer* the effective conductivity of voxel n_i and its neighbour on face 2.

$$
\begin{aligned}
\mathbf{v}^{\mathrm{T}}\mathbf{A}\mathbf{v} = \sum_{i=1}^{N} \Bigg\{ & \frac{2\acute{o}_{n}^{xx}\acute{o}_{nn_2}^{xx}}{\acute{o}_{n}^{xx}+\acute{o}_{nn_2}^{xx}}\left(\varnothing_{n}-\varnothing_{nn_2}\right)^{2} + \\
& \frac{2\acute{o}_{n}^{yy}\acute{o}_{nn_4}^{yy}}{\acute{o}_{n}^{yy}+\acute{o}_{nn_4}^{yy}}\left(\varnothing_{n}-\varnothing_{nn_4}\right)^{2} + \\
& \frac{2\acute{o}_{n}^{zz}\acute{o}_{nn_6}^{zz}}{\acute{o}_{n}^{zz}+\acute{o}_{nn_6}^{zz}}\left(\varnothing_{n}-\varnothing_{nn_6}\right)^{2} + \\
& 2\Bigg\{ \frac{\acute{o}_{n}^{yy}\acute{o}_{nn_2}^{xx}+\acute{o}_{nn_2}^{yy}\acute{o}_{n}^{xx}}{\acute{o}_{n}^{xx}+\acute{o}_{nn_2}^{xx}}\left(\varnothing_{n}-\varnothing_{nn_2}\right)\left(\varnothing_{nq_2}-\varnothing_{nq_4}\right) + \\
& \frac{\acute{o}_{n}^{yy}\acute{o}_{nn_4}^{yy}+\acute{o}_{nn_4}^{yy}\acute{o}_{n}^{yy}}{\acute{o}_{n}^{yy}+\acute{o}_{nn_4}^{yy}}\left(\varnothing_{n}-\varnothing_{nn_4}\right)\left(\varnothing_{nq_1}-\varnothing_{nq_3}\right) + \\
& \frac{\acute{o}_{n}^{yz}\acute{o}_{nn_6}^{yy}+\acute{o}_{nn_6}^{yz}\acute{o}_{n}^{yy}}{\acute{o}_{n}^{yy}+\acute{o}_{nn_6}^{yy}}\left(\varnothing_{n}-\varnothing_{nn_6}\right)\left(\varnothing_{nr_2}-\varnothing_{nr_4}\right) + \\
& \frac{\acute{o}_{n}^{xz}\acute{o}_{nn_6}^{zz}+\acute{o}_{nn_6}^{xz}\acute{o}_{n}^{zz}}{\acute{o}_{n}^{zz}+\acute{o}_{nn_6}^{zz}}\left(\varnothing_{n}-\varnothing_{nn_6}\right)\left(\varnothing_{nr_1}-\varnothing_{nr_3}\right) + \\
& \frac{\acute{o}_{n}^{xz}\acute{o}_{nn_2}^{xx}+\acute{o}_{nn_2}^{xz}\acute{o}_{n}^{xx}}{\acute{o}_{n}^{xx}+\acute{o}_{nn_2}^{xx}}\left(\varnothing_{n}-\varnothing_{nn_2}\right)\left(\varnothing_{ns_2}-\varnothing_{ns_4}\right) + \\
& \frac{\acute{o}_{n}^{xz}\acute{o}_{nn_6}^{zz}+\acute{o}_{nn_6}^{xz}\acute{o}_{n}^{zz}}{\acute{o}_{n}^{zz}+\acute{o}_{nn_6}^{zz}}\left(\varnothing_{n}-\varnothing_{nn_6}\right)\left(\varnothing_{ns_1}-\varnothing_{ns_3}\right) \Bigg\} \Bigg\} + \\
\sum_{i=1}^{N} \Bigg\{ & \Bigg\{ \acute{o}_{qn_2}^{xx}+\acute{o}_{qn_4}^{xx}-\frac{\tfrac{1}{2}\left(\acute{o}_{qn_2}^{xy}-\acute{o}_{qn_4}^{xy}\right)^{2}}{\acute{o}_{qn_2}^{yy}+\acute{o}_{qn_4}^{yy}} \Bigg\}\left(\varnothing_{q}-\varnothing_{qq_2}\right)^{2} + \\
& \Bigg\{ \acute{o}_{qn_1}^{yy}+\acute{o}_{qn_3}^{yy}-\frac{\tfrac{1}{2}\left(\acute{o}_{qn_1}^{xy}-\acute{o}_{qn_3}^{xy}\right)^{2}}{\acute{o}_{qn_1}^{xx}+\acute{o}_{qn_3}^{xx}} \Bigg\}\left(\varnothing_{q}-\varnothing_{qq_4}\right)^{2} + \\
& 2\Bigg\{ \acute{o}_{qn_5}^{xz}+\acute{o}_{qn_6}^{xz}-\frac{\tfrac{1}{2}\left(\acute{o}_{qn_5}^{xy}-\acute{o}_{qn_6}^{xy}\right)\left(\acute{o}_{qn_5}^{xz}-\acute{o}_{qn_6}^{xz}\right)}{\acute{o}_{qn_5}^{xx}+\acute{o}_{qn_6}^{xx}} \Bigg\}\left(\varnothing_{q}-\varnothing_{qq_1}\right)\left(\varnothing_{qs_2}-\varnothing_{qs_4}\right) \Bigg\} + \\
\sum_{i=1}^{N} \Bigg\{ & \Bigg\{ \acute{o}_{rn_2}^{yy}+\acute{o}_{rn_4}^{yy}-\frac{\tfrac{1}{2}\left(\acute{o}_{rn_2}^{yz}-\acute{o}_{rn_4}^{yz}\right)^{2}}{\acute{o}_{rn_2}^{zz}+\acute{o}_{rn_4}^{zz}} \Bigg\}\left(\varnothing_{r}-\varnothing_{rr_2}\right)^{2} + \\
& \Bigg\{ \acute{o}_{rn_1}^{zz}+\acute{o}_{rn_3}^{zz}-\frac{\tfrac{1}{2}\left(\acute{o}_{rn_1}^{yz}-\acute{o}_{rn_3}^{yz}\right)^{2}}{\acute{o}_{rn_1}^{yy}+\acute{o}_{rn_3}^{yy}} \Bigg\}\left(\varnothing_{r}-\varnothing_{rr_4}\right)^{2} + \\
& 2\Bigg\{ \acute{o}_{rn_5}^{yz}+\acute{o}_{rn_6}^{yz}-\frac{\tfrac{1}{2}\left(\acute{o}_{rn_5}^{yy}-\acute{o}_{rn_6}^{yy}\right)\left(\acute{o}_{rn_5}^{yz}-\acute{o}_{rn_6}^{yz}\right)}{\acute{o}_{rn_5}^{yy}+\acute{o}_{rn_6}^{yy}} \Bigg\}\left(\varnothing_{r}-\varnothing_{rr_1}\right)\left(\varnothing_{rq_2}-\varnothing_{rq_4}\right) \Bigg\} + \\
\sum_{i=1}^{N} \Bigg\{ & \Bigg\{ \acute{o}_{sn_2}^{xx}+\acute{o}_{sn_4}^{xx}-\frac{\tfrac{1}{2}\left(\acute{o}_{sn_2}^{xz}-\acute{o}_{sn_4}^{xz}\right)^{2}}{\acute{o}_{sn_2}^{zz}+\acute{o}_{sn_4}^{zz}} \Bigg\}\left(\varnothing_{s}-\varnothing_{ss_2}\right)^{2} + \\
& \Bigg\{ \acute{o}_{sn_1}^{zz}+\acute{o}_{sn_3}^{zz}-\frac{\tfrac{1}{2}\left(\acute{o}_{sn_1}^{xz}-\acute{o}_{sn_3}^{xz}\right)^{2}}{\acute{o}_{sn_1}^{xx}+\acute{o}_{sn_3}^{xx}} \Bigg\}\left(\varnothing_{s}-\varnothing_{ss_4}\right)^{2} + \\
& 2\Bigg\{ \acute{o}_{sn_5}^{xz}+\acute{o}_{sn_6}^{xz}-\frac{\tfrac{1}{2}\left(\acute{o}_{sn_5}^{xz}-\acute{o}_{sn_6}^{xz}\right)\left(\acute{o}_{sn_5}^{xz}-\acute{o}_{sn_6}^{xz}\right)}{\acute{o}_{sn_5}^{zz}+\acute{o}_{sn_6}^{zz}} \Bigg\}\left(\varnothing_{s}-\varnothing_{ss_1}\right)\left(\varnothing_{sr_2}-\varnothing_{sr_4}\right) \Bigg\}
\end{aligned}
\tag{A10}
$$

Considering the expected properties of conductivity tensors in the EFVM model, a reduced approximation of (A10) can be drafted to clarify the nature of $\mathbf{v}^T\mathbf{A}\mathbf{v}$. In particular, since principal (tensor diagonal) conductivity values are positive and about 5-30 times larger than coupled (off-diagonal) conductivity values, we generalize approximate magnitudes $ó^{pri} \approx ó_{exp} > 0$ and $ó^{coup} \approx \pm ⅕ ó_{exp}$. Then we can state that voxel principal effective conductivity values $\frac{2ó_a^{pri} ó_b^{pri}}{ó_a^{pri} + ó_b^{pri}} \approx ó_{exp}$, voxel coupling and intervoxel in-plane coupling effective conductivity values $\frac{ó_a^{coup} ó_b^{pri} + ó_b^{coup} ó_a^{pri}}{ó_a^{pri} + ó_b^{pri}} \approx \pm ⅕ ó_{exp}$, intervoxel principal effective conductivity values $ó_a^{pri,1} + ó_b^{pri,1} - \frac{½\left(ó_a^{coup} - ó_b^{coup}\right)^2}{ó_a^{pri,2} + ó_b^{pri,2}} \approx 2ó_{exp}$, and that intervoxel out-of-plane coupling effective conductivity values $ó_a^{coup,1} + ó_b^{coup,1} - \frac{½\left(ó_a^{coup,2} - ó_b^{coup,2}\right)\left(ó_a^{coup,3} - ó_b^{coup,3}\right)}{ó_a^{pri} + ó_b^{pri}} \approx \pm ⅖ ó_{exp}$. Thus,

$$
\begin{aligned}
\mathbf{v}^T\mathbf{A}\mathbf{v} \approx \sum_{i=1}^{N_n} \Bigg\{ & ó_{exp}\left\{\left(ø_{n_i} - ø_{n_i n_2}\right)^2 + \left(ø_{n_i} - ø_{n_i n_4}\right)^2 + \left(ø_{n_i} - ø_{n_i n_6}\right)^2\right\} \pm \\
& ⅖ ó_{exp}\left\{\begin{array}{l}
\left(ø_{n_i} - ø_{n_i n_2}\right)\left(ø_{n_i q_2} - ø_{n_i q_4}\right) + \left(ø_{n_i} - ø_{n_i n_4}\right)\left(ø_{n_i q_3} - ø_{n_i q_4}\right) + \\
\left(ø_{n_i} - ø_{n_i n_4}\right)\left(ø_{n_i r_2} - ø_{n_i r_4}\right) + \left(ø_{n_i} - ø_{n_i n_6}\right)\left(ø_{n_i r_5} - ø_{n_i r_4}\right) + \\
\left(ø_{n_i} - ø_{n_i n_2}\right)\left(ø_{n_i s_2} - ø_{n_i s_4}\right) + \left(ø_{n_i} - ø_{n_i n_6}\right)\left(ø_{n_i s_5} - ø_{n_i s_4}\right)
\end{array}\right\} + \\
& \sum_{i=1}^{N_q}\left\{2ó_{exp}\left\{\left(ø_{q_i} - ø_{q_i q_2}\right)^2 + \left(ø_{q_i} - ø_{q_i q_4}\right)^2\right\} \pm ⅕ ó_{exp}\left(ø_{q_i} - ø_{q_i q_4}\right)\left(ø_{q_i s_2} - ø_{q_i s_4}\right)\right\} + \\
& \sum_{i=1}^{N_r}\left\{2ó_{exp}\left\{\left(ø_{r_i} - ø_{r_i r_4}\right)^2 + \left(ø_{r_i} - ø_{r_i r_6}\right)^2\right\} \pm ⅕ ó_{exp}\left(ø_{r_i} - ø_{r_i r_6}\right)\left(ø_{r_i q_3} - ø_{r_i q_4}\right)\right\} + \\
& \sum_{i=1}^{N_s}\left\{2ó_{exp}\left\{\left(ø_{s_i} - ø_{s_i s_2}\right)^2 + \left(ø_{s_i} - ø_{s_i s_6}\right)^2\right\} \pm ⅕ ó_{exp}\left(ø_{s_i} - ø_{s_i s_2}\right)\left(ø_{s_i r_2} - ø_{s_i r_4}\right)\right\}.
\end{aligned}
\tag{A11}
$$

Allowing that potentials, $ψ$, could be uniform in $\mathbf{v}$, the differences of potential in (A11) are assigned an average magnitude of $Äø \geq 0$, giving

$$\mathbf{v}^T\mathbf{A}\mathbf{v} \approx N_n\left(3\delta_{exp}\Delta\omega^2 \pm 12/5\,\delta_{exp}\Delta\omega^2\right) + N_q\left(4\delta_{exp}\Delta\omega^2 \pm 4/5\,\delta_{exp}\Delta\omega^2\right) + N_r\left(4\delta_{exp}\Delta\omega^2 \pm 4/5\,\delta_{exp}\Delta\omega^2\right) + N_s\left(4\delta_{exp}\Delta\omega^2 \pm 4/5\,\delta_{exp}\Delta\omega^2\right) = \left\{N_n\left(3 \pm 2\,2/5\right) + \left(N_q + N_r + N_s\right)\left(4 \pm 4/5\right)\right\}\delta_{exp}\Delta\omega^2 \geq 0. \quad \text{(A12)}$$

Therefore **A** is positive semidefinite, and the system **Av** = **b** can be solved by iterative methods such as the CGM. As mentioned in Section II-D1, since **A** is semidefinite, the solution vector **v** will not be unique – it will depend on its initial estimate supplied to the solver program. If one is interested only in the node potential subvector $\mathbf{v}_n$ (as is the case when compiling a LFM), it is enough to know that $\mathbf{v}_n$ is subject to a uniform offset. A unique potential field can be obtained by subtracting a constant value from $\mathbf{v}_n$ such that the node representing the reference electrode has zero potential.

On the other hand, if positive definiteness is needed for the solution technique, and/or if unique internode potentials are required for analysis, it is necessary to examine the nature of rank deficiency in **A**, and how it can be rectified by deflation. Intuitively, the full potential vector, **v**, is made up of node, *xy* internode, *yz* internode, and *xz* internode potentials,

$$\mathbf{v} = \mathbf{v}_n \cup \mathbf{v}_q \cup \mathbf{v}_r \cup \mathbf{v}_s. \quad \text{(A13)}$$

It is easy from (A11) that when potentials are uniform across each subvector, that is,

$$\mathbf{v}_n = [c_n\, c_n \ldots c_n]^T, \mathbf{v}_q = [c_q\, c_q \ldots c_q]^T, \mathbf{v}_r = [c_r\, c_r \ldots c_r]^T, \mathbf{v}_s = [c_s\, c_s \ldots c_s]^T, \quad \text{(A14)}$$

then $\mathbf{v}^T\mathbf{A}\mathbf{v} = 0$ for some nonzero **v**. This observation suggests that **A** is rank deficient by at least 4. It is less obvious that the intervoxel subvectors, $\mathbf{v}_q$, $\mathbf{v}_r$, $\mathbf{v}_s$, can be further divided according to

$$\mathbf{v}_q = \bigcup_{i=1}^{d_z} \mathbf{v}_{q_i}, \quad \mathbf{v}_r = \bigcup_{i=1}^{d_x} \mathbf{v}_{r_i}, \quad \mathbf{v}_s = \bigcup_{i=1}^{d_y} \mathbf{v}_{s_i}. \quad \text{(A15)}$$

where d_z, d_x, and d_y are the number of *xy*, *yz*, and *xz* voxel planes in the model, respectively. (In other words, d_x is the width of the model in the *x* dimension, measured in number of voxels). If potentials are uniform over each $\mathbf{v}_{q_i}$, $\mathbf{v}_{r_i}$, and $\mathbf{v}_{s_i}$, then $\mathbf{v}^T\mathbf{A}\mathbf{v}$ is still zero.

Roughly explained, this is due to the fact that within each voxel plane exists a layer of intervoxels whose internode reference potential is independent from that of all other internodes. Current flow calculated through the intervoxel faces is constrained within the voxel plane, and any current that flows out of the plane through voxel faces does not directly depend on potential at those internodes (see. Figure 2-A5). Therefore, if $\mathbf{v}_{q_i}$ is a subset of the solution $\mathbf{v}$, then so is $\mathbf{v}_{q_i}$ plus any constant value. Since this is true for all $\mathbf{v}_{q_i}$, $\mathbf{v}_{r_i}$, and $\mathbf{v}_{s_i}$, as well as for $\mathbf{v}_n$, $\mathbf{A}$ is rank deficient by exactly $d_x + d_y + d_z + 1$.

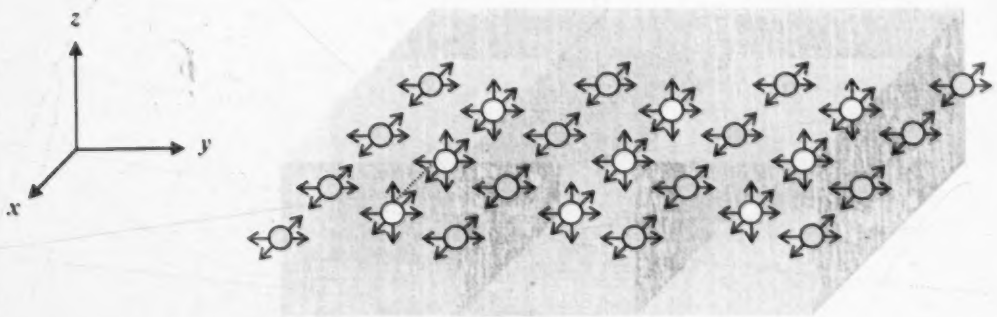

Figure 2-A5: An *xy* voxel plane where white circles represent nodes and grey circles represent *xy* internodes. Any flux through faces above or below (±*z*) the plane does not directly depend on the potentials of the internodes shown – only on node potentials and potentials of non-*xy* internodes that lie on the plane surface (not shown). Thus, the offset potential of this plane of internodes is independent from that of the nodes and all other internodes in the model.

Rigorous proof of this assertion is possible, but omitted here. However, the concept is clarified by redrafting (A11) with respect to the voxel plane solution subvectors (A15), and then forcing one potential value from each subvector to be zero (A17).

$$\mathbf{v}^{\mathrm{T}}\mathbf{A}\mathbf{v} \approx \sum_{i=1}^{N_n}\left\{\begin{array}{c} \acute{o}_{exp}\left\{\left(\varnothing_{n_i}-\varnothing_{n_in_2}\right)^2+\left(\varnothing_{n_i}-\varnothing_{n_in_4}\right)^2+\left(\varnothing_{n_i}-\varnothing_{n_in_6}\right)^2\right\}\pm \\ \tfrac{2}{5}\acute{o}_{exp}\left\{\begin{array}{l}\left(\varnothing_{n_i}-\varnothing_{n_in_2}\right)\left(\varnothing_{n_iq_2}-\varnothing_{n_iq_4}\right)+\left(\varnothing_{n_i}-\varnothing_{n_in_4}\right)\left(\varnothing_{n_iq_3}-\varnothing_{n_iq_4}\right)+\\ \left(\varnothing_{n_i}-\varnothing_{n_in_4}\right)\left(\varnothing_{n_ir_2}-\varnothing_{n_ir_4}\right)+\left(\varnothing_{n_i}-\varnothing_{n_in_6}\right)\left(\varnothing_{n_ir_3}-\varnothing_{n_ir_4}\right)+\\ \left(\varnothing_{n_i}-\varnothing_{n_in_2}\right)\left(\varnothing_{n_is_2}-\varnothing_{n_is_4}\right)+\left(\varnothing_{n_i}-\varnothing_{n_in_6}\right)\left(\varnothing_{n_is_3}-\varnothing_{n_is_4}\right)\end{array}\right\}+ \end{array}\right\}+$$

$$\sum_{i=1}^{d_z}\sum_{j=1}^{N_{qi}}\left\{2\acute{o}_{exp}\left\{\left(\varnothing_{q_{ij}}-\varnothing_{q_{ij}q_2}\right)^2+\left(\varnothing_{q_{ij}}-\varnothing_{q_{ij}q_4}\right)^2\right\}\pm\tfrac{4}{5}\acute{o}_{exp}\left(\varnothing_{q_{ij}}-\varnothing_{q_{ij}q_4}\right)\left(\varnothing_{q_{ij}s_2}-\varnothing_{q_{ij}s_4}\right)\right\}+ \quad \text{(A16)}$$

$$\sum_{i=1}^{d_x}\sum_{j=1}^{N_{ri}}\left\{2\acute{o}_{exp}\left\{\left(\varnothing_{r_{ij}}-\varnothing_{r_{ij}r_4}\right)^2+\left(\varnothing_{r_{ij}}-\varnothing_{r_{ij}r_6}\right)^2\right\}\pm\tfrac{4}{5}\acute{o}_{exp}\left(\varnothing_{r_{ij}}-\varnothing_{r_{ij}r_6}\right)\left(\varnothing_{r_{ij}q_3}-\varnothing_{r_{ij}q_4}\right)\right\}+$$

$$\sum_{i=1}^{d_y}\sum_{j=1}^{N_{si}}\left\{2\acute{o}_{exp}\left\{\left(\varnothing_{s_{ij}}-\varnothing_{s_{ij}s_2}\right)^2+\left(\varnothing_{s_{ij}}-\varnothing_{s_{ij}s_6}\right)^2\right\}\pm\tfrac{4}{5}\acute{o}_{exp}\left(\varnothing_{s_{ij}}-\varnothing_{s_{ij}s_2}\right)\left(\varnothing_{s_{ij}r_2}-\varnothing_{s_{ij}r_4}\right)\right\},$$

where N_{qi} is the number of *xy* internodes in the i^{th} *xy* plane, N_{ri} is the number of *yz* internodes in the i^{th} *yz* plane, and N_{si} is the number of *xz* internodes in the i^{th} *xz* plane. (The number of in-plane internodes will be just over double the number of voxels in a given plane.) Now, one potential value from each subvector is forced to be zero by removing nodes n_1 and internodes q_{i1}, r_{i1}, and s_{i1} from the potential vector **v**, as well as the corresponding rows and columns from **A**. The remaining potential vector and coefficient matrix are called $\mathbf{v}_d$ and $\mathbf{A}_d$, respectively.

$$\begin{aligned}
\mathbf{v}_{\mathrm{d}}^{\mathrm{T}}\mathbf{A}_{\mathrm{d}}\mathbf{v}_{\mathrm{d}} \approx{}& \acute{o}_{exp}\left(\varnothing^{2}_{n_1n_2}+\varnothing^{2}_{n_1n_4}+\varnothing^{2}_{n_1n_6}\right)\pm \tfrac{2}{5}\acute{o}_{exp}\begin{Bmatrix}\varnothing_{n_1n_2}\left(\varnothing_{n_1q_4}-\varnothing_{n_1q_2}\right)+\varnothing_{n_1n_4}\left(\varnothing_{n_1q_4}-\varnothing_{n_1q_5}\right)+\\ \varnothing_{n_1n_4}\left(\varnothing_{n_1r_4}-\varnothing_{n_1r_2}\right)+\varnothing_{n_1n_6}\left(\varnothing_{n_1r_4}-\varnothing_{n_1r_5}\right)+\\ \varnothing_{n_1n_2}\left(\varnothing_{n_1s_4}-\varnothing_{n_1s_2}\right)+\varnothing_{n_1n_6}\left(\varnothing_{n_1s_4}-\varnothing_{n_1s_5}\right)\end{Bmatrix}+\\
&\sum_{i=1}^{d_z}\left\{2\acute{o}_{exp}\left(\varnothing^{2}_{q_{i1}q_2}+\varnothing^{2}_{q_{i1}q_4}\right)\pm \tfrac{1}{5}\acute{o}_{exp}\varnothing_{q_{i1}q_4}\left(\varnothing_{q_{i1}s_4}-\varnothing_{q_{i1}s_2}\right)\right\}+\\
&\sum_{i=1}^{d_x}\left\{2\acute{o}_{exp}\left(\varnothing^{2}_{r_{i1}r_4}+\varnothing^{2}_{r_{i1}r_6}\right)\pm \tfrac{1}{5}\acute{o}_{exp}\varnothing_{r_{i1}r_6}\left(\varnothing_{r_{i1}q_4}-\varnothing_{r_{i1}q_3}\right)\right\}+\\
&\sum_{i=1}^{d_y}\left\{2\acute{o}_{exp}\left(\varnothing^{2}_{s_{i1}s_2}+\varnothing^{2}_{s_{i1}s_6}\right)\pm \tfrac{1}{5}\acute{o}_{exp}\varnothing_{s_{i1}s_2}\left(\varnothing_{s_{i1}r_4}-\varnothing_{s_{i1}r_2}\right)\right\}+\\
&\sum_{i=2}^{N_n}\begin{Bmatrix}\hat{o}_{exp}\left\{\left(\varnothing_{n_i}-\varnothing_{n_in_2}\right)^2+\left(\varnothing_{n_i}-\varnothing_{n_in_4}\right)^2+\left(\varnothing_{n_i}-\varnothing_{n_in_6}\right)^2\right\}\pm\\ \tfrac{2}{5}\acute{o}_{exp}\begin{Bmatrix}\left(\varnothing_{n_i}-\varnothing_{n_in_2}\right)\left(\varnothing_{n_iq_2}-\varnothing_{n_iq_4}\right)+\left(\varnothing_{n_i}-\varnothing_{n_in_4}\right)\left(\varnothing_{n_iq_3}-\varnothing_{n_iq_4}\right)+\\ \left(\varnothing_{n_i}-\varnothing_{n_in_4}\right)\left(\varnothing_{n_ir_2}-\varnothing_{n_ir_4}\right)+\left(\varnothing_{n_i}-\varnothing_{n_in_6}\right)\left(\varnothing_{n_ir_3}-\varnothing_{n_ir_4}\right)+\\ \left(\varnothing_{n_i}-\varnothing_{n_in_2}\right)\left(\varnothing_{n_is_2}-\varnothing_{n_is_4}\right)+\left(\varnothing_{n_i}-\varnothing_{n_in_6}\right)\left(\varnothing_{n_is_3}-\varnothing_{n_is_4}\right)\end{Bmatrix}\end{Bmatrix}+\\
&\sum_{i=1}^{d_z}\sum_{j=2}^{N_{qi}}\left\{2\acute{o}_{exp}\left\{\left(\varnothing_{q_{ij}}-\varnothing_{q_{ij}q_2}\right)^2+\left(\varnothing_{q_{ij}}-\varnothing_{q_{ij}q_4}\right)^2\right\}\pm \tfrac{1}{5}\acute{o}_{exp}\left(\varnothing_{q_{ij}}-\varnothing_{q_{ij}q_4}\right)\left(\varnothing_{q_{ij}s_2}-\varnothing_{q_{ij}s_4}\right)\right\}+\\
&\sum_{i=1}^{d_x}\sum_{j=2}^{N_{ri}}\left\{2\acute{o}_{exp}\left\{\left(\varnothing_{r_{ij}}-\varnothing_{r_{ij}r_4}\right)^2+\left(\varnothing_{r_{ij}}-\varnothing_{r_{ij}r_6}\right)^2\right\}\pm \tfrac{1}{5}\acute{o}_{exp}\left(\varnothing_{r_{ij}}-\varnothing_{r_{ij}r_6}\right)\left(\varnothing_{r_{ij}q_3}-\varnothing_{r_{ij}q_4}\right)\right\}+\\
&\sum_{i=1}^{d_y}\sum_{j=2}^{N_{si}}\left\{2\acute{o}_{exp}\left\{\left(\varnothing_{s_{ij}}-\varnothing_{s_{ij}s_2}\right)^2+\left(\varnothing_{s_{ij}}-\varnothing_{s_{ij}s_6}\right)^2\right\}\pm \tfrac{1}{5}\acute{o}_{exp}\left(\varnothing_{s_{ij}}-\varnothing_{s_{ij}s_2}\right)\left(\varnothing_{s_{ij}r_2}-\varnothing_{s_{ij}r_4}\right)\right\},
\end{aligned} \tag{A17}$$

The potential values in (A17) are assigned an average magnitude of ψ, and again, potential differences are $\Ä\varnothing$ giving,

$$\begin{aligned}
\mathbf{v}_{\mathrm{d}}^{\mathrm{T}}\mathbf{A}_{\mathrm{d}}\mathbf{v}_{\mathrm{d}} \approx{}& 3\acute{o}_{exp}\varnothing^{2}\pm \tfrac{12}{5}\acute{o}_{exp}\varnothing\Ä\varnothing+d_z\left(4\acute{o}_{exp}\varnothing^{2}\pm \tfrac{1}{5}\acute{o}_{exp}\varnothing\Ä\varnothing\right)+\\
&d_x\left(4\acute{o}_{exp}\varnothing^{2}\pm \tfrac{1}{5}\acute{o}_{exp}\varnothing\Ä\varnothing\right)+d_y\left(4\acute{o}_{exp}\varnothing^{2}\pm \tfrac{1}{5}\acute{o}_{exp}\varnothing\Ä\varnothing\right)+\\
&\left(N_n-1\right)\left(3\acute{o}_{exp}\Ä\varnothing^{2}\pm \tfrac{12}{5}\acute{o}_{exp}\Ä\varnothing^{2}\right)+\left(N_q-d_z\right)\left(4\acute{o}_{exp}\Ä\varnothing^{2}\pm \tfrac{1}{5}\acute{o}_{exp}\Ä\varnothing^{2}\right)+\\
&\left(N_r-d_x\right)\left(4\acute{o}_{exp}\Ä\varnothing^{2}\pm \tfrac{1}{5}\acute{o}_{exp}\Ä\varnothing^{2}\right)+\left(N_s-d_y\right)\left(4\acute{o}_{exp}\Ä\varnothing^{2}\pm \tfrac{1}{5}\acute{o}_{exp}\Ä\varnothing^{2}\right)=\\
&\left(3+4d_x+4d_y+4d_z\right)\acute{o}_{exp}\varnothing^{2}\pm\left(\tfrac{12}{5}+\tfrac{1}{5}d_x+\tfrac{1}{5}d_y+\tfrac{1}{5}d_z\right)\acute{o}_{exp}\varnothing\Ä\varnothing\\
&\left\{N_n\left(3\pm 2\tfrac{2}{5}\right)+\left(N_q+N_r+N_s-d_x-d_y-d_z\right)\left(4\pm \tfrac{1}{5}\right)\right\}\acute{o}_{exp}\Ä\varnothing^{2}>0.
\end{aligned} \tag{A18}$$

By inspection of (A18), even for a solution vector, $\mathbf{v}_{\mathrm{d}}$, in which potentials are uniform over each $\mathbf{v}_{q_i}$, $\mathbf{v}_{r_i}$, and $\mathbf{v}_{s_i}$, that is $\Ä\varnothing=0$, $\mathbf{v}_{\mathrm{d}}^{\mathrm{T}}\mathbf{A}_{\mathrm{d}}\mathbf{v}_{\mathrm{d}}>0$. Indeed, for any nonzero vector

$\mathbf{v}_d \in \mathbf{R}$, $\mathbf{v}_d^T \mathbf{A}_d \mathbf{v}_d > 0$. Therefore, the coefficient matrix, $\mathbf{A}_d$, is symmetric positive definite. It is now clear that deflation of $\mathbf{A}$ is performed by removing one node equation from the system, as well as one internode equation for every voxel plane in 3 dimensions.

The solution of the deflated system $\mathbf{A}_d\mathbf{v}_d = \mathbf{b}_d$ will be unique, and the potentials of the remaining (inter)nodes in each solution subvector will be relative to the designated potential of the deleted (inter)nodes. If it is required that these values be nonzero, then the following adjustment must be made to the deflated source vector prior to solution,

$$\mathbf{b}_d = \mathbf{b}_d' - a_n \mathbf{A}_{d,n} - \sum_{i=1}^{d_z} a_{q_i} \mathbf{A}_{d,q_i} - \sum_{i=1}^{d_x} a_{r_i} \mathbf{A}_{d,r_i} - \sum_{i=1}^{d_y} a_{s_i} \mathbf{A}_{d,s_i}, \qquad \text{(A19)}$$

where n, q_i, r_i, s_i are indices of the deleted (inter)nodes; a_n, a_{q_i}, a_{r_i}, a_{s_i} are the forced potentials of those; and $\mathbf{b}_d'$ is the original source vector with values corresponding to the deleted (inter)nodes removed.

Of course, the offset potential of any solution subvector can be adjusted after the fact by subtraction of a constant value. Although the deflation technique is not computationally intensive, iterative solution techniques that can handle positive semidefinite systems are recommended in order to avoid keeping track of internode types and the voxel planes in which they exist.

Appendix B: Vectorized EFVM Decomposition Algorithm Flowchart

Voxel locations in the 3D model grid are referenced by triplets of (x, y, z) subscripts, or equivalently by scalar indices ranging from 1 to **dx*dy*dz**. Each "non-air" voxel in the 3D model grid is assigned a unique node number (found in **Map**) that dictates its place in the system of equations. An expanded grid that reflects the staggered configuration of nodes and internodes is assigned (inter)node numbers (found in **XMap**) where the node numbers correspond to those in the regular grid (**Map**). (Inter)voxel locations in the expanded grid are referenced by subscripts or scalar indices ranging from 1 to **dxX*dyX*dzX**, where **dxX** is 2***dx**+1, likewise for **dyX** and **dzX**.

Like the isotropic FVM coefficient matrix [24], the coefficient matrix **A** is symmetric and elements on the main diagonal of **A** are just the negated sum of the *principal effective conductivity* coefficients in that row (or column). Thus, only elements in **A**'s upper triangle need be computed explicitly. This is accomplished by considering conductivities of adjacent (inter)voxels only in the positive x, y, and/or z directions relative to each (inter)node. In the case of node-internode and out-of-plane internode-internode relationships, symmetry of effective conductivity tensors is similarly exploited. Q, R, S variable names refer respectively to xy, xz, and yz internodes or intervoxels. Apart from the main algorithm, three matrix-filling subroutines are called repeatedly from flowchart blocks with vertical panels on the sides. The subroutine algorithms follow the main flowchart. All uses of the multiplication symbol * indicate array (not matrix) multiplication. Boxes with dotted outlines enclose comments on the algorithm.

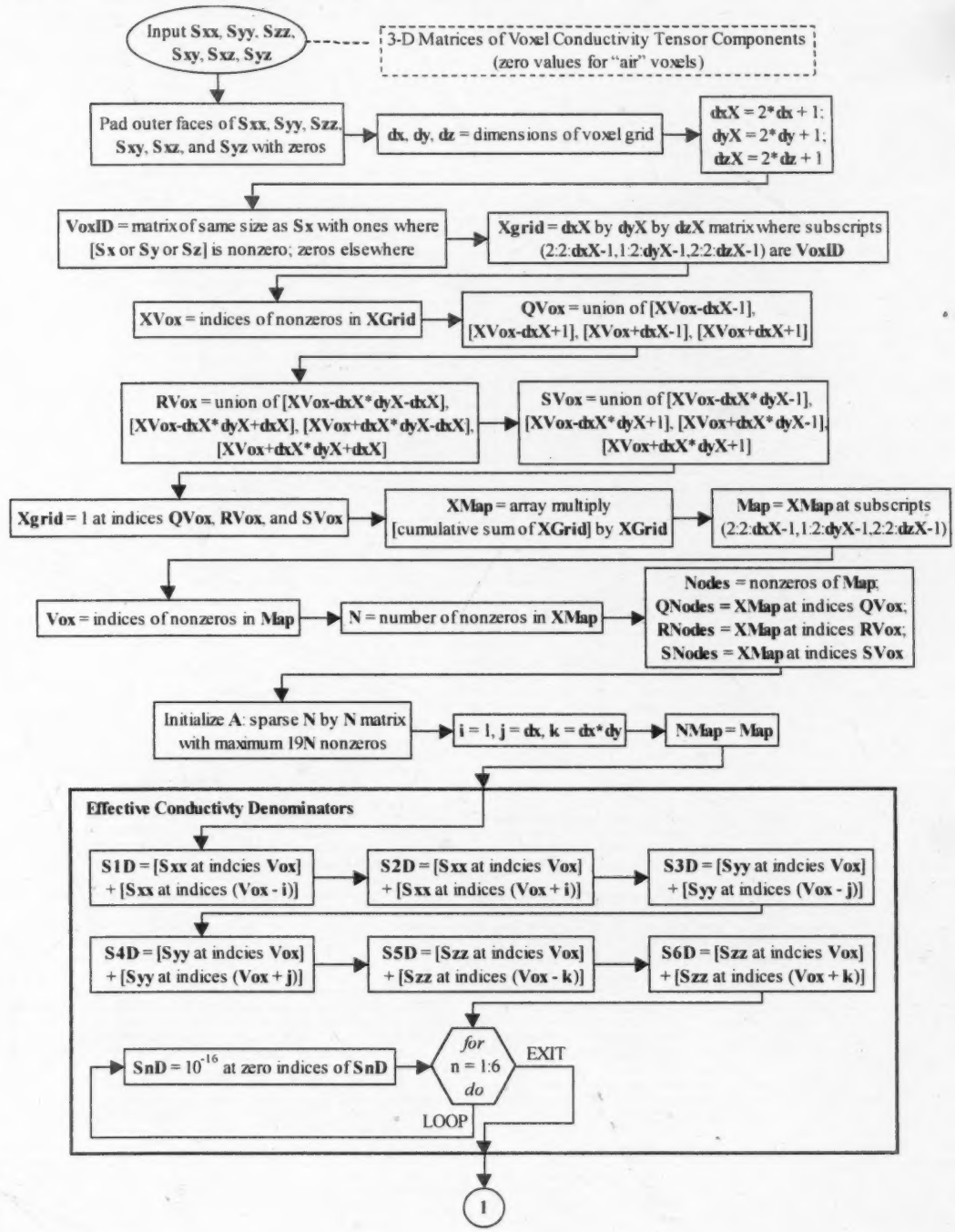
Input Sxx, Syy, Szz, Sxy, Sxz, Syz
3-D Matrices of Voxel Conductivity Tensor Components (zero values for "air" voxels)
Pad outer faces of Sxx, Syy, Szz, Sxy, Sxz, and Syz with zeros
dx, dy, dz = dimensions of voxel grid
dxX = 2*dx + 1; dyX = 2*dy + 1; dzX = 2*dz + 1
VoxID = matrix of same size as Sx with ones where [Sx or Sy or Sz] is nonzero; zeros elsewhere
Xgrid = dxX by dyX by dzX matrix where subscripts (2:2:dxX-1,1:2:dyX-1,2:2:dzX-1) are VoxID
XVox = indices of nonzeros in XGrid
QVox = union of [XVox-dxX-1], [XVox-dxX+1], [XVox+dxX-1], [XVox+dxX+1]
RVox = union of [XVox-dxX*dyX-dxX], [XVox-dxX*dyX+dxX], [XVox+dxX*dyX-dxX], [XVox+dxX*dyX+dxX]
SVox = union of [XVox-dxX*dyX-1], [XVox-dxX*dyX+1], [XVox+dxX*dyX-1], [XVox+dxX*dyX+1]
Xgrid = 1 at indices QVox, RVox, and SVox
XMap = array multiply [cumulative sum of XGrid] by XGrid
Map = XMap at subscripts (2:2:dxX-1,1:2:dyX-1,2:2:dzX-1)
Vox = indices of nonzeros in Map
N = number of nonzeros in XMap
Nodes = nonzeros of Map; QNodes = XMap at indices QVox; RNodes = XMap at indices RVox; SNodes = XMap at indices SVox
Initialize A: sparse N by N matrix with maximum 19N nonzeros
i = 1, j = dx, k = dx*dy
NMap = Map
Effective Conductivty Denominators
S1D = [Sxx at indcies Vox] + [Sxx at indices (Vox - i)]
S2D = [Sxx at indcies Vox] + [Sxx at indices (Vox + i)]
S3D = [Syy at indcies Vox] + [Syy at indices (Vox - j)]
S4D = [Syy at indcies Vox] + [Syy at indices (Vox + j)]
S5D = [Szz at indcies Vox] + [Szz at indices (Vox - k)]
S6D = [Szz at indcies Vox] + [Szz at indices (Vox + k)]
SnD = 10^-16 at zero indices of SnD
for n = 1:6 do
EXIT
LOOP
1

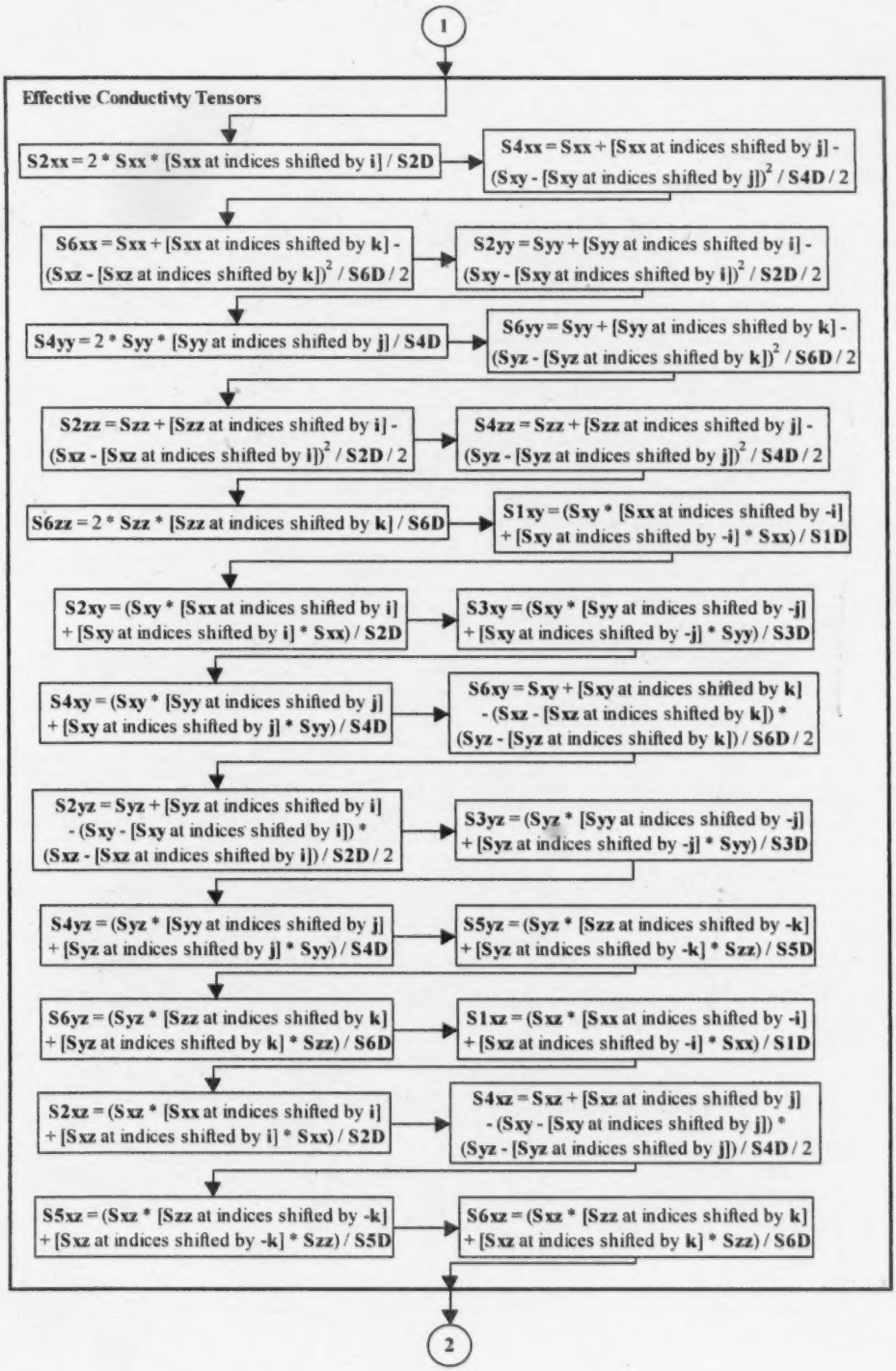
1
Effective Conductivty Tensors
S2xx = 2 * Sxx * [Sxx at indices shifted by i] / S2D
S4xx = Sxx + [Sxx at indices shifted by j] - (Sxy - [Sxy at indices shifted by j])^2 / S4D / 2
S6xx = Sxx + [Sxx at indices shifted by k] - (Sxz - [Sxz at indices shifted by k])^2 / S6D / 2
S2yy = Syy + [Syy at indices shifted by i] - (Sxy - [Sxy at indices shifted by i])^2 / S2D / 2
S4yy = 2 * Syy * [Syy at indices shifted by j] / S4D
S6yy = Syy + [Syy at indices shifted by k] - (Syz - [Syz at indices shifted by k])^2 / S6D / 2
S2zz = Szz + [Szz at indices shifted by i] - (Sxz - [Sxz at indices shifted by i])^2 / S2D / 2
S4zz = Szz + [Szz at indices shifted by j] - (Syz - [Syz at indices shifted by j])^2 / S4D / 2
S6zz = 2 * Szz * [Szz at indices shifted by k] / S6D
S1xy = (Sxy * [Sxx at indices shifted by -i] + [Sxy at indices shifted by -i] * Sxx) / S1D
S2xy = (Sxy * [Sxx at indices shifted by i] + [Sxy at indices shifted by i] * Sxx) / S2D
S3xy = (Sxy * [Syy at indices shifted by -j] + [Sxy at indices shifted by -j] * Syy) / S3D
S4xy = (Sxy * [Syy at indices shifted by j] + [Sxy at indices shifted by j] * Syy) / S4D
S6xy = Sxy + [Sxy at indices shifted by k] - (Sxz - [Sxz at indices shifted by k]) * (Syz - [Syz at indices shifted by k]) / S6D / 2
S2yz = Syz + [Syz at indices shifted by i] - (Sxy - [Sxy at indices shifted by i]) * (Sxz - [Sxz at indices shifted by i]) / S2D / 2
S3yz = (Syz * [Syy at indices shifted by -j] + [Syz at indices shifted by -j] * Syy) / S3D
S4yz = (Syz * [Syy at indices shifted by j] + [Syz at indices shifted by j] * Syy) / S4D
S5yz = (Syz * [Szz at indices shifted by -k] + [Syz at indices shifted by -k] * Szz) / S5D
S6yz = (Syz * [Szz at indices shifted by k] + [Syz at indices shifted by k] * Szz) / S6D
S1xz = (Sxz * [Sxx at indices shifted by -i] + [Sxz at indices shifted by -i] * Sxx) / S1D
S2xz = (Sxz * [Sxx at indices shifted by i] + [Sxz at indices shifted by i] * Sxx) / S2D
S4xz = Sxz + [Sxz at indices shifted by j] - (Sxy - [Sxy at indices shifted by j]) * (Syz - [Syz at indices shifted by j]) / S4D / 2
S5xz = (Sxz * [Szz at indices shifted by -k] + [Sxz at indices shifted by -k] * Szz) / S5D
S6xz = (Sxz * [Szz at indices shifted by k] + [Sxz at indices shifted by k] * Szz) / S6D
2

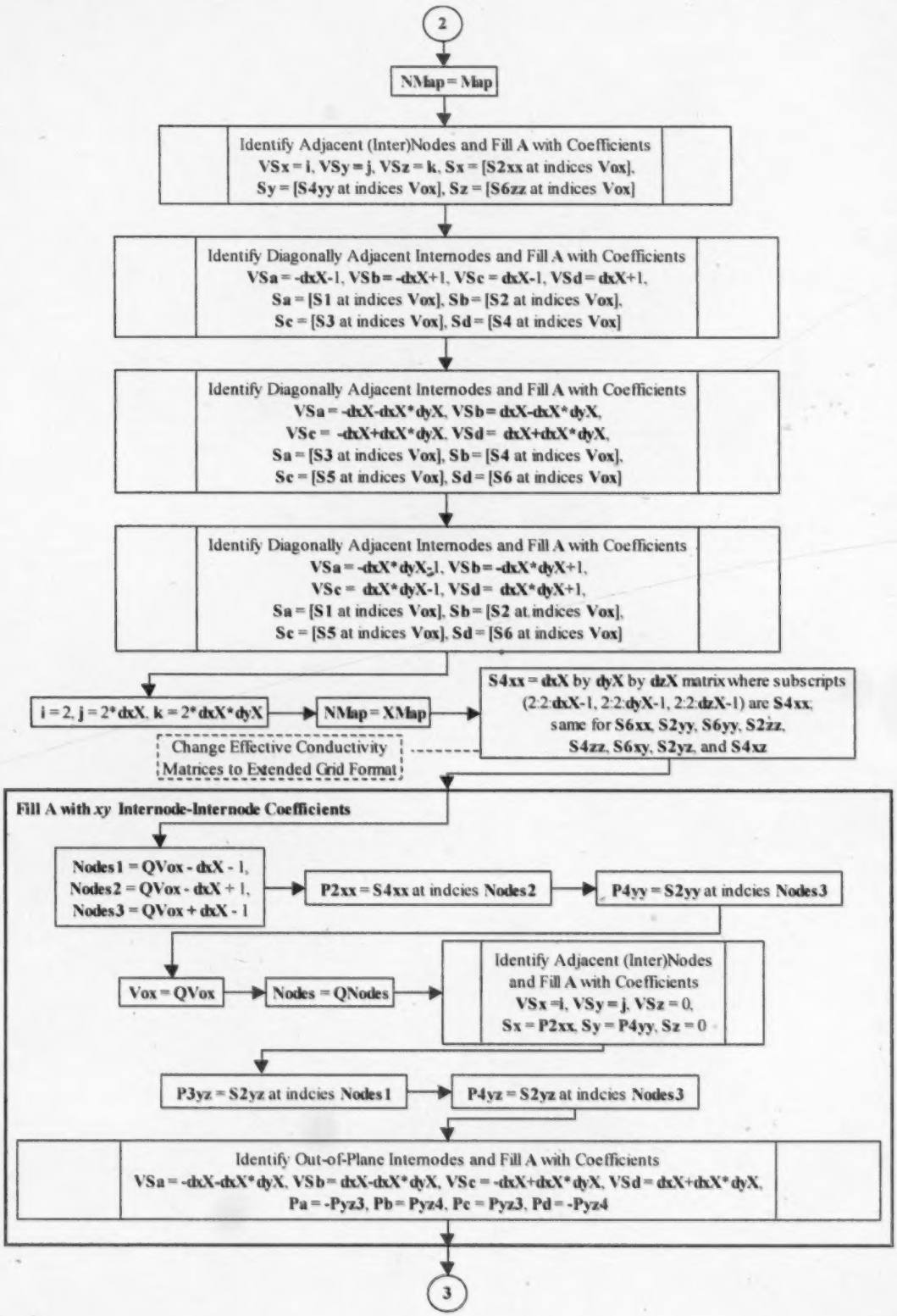
2
NMap = Map
Identify Adjacent (Inter)Nodes and Fill A with Coefficients
VSx = i, VSy = j, VSz = k, Sx = [S2xx at indices Vox],
Sy = [S4yy at indices Vox], Sz = [S6zz at indices Vox]
Identify Diagonally Adjacent Internodes and Fill A with Coefficients
VSa = -dxX-1, VSb = -dxX+1, VSc = dxX-1, VSd = dxX+1,
Sa = [S1 at indices Vox], Sb = [S2 at indices Vox],
Sc = [S3 at indices Vox], Sd = [S4 at indices Vox]
Identify Diagonally Adjacent Internodes and Fill A with Coefficients
VSa = -dxX-dxX*dyX, VSb = dxX-dxX*dyX,
VSc = -dxX+dxX*dyX, VSd = dxX+dxX*dyX,
Sa = [S3 at indices Vox], Sb = [S4 at indices Vox],
Sc = [S5 at indices Vox], Sd = [S6 at indices Vox]
Identify Diagonally Adjacent Internodes and Fill A with Coefficients
VSa = -dxX*dyX-1, VSb = -dxX*dyX+1,
VSc = dxX*dyX-1, VSd = dxX*dyX+1,
Sa = [S1 at indices Vox], Sb = [S2 at indices Vox],
Sc = [S5 at indices Vox], Sd = [S6 at indices Vox]
i = 2, j = 2*dxX, k = 2*dxX*dyX
NMap = XMap
S4xx = dxX by dyX by dzX matrix where subscripts
(2:2:dxX-1, 2:2:dyX-1, 2:2:dzX-1) are S4xx;
same for S6xx, S2yy, S6yy, S2zz,
S4zz, S6xy, S2yz, and S4xz
Change Effective Conductivity
Matrices to Extended Grid Format
Fill A with xy Internode-Internode Coefficients
Nodes1 = QVox - dxX - 1,
Nodes2 = QVox - dxX + 1,
Nodes3 = QVox + dxX - 1
P2xx = S4xx at indcies Nodes2
P4yy = S2yy at indcies Nodes3
Vox = QVox
Nodes = QNodes
Identify Adjacent (Inter)Nodes
and Fill A with Coefficients
VSx = i, VSy = j, VSz = 0,
Sx = P2xx, Sy = P4yy, Sz = 0
P3yz = S2yz at indcies Nodes1
P4yz = S2yz at indcies Nodes3
Identify Out-of-Plane Internodes and Fill A with Coefficients
VSa = -dxX-dxX*dyX, VSb = dxX-dxX*dyX, VSc = -dxX+dxX*dyX, VSd = dxX+dxX*dyX,
Pa = -Pyz3, Pb = Pyz4, Pc = Pyz3, Pd = -Pyz4
3

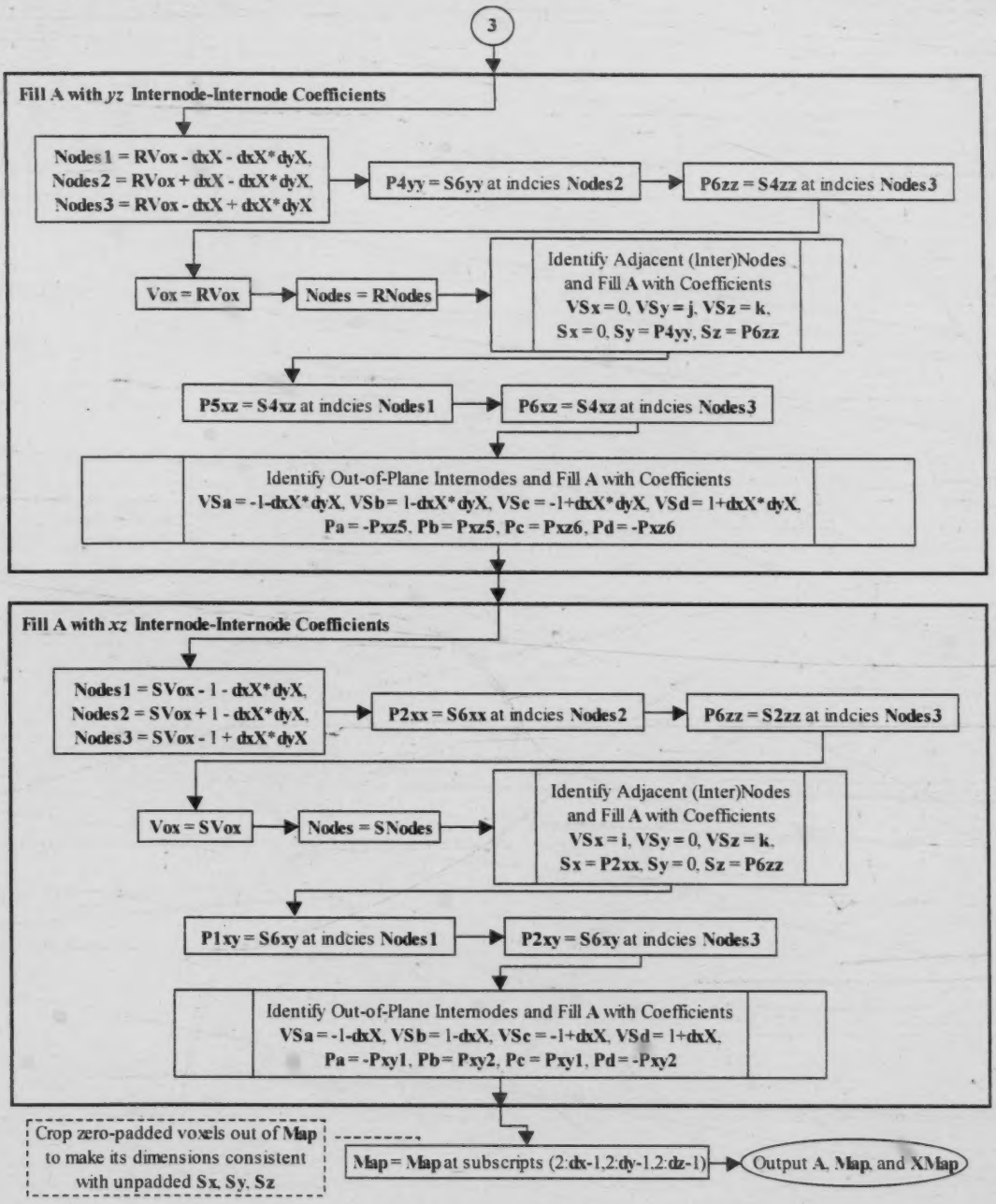
3
Fill A with yz Internode-Internode Coefficients
Nodes1 = RVox - dxX - dxX*dyX,
Nodes2 = RVox + dxX - dxX*dyX,
Nodes3 = RVox - dxX + dxX*dyX
P4yy = S6yy at indcies Nodes2
P6zz = S4zz at indcies Nodes3
Vox = RVox
Nodes = RNodes
Identify Adjacent (Inter)Nodes and Fill A with Coefficients
VSx = 0, VSy = j, VSz = k,
Sx = 0, Sy = P4yy, Sz = P6zz
P5xz = S4xz at indcies Nodes1
P6xz = S4xz at indcies Nodes3
Identify Out-of-Plane Internodes and Fill A with Coefficients
VSa = -1-dxX*dyX, VSb = 1-dxX*dyX, VSc = -1+dxX*dyX, VSd = 1+dxX*dyX,
Pa = -Pxz5, Pb = Pxz5, Pc = Pxz6, Pd = -Pxz6
Fill A with xz Internode-Internode Coefficients
Nodes1 = SVox - 1 - dxX*dyX,
Nodes2 = SVox + 1 - dxX*dyX,
Nodes3 = SVox - 1 + dxX*dyX
P2xx = S6xx at indcies Nodes2
P6zz = S2zz at indcies Nodes3
Vox = SVox
Nodes = SNodes
Identify Adjacent (Inter)Nodes and Fill A with Coefficients
VSx = i, VSy = 0, VSz = k,
Sx = P2xx, Sy = 0, Sz = P6zz
P1xy = S6xy at indcies Nodes1
P2xy = S6xy at indcies Nodes3
Identify Out-of-Plane Internodes and Fill A with Coefficients
VSa = -1-dxX, VSb = 1-dxX, VSc = -1+dxX, VSd = 1+dxX,
Pa = -Pxy1, Pb = Pxy2, Pc = Pxy1, Pd = -Pxy2
Crop zero-padded voxels out of Map to make its dimensions consistent with unpadded Sx, Sy, Sz
Map = Map at subscripts (2:dx-1,2:dy-1,2:dz-1)
Output A, Map, and XMap

Subroutines follow.

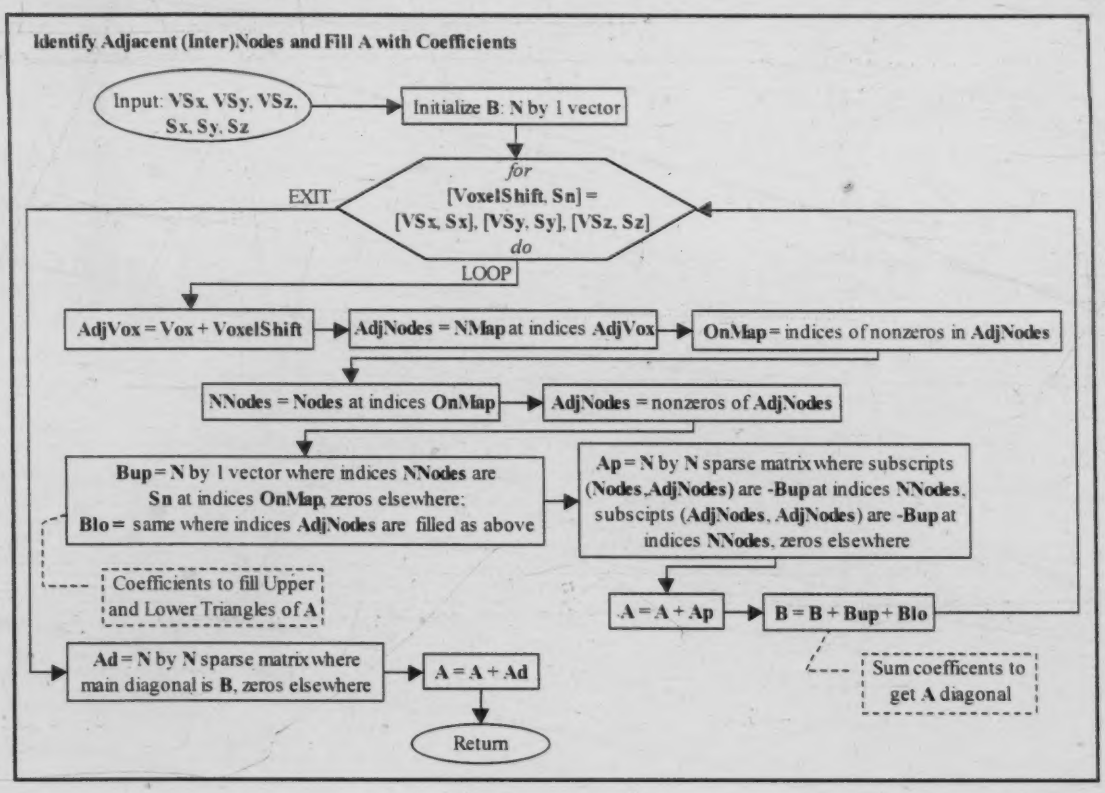
Identify Adjacent (Inter)Nodes and Fill A with Coefficients
Input: VSx, VSy, VSz, Sx, Sy, Sz
Initialize B: N by 1 vector
for [VoxelShift, Sn] = [VSx, Sx], [VSy, Sy], [VSz, Sz] do
EXIT
LOOP
AdjVox = Vox + VoxelShift
AdjNodes = NMap at indices AdjVox
OnMap = indices of nonzeros in AdjNodes
NNodes = Nodes at indices OnMap
AdjNodes = nonzeros of AdjNodes
Bup = N by 1 vector where indices NNodes are Sn at indices OnMap, zeros elsewhere;
Blo = same where indices AdjNodes are filled as above
Ap = N by N sparse matrix where subscripts (Nodes,AdjNodes) are -Bup at indices NNodes, subscipts (AdjNodes, AdjNodes) are -Bup at indices NNodes, zeros elsewhere
Coefficients to fill Upper and Lower Triangles of A
A = A + Ap
B = B + Bup + Blo
Sum coefficents to get A diagonal
Ad = N by N sparse matrix where main diagonal is B, zeros elsewhere
A = A + Ad
Return

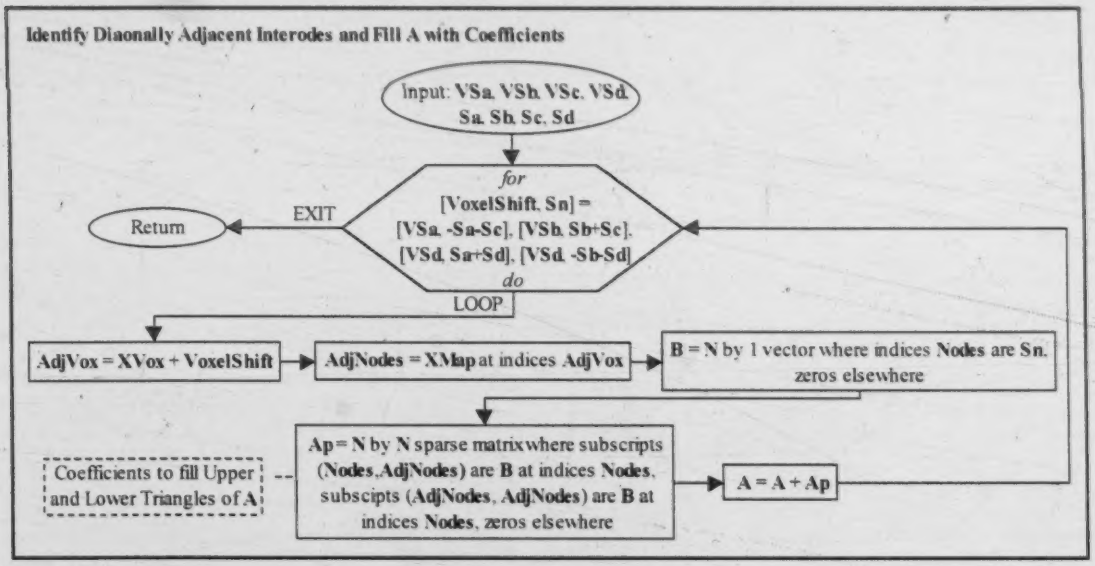
Identify Diaonally Adjacent Interodes and Fill A with Coefficients
Input: VSa, VSb, VSc, VSd, Sa, Sb, Sc, Sd
for [VoxelShift, Sn] = [VSa, -Sa-Sc], [VSb, Sb+Sc], [VSd, Sa+Sd], [VSd, -Sb-Sd] do
EXIT
Return
LOOP
AdjVox = XVox + VoxelShift
AdjNodes = XMap at indices AdjVox
B = N by 1 vector where indices Nodes are Sn, zeros elsewhere
Ap = N by N sparse matrix where subscripts (Nodes,AdjNodes) are B at indices Nodes, subscipts (AdjNodes, AdjNodes) are B at indices Nodes, zeros elsewhere
A = A + Ap
Coefficients to fill Upper and Lower Triangles of A

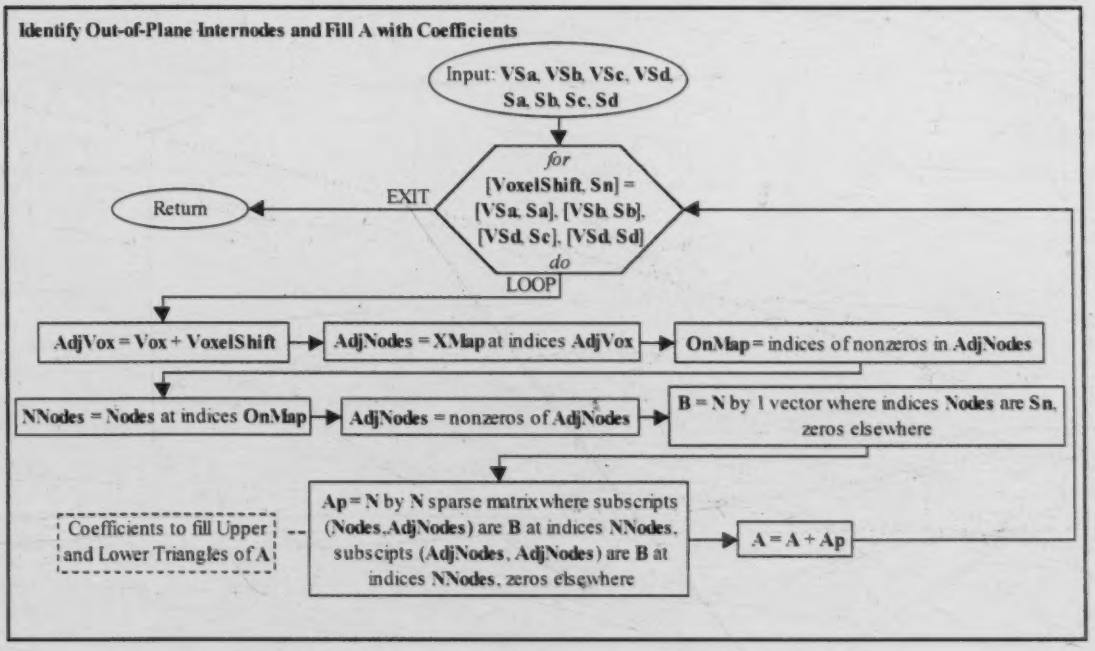
Identify Out-of-Plane Internodes and Fill A with Coefficients
Input: VSa, VSb, VSc, VSd, Sa, Sb, Sc, Sd
for [VoxelShift, Sn] = [VSa, Sa], [VSb, Sb], [VSd, Sc], [VSd, Sd] do
EXIT
Return
LOOP
AdjVox = Vox + VoxelShift
AdjNodes = XMap at indices AdjVox
OnMap = indices of nonzeros in AdjNodes
NNodes = Nodes at indices OnMap
AdjNodes = nonzeros of AdjNodes
B = N by 1 vector where indices Nodes are Sn, zeros elsewhere
Ap = N by N sparse matrix where subscripts (Nodes,AdjNodes) are B at indices NNodes, subscipts (AdjNodes, AdjNodes) are B at indices NNodes, zeros elsewhere
A = A + Ap
Coefficients to fill Upper and Lower Triangles of A

CHAPTER 3

ACCELERATED FORWARD SOLUTION BY CHEBYSHEV POLYNOMIAL PRECONDITIONING

I. Introduction

A. Volume Conductor Models

The earliest and most simple head models developed for EEG source localization were analytically-derived spherical volume conductors. These days, it is widely agreed that any spherical model is too simplistic to accurately locate epileptogenic foci [1]-[3]. Some work in fitting spherical surface potentials to a realistic head shape [4]-[7], or vice-versa [8] has been documented. These techniques are quite effective for localizing superficial sources, but less so for electrical activity originating deeper in the brain, or where the shape of the skull deviates most dramatically from the ideal sphere.

Increased accessibility of efficient and affordable computing has spawned a pursuit of more realistic, numerical head models. Analytical spherical models serve as a "gold standard" by which the performance of numerical volume conductor models may be assessed. The Finite Element Method (FEM) [9], [10] is a popular method of representing realistic head volumes. This technique models the entire volume with interconnected elements of various shapes and sizes. As such, this method accounts for many of the complexities omitted by analytical models and the Boundary Element Method (BEM) [11], [12] including tissue discontinuities, inhomogeneities, and anisotropy. It is therefore is a preferred model for EEG source localization [13], but setting up an optimal nonuniform volume grid can be a challenging task [13], [14].

B. Source Models

There is a strong physiological argument to support the assertion that equivalent current dipoles can adequately approximate the electric field produced by a region of active cortical cells [15], [16]. However, since complex combinations of cortical generators can emit overlapping signals and usually evolve over time, it may be necessary to develop more complicated source models to account for such cerebral activity. Spatiotemporal dipole source models have been investigated to this end [1]. Furthermore, spatiotemporal data can be exploited to null the effect of EEG background – uncorrelated noise – in single or multiple dipole source estimation algorithms by principal component analysis [17]-[20].

C. Finite Volume Method

The Finite Volume Method (FVM) is a numerical technique used to model current flow through an inhomogeneous medium by building a mathematical description of the volume as an assemblage of many equally sized discrete volume elements [14], [21]. Each hexahedron is assigned resistive properties based on those of the tissue it represents. This method is based on general curvilinear coordinates. In the present work, cubic voxels are framed in an isotropic Cartesian grid.

Since the voxels defined in this particular implementation of the FVM are strictly cubic, the discretized head model can be extracted directly from the pixels of medical images. Furthermore, the computational complications of a nonuniform grid are avoided by using very high finite volume resolution throughout the head, rather than doing mesh refinement at critical tissue interfaces, as is often necessary with the FEM. Thus the volume decomposition and formulation of equations is conceptually and mathematically

very simple [22], lending itself well to a robust, unsupervised algorithm for patient-specific head model development.

A FVM head model can account for patient-specific head shape and tissue discontinuities such as holes in the bone structure. This important flexibility offers maximal accuracy in source localization. The method was verified by comparison to the "gold standard" analytic equation for a 3-shelled sphere, with respect to calculated surface potentials [14], and single dipole localization [23]. There it was confirmed that the accuracy of the numerical method is improved by increasing the spatial resolution of the three-dimensional FVM volume grid. For spatial resolution of one millimeter, the head must be represented by millions of voxels, yielding an enormous set of data to be algebraically manipulated. This leads to significant challenges in terms of computation time and memory requirements. Integration of polynomial preconditioning with the Conjugate Gradient Method algorithm makes it possible to solve very large systems of finite difference equations so that the head model can be discretized into many more volume elements (better spatial resolution) than has been attempted in the past.

II. Methods

A. Model Preparation

For the purpose of simulating the flow of current from a source in the brain to electrodes on the scalp (the forward problem in EEG), the assemblage of discrete volume elements are modeled as a three-dimensional mesh circuit. Theoretical details and justification for this treatment is provided in [21]. Each cube is represented by a node, which is coupled to six adjacent nodes by a resistor (see Figure 3-1). The conductivity of

the connection between two neighbouring nodes (effective conductivity, $\acute{o}_{eff}$) is simply the series combination of the conductivities of the two adjacent half-voxels. That is, the nodes at the centres of voxels 0 and 1 are separated by the effective conductivity

$$\acute{o}_{eff1} = \frac{2\acute{o}_0\acute{o}_1}{\acute{o}_0 + \acute{o}_1}. \tag{1}$$

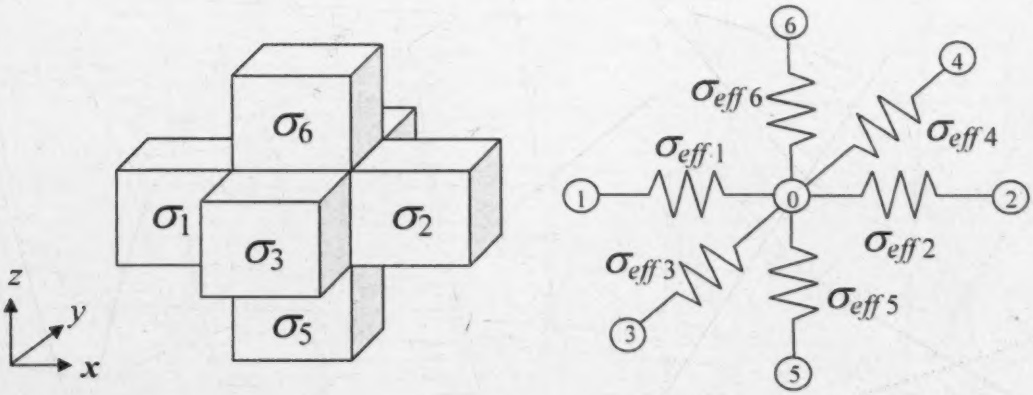

Figure 3-1: A set of adjacent voxels modeled as nodes in a 3D mesh circuit.

For the purposes of this study, the origin of an electrical signal in the brain is modeled as a single current dipole – a source and sink separated by one node. A relationship between any node and its six neighbours is expressed using Kirchoff's Current Law. The finite difference equation that describes the relationship amongst any set of seven adjacent nodes is

$$\begin{aligned} &\acute{o}_{eff1}(\varnothing_0 - \varnothing_1) + \acute{o}_{eff2}(\varnothing_0 - \varnothing_2) + \acute{o}_{eff3}(\varnothing_0 - \varnothing_3) + \\ &\acute{o}_{eff4}(\varnothing_0 - \varnothing_4) + \acute{o}_{eff5}(\varnothing_0 - \varnothing_5) + \acute{o}_{eff6}(\varnothing_0 - \varnothing_6) = \frac{I_0}{h}, \end{aligned} \tag{2}$$

where ψ_0 is the potential of the central node, ψ_n are the potentials of the adjacent nodes, σ_{effn} are the conductivities shared by the central node and each adjacent node (conductivity per unit length), I_0 is the total source current in the central voxel, and h is

the side length of every voxel. Note that I_0 is zero for every voxel except those where a current source or sink are located. Briefly explained, the factor h scales effective conductivities to account for voxel dimensions. This relationship is derived from Poisson's electrostatic equation as detailed in [23].

The difference equation (2) is applied to every node to create a system of equations governed by Ohm's Law,

$$\mathbf{A} \cdot \mathbf{v} = \mathbf{b}, \tag{3}$$

where **A** is the coefficient matrix, **v** is a column vector of the potentials at every node, and **b** is a column vector of current sources at each node. Note that **A** is a symmetric and sparse matrix with exactly seven nonzero elements per row. **b** is also a sparse vector – the only nonzero elements are due to the current source and sink specified for the particular forward problem. A mathematical examination of properties particular to the FVM linear system is available in [14].

B. Solving the Linear System

1) The Conjugate Gradient Method: The objective is to be able to solve the system of equations (3) by inverting its coefficient matrix,

$$\mathbf{v} = \mathbf{A}^{-1} \cdot \mathbf{b}. \tag{4}$$

Unfortunately, the matrix **A** is so large (could be millions by millions), that its inversion is an impossible task even for a modern computer with the fastest processors and the largest possible memory. The method selected for the solution of (3) is an iterative one known as the Conjugate Gradient Method (CGM). Its use is justified by the fact that the matrix **A** is sparse with exactly seven nonzero elements per row, symmetric and positive

semidefinite. Proof of these properties is provided in [14]. For a visual depiction of the matrix equation format see Figure 3-2.

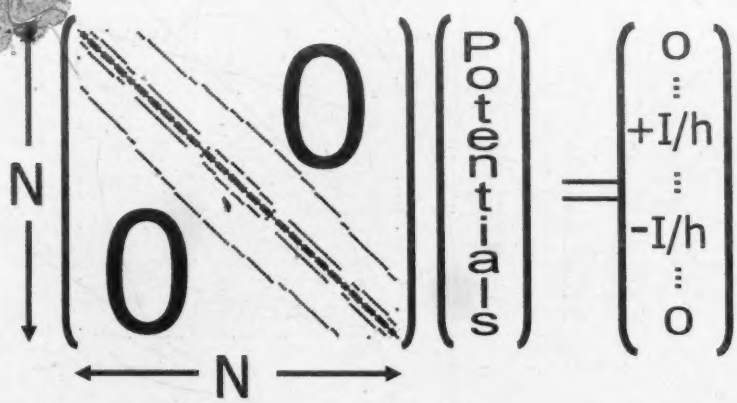

Figure 3-2: A visual depiction of the finite difference system of equations. N is the number of voxels in the head model.

The CGM is an iterative technique designed to achieve the solution result using a number of steps that is no more than the dimension of the matrix itself (actually, the number of distinct eigenvalues of the matrix [24]). In practice though, the number of iterations may not need to be so large. Iterations need to be carried out only until the mean squared difference between **A v** and the input vector **b** is less than some tolerance value å. That is,

$$\left\| \mathbf{A} \cdot \mathbf{v}_i - \mathbf{b} \right\|_2 < \varepsilon, \tag{5}$$

where $\mathbf{v}_i$ is the intermediate solution at iteration *i*. At every iteration, (5) is evaluated and once ε is sufficiently small, the iterated vector $\mathbf{v}_i$ is accepted as the approximation of the exact solution **v**, and the solver program is stopped. The exact form of the CGM pseudo-code is as follows:

Select the initial approximation $\mathbf{v}_0$, define the zeroth iteration vectors,

$$\mathbf{d}_0 = \mathbf{r}_0 = \mathbf{b} - \mathbf{A}\mathbf{v}_0 .$$

and follow the iterative procedure:

$$\acute{a}_i = \frac{\mathbf{r}_i^{\mathrm{T}}\mathbf{r}_i}{\mathbf{d}_i^{\mathrm{T}}\mathbf{A}\mathbf{d}_i}$$

$$\mathbf{v}_{i+1} = \mathbf{v}_i + \acute{a}_i\mathbf{d}_i$$

$$\mathbf{r}_{i+1} = \mathbf{r}_i - \acute{a}_i\mathbf{A}\mathbf{d}_i$$

$$\hat{a}_{i+1} = \frac{\mathbf{r}_{i+1}^{\mathrm{T}}\mathbf{r}_{i+1}}{\mathbf{r}_i^{\mathrm{T}}\mathbf{r}_i}$$

$$\mathbf{d}_{i+1} = \mathbf{r}_{i+1} + \hat{a}_{i+1}\mathbf{d}_i ,$$

where the superscript T indicates transposition.

The accumulation of round-off error causes the residuals $\mathbf{r}_i$ to gradually lose accuracy and, more importantly, the conjugate directions $\mathbf{d}_i$ to lose **A**-orthogonality. Whereas the former is somewhat benign, the latter reduces the iterative scheme to aimless wondering around the exact solution with a possibility of moving away from the exact solution. The error control (5) becomes of paramount importance as it provides an indication when the iterative process losses its effectiveness.

2) Matrix Deflation: **A** is positive semidefinite which means that the system of equations does not have a unique solution. Since **A** is rank deficient by 1, the CGM will converge to a solution vector that is offset by some constant value which depends on the initial solution estimate, $\mathbf{v}_0$, provided to the solver program [25]. This problem is easily overcome by arbitrarily assigning a reference value, a, to one of the potential variables, removing its row and column from **A**, and deleting the corresponding input and output variables from **v** and **b**, leaving a new system

$$\mathbf{A}_d \cdot \mathbf{v}_d = \mathbf{b}_d \,, \tag{6}$$

where

$$\mathbf{A}_d = \begin{bmatrix} A_{22} & \cdots & A_{2N} \\ \vdots & \ddots & \vdots \\ A_{N2} & \cdots & A_{NN} \end{bmatrix}, \tag{7}$$

and

$$\mathbf{v}_d = \begin{bmatrix} \phi_2 \\ \vdots \\ \phi_N \end{bmatrix}, \mathbf{b}_d = \begin{bmatrix} I_2 \\ \vdots \\ I_N \end{bmatrix} - a \begin{bmatrix} A_{21} \\ \vdots \\ A_{N1} \end{bmatrix}. \tag{8}$$

The deflated conductivity matrix $\mathbf{A}_d$ is positive definite and the remaining solution vector will be made up of values that are relative to the predefined reference value, a [14]. Recall, however, that the CGM is applicable to symmetric positive semidefinite systems [24], as well as those that are positive definite. Thus, matrix deflation is *not* strictly necessary for the solution method used in this work. Lack of uniqueness in the solution of the undeflated system (3) can be overcome by subtracting a constant value from the potential vector such that the reference node is grounded.

3) Preconditioning: One of the major parameters that influences the effectiveness of the CGM is the ratio of the largest eigenvalue of **A** to the smallest one, often referred to as the *condition number* of **A**. The closer the condition number is to one, the more quickly the iterative process converges. Since the condition number of the coefficient matrix plays such an important role in the efficiency of CGM, it is desirable to estimate it and, if needed, to improve it prior to or during the iterative process. The process of improving the condition number of a matrix is known as *preconditioning*. The main idea behind preconditioning is to replace the original system (3) with

$$\tilde{\mathbf{A}} \cdot \tilde{\mathbf{v}} = \tilde{\mathbf{b}}, \tag{9}$$

where the matrix $\tilde{\mathbf{A}} = \mathbf{C}_L \mathbf{A} \mathbf{C}_R$ has a better condition number than **A**. $\tilde{\mathbf{v}} = \mathbf{C}_R^{-1}\mathbf{v}$, $\tilde{\mathbf{b}} = \mathbf{C}_L \mathbf{b}$. $\mathbf{C}_L$ and $\mathbf{C}_R$ are two matrices known as left and right preconditioners, respectively.

The choice of preconditioner matrices gives rise to a number of possible methods, none of which is universal, and most have limited applicability. Two appear to be suitable to improve the condition of the extraordinarily large system (3): Jacobi preconditioning and polynomial preconditioning with Chebyshev polynomials.

a) Jacobi preconditioning: Jacobi preconditioning [26] is the simplest method by which one can improve the condition number of a matrix. The preconditioners are chosen to satisfy $\mathbf{C}_L = \mathbf{C}_R = \mathbf{J}$, where **J** is a diagonal matrix known as the Jacobi preconditioner and constructed according to

$$J_{kk} = \sqrt{\frac{1}{A_{kk}}} \quad . \tag{10}$$

It is easy to see that using the matrix, **J**, as both the left and right preconditioners, transforms the coefficient matrix **A** such that the main diagonal of $\tilde{\mathbf{A}} = \mathbf{JAJ}$ is all ones. The Gersgorin theorem [14] shows that Jacobi preconditioning therefore brings the spectral bounds (highest and lowest eigenvalues) of a FVM coefficient matrix into the interval [0, 2]. (Jacobi preconditioned eigenvalues of an anisotropic EFVM model [27] will have a slightly larger upper bound.) However, due to its limited power, Jacobi preconditioning is combined with the more sophisticated polynomial preconditioning (next section).

Jacobi preconditioning is especially convenient for the problem at hand because computing the diagonal matrix **J** and multiplying it by **A**, **b**, and $\tilde{\mathbf{v}}$ are rather inexpensive

operations computationally. Furthermore, since the symmetry of the system is preserved by this method, the CGM can be used directly to solve for $\tilde{\mathbf{v}}$, given $\tilde{\mathbf{A}}$ and $\tilde{\mathbf{b}} = \mathbf{Jb}$. That is, unlike unsymmetrical forms of preconditioning, Jacobi preconditioning does not need to be performed at each step of the iterative solution process to be compatible with the CGM [28]. Instead, $\tilde{\mathbf{A}}$ and $\tilde{\mathbf{b}}$ are computed in advance, and the final solution vector, $\mathbf{v} = \mathbf{J}\tilde{\mathbf{v}}$, is determined after convergence is achieved. These three simple steps implement the Jacobi preconditioner in its entirety, with exactly the same effect as preconditioning at every CGM iteration, but saving the computational expense of repeated application.

b) Polynomial preconditioning with Chebyshev Polynomials: This type of preconditioning consists of selecting the right preconditioner $\mathbf{C_R}$ to be the identity matrix and the left preconditioner

$$\mathbf{C_L} = \mathbf{A}^{-1}\left\{ \mathbf{I} - \left. T_m\left(\frac{(\lambda_{max} + \lambda_{min} - 2\mathbf{A})}{\lambda_{max} - \lambda_{min}}\right) \middle/ T_m\left(\frac{(\lambda_{max} + \lambda_{min})}{\lambda_{max} - \lambda_{min}}\right) \right\} = \sum_{j=0}^{m-1} \acute{a}_j \mathbf{A}^j, \qquad (11)$$

where $\mathbf{I}$ is the identity matrix, λ are the eigenvalues of $\mathbf{A}$, and T_m is the Chebyshev polynomial of a scalar or matrix variable η, given by the formula

$$T_m(\varsigma) = \frac{1}{2}\left\{\left(\varsigma + \sqrt{\varsigma^2 - 1}\right)^m + \left(\varsigma - \sqrt{\varsigma^2 - 1}\right)^m\right\}. \qquad (12)$$

This choice of $\mathbf{C_R}$ results in the solution vector not being affected by the preconditioning operation, i.e. $\tilde{\mathbf{v}} = \mathbf{v}$, only the efficiency of convergence is altered. The use of Chebyshev polynomials of the first kind [28] in $\mathbf{C_L}$ causes the eigenvalues of $\tilde{\mathbf{A}} = \mathbf{C_L(A)A}$ to be as tightly clustered about unity as possible. To clarify this assertion, see [30] and [31] which show that Chebyshev polynomials of the form (12) minimize the

uniform norm of the polynomial $\mathbf{I} - \mathbf{C}_L(\lambda)\lambda$ on the set $[\lambda_{min}, \lambda_{max}]$, the (estimated) spectrum of **A**.

The algorithm developed in [14] combines polynomial preconditioning with the CGM. Through this technique, $\mathbf{C}_L$ need not be calculated and stored prior to solution. Rather, the matrix polynomial coefficients are determined before solving by an alternative formula for $\mathbf{C}_L$, which does not require knowledge of $\mathbf{A}^{-1}$,

$$\mathbf{C}_L = \frac{2}{(\lambda_{max} - \lambda_{min}) T_m\left(\frac{\lambda_{max} + \lambda_{min}}{\lambda_{max} - \lambda_{min}}\right)} \sum_{n=1}^{m} t_n \sum_{k=0}^{n-1} \left(\frac{\lambda_{max} + \lambda_{min}}{\lambda_{max} - \lambda_{min}}\right)^{n-1-k} \times \sum_{j=0}^{k} (-1)^j \frac{k!}{(k-j)!\, j!} \frac{(\lambda_{max} + \lambda_{min})^j 2^{k-j}}{(\lambda_{max} - \lambda_{min})^k} \mathbf{A}^j = \sum_{n=0}^{m-1} \acute{a}_n \mathbf{A}^n, \tag{13}$$

where t_n are coefficients of the m^{th} order Chebyshev polynomial T_m (12). In practice, these coefficients are generated by the recursive formula

$$T_{n+1}(x) = 2xT_n(x) - T_{n-1}(x). \tag{14}$$

where

$$T_0(x) = 1, \quad T_1(x) = x. \tag{15}$$

To calculate the coefficients α_n by (13) only λ_{min}, λ_{max} and m need to be specified (see Section II-C below for information on selection of these parameters). That is, the matrix polynomial coefficients α_n are determined without manipulation of **A**.

During the CGM, $\mathbf{C}_L$ is applied to **A** "on the fly" through a number of additional matrix-vector multiplications and vector additions at each iteration. Where multiplication of $\widetilde{\mathbf{A}}$ by the vector $\mathbf{d}_i$ is required (see CGM iterative procedure in Section II-B1 above), the operation is performed without ever having explicitly carried out the multiplication $\widetilde{\mathbf{A}} = \mathbf{C}_L\mathbf{A}$. That is,

$$\tilde{\mathbf{A}} \cdot \mathbf{d}_i = \mathbf{C}_L \mathbf{A} \cdot \mathbf{d}_i = \alpha_0 \mathbf{A} \cdot \mathbf{d}_i + \alpha_1 \mathbf{A}^2 \cdot \mathbf{d}_i + \alpha_2 \mathbf{A}^3 \cdot \mathbf{d}_i + \alpha_3 \mathbf{A}^4 \cdot \mathbf{d}_i + \cdots . \quad (16)$$

Increasing powers of **A** become less and less sparse, requiring very large amounts of memory to store and manipulate. However, calculation of multiple powers of **A** can be avoided considering that

$$\mathbf{C}_L \mathbf{A} \cdot \mathbf{d}_i = \alpha_0 \mathbf{x}' + \alpha_1 \mathbf{x}'' + \alpha_2 \mathbf{x}''' + \alpha_3 \mathbf{x}'''' + \cdots . \quad (17)$$

where $\mathbf{x}^{(n)} = \mathbf{A}^n \cdot \mathbf{d}_i$ is a column vector that is generated recursively beginning with $\mathbf{x}' = \mathbf{A} \cdot \mathbf{d}_i$, $\mathbf{x}'' = \mathbf{A} \cdot \mathbf{x}'$, etc. In this way, polynomial preconditioning requires only *m* extra matrix-vector multiplications and vector additions per CGM iteration, where *m* is the order of $\tilde{\mathbf{A}} = \mathbf{C}_L \mathbf{A}$. This integrated technique for preconditioning within the CGM affords important computational savings, making it possible to apply polynomial preconditioning to the system of equations for a very high resolution FVM head model using an affordable amount of RAM and CPU time.

C. Timing and Optimization Experiments

The purpose of this work is to catalog timing results for solution of an FVM linear system of equations using Jacobi preconditioning and the Chebyshev polynomial preconditioned CGM, and to assess the benefits of both preconditioning techniques. Specifically, we are interested in monitoring the performance of the iterative solution method applied to the linear equations of a very high resolution realistic FVM head model. The conductor model with which experiments were performed was created using the National Library of Medicine's Visible Man CT data, which are of 1mm isotropic spatial resolution. The head is framed in a 181 by 217 by 181 grid, and its volume takes up 4,079,307 voxels. Voxels were identified as either bone or soft tissue and generalized

conductivities assigned to the tissue types were specified as $(3.5\ \Omega m)^{-1}$ for scalp/brain, and $(280\ \Omega m)^{-1}$ for bone. These values are typically used in three-shelled spherical models of the head [14], though references to differing conductivity parameters are also common. In order to illustrate how the size of an FVM model affects solution speed and parameter optimization, another lower resolution model was created for comparison by combining sets of 8 $(1\ mm)^3$ voxels into single $(2\ mm)^3$ voxels. This version of the realistic head model takes up 523,665 voxels in a 91 by 109 by 91 grid.

Head model decomposition was implemented using MATLAB. Vectorization techniques were applied widely throughout the code to avoid any programming loops that might be used for node-by-node computations, since loops executed by interpretive software platforms such as MATLAB are notoriously inefficient. Jacobi preconditioning and generation of the polynomial coefficients α_n, which are read as inputs to the solver program, are also generated using MATLAB. The highly vectorized program used in this research (see algorithm flowchart in [23]) can prepare the high resolution realistic head model (~4,000,000 voxels) for forward solution in about 6 minutes on the UltraSparc II 296 MHz processor with 1.2 GB RAM. The polynomial preconditioned CGM solver was programmed and compiled using C for increased computational and data input/output efficiency.

Previous work using the CGM to solve an FVM system of equations has shown that a tolerance value of $\varepsilon = 10^{-10}$ (5) or less gives minimum error when comparing potentials on the surface of a discretized inhomogeneous sphere to those calculated by a gold standard analytical model [14]. Therefore we assume that this convergence criterion will

provide a solution vector, **v**, of acceptable accuracy for the purposes of a FVM head model for EEG source localization.

1) Polynomial Degree: When preconditioning with Chebyshev polynomials, it is necessary to decide how far to expand the matrix polynomial $\mathbf{C}_L$. The greater its degree, m, the more effective preconditioning is, and the fewer CGM iterations required for convergence. Although a larger value of m tends to decrease the number of iterations, it also increases the amount of computational time per iteration. Thus, for every FVM head model there is an optimal degree of polynomial preconditioning which will afford maximal time savings. The approach taken to determine the best value of m for any model is empirical, but it is expected that general guidelines can be established to suggest a suitable choice of m for FVM systems of various sizes. Repetitive solution experiments were performed on both sizes of realistic FVM models to investigate how optimization of m with respect to total solution time relates to model size and the spectral bounds λ_{min} and λ_{max} specified in the computation of α_n (13).

Convergence of the iterative solution process depends somewhat on the properties of the source vector, **b**, assigned to the system. In most cases, **b** will have only two nonzero entries corresponding to the current source and sink of a single dipole. This is certainly true in a typical situation when using the FVM to compile a model-specific lead field matrix, where each solution is obtained for a source and sink placed at the leads of a single electrode pair [23]. The relative positions of the source and sink in the head model determine the distance between the two nonzero values in the vector **b**. Evaluations of solution speed with respect to various source/sink spreads indicated that the resulting variation in CGM iterations required for convergence is much less than that observed

between successive values of m. For simplicity, therefore, it was decided to run experiments with just one input vector, **b**, for each model size. A single z-oriented dipole was placed at the centre of the head to generate the source vector used in all trials.

2) Spectral Bound Parameters: The two parameters (other than m) required to calculate the appropriate polynomial coefficients, α_n, are the approximate spectral bounds of **A**, λ_{max} and λ_{min}. A precise measure of these values allows the condition number of $\tilde{\mathbf{A}} = \mathbf{C}_L\mathbf{A}$ to be minimized. However, it turns out that using the *exact* spectral bounds of **A** for λ_{max} and λ_{min} as does *not* minimize the number of iterations required for solution convergence. In fact, there is no definitive method to establish the optimal spectral parameters, but it is suggested that values somewhat inside the actual bounds are usually suitable [25]. Here again, several experiments were performed to investigate how optimization of the parameters λ_{max} and λ_{min} with respect to total solution time relates to model size and the degree of polynomial preconditioning, m.

3) To Deflate or Not to Deflate: We know that the polynomial preconditioned CGM can be applied to positive definite or semidefinite systems. Clearly, the deflated version of the FVM coefficient matrix, $\mathbf{A}_d$, is of better condition than **A**, since its singularity has been removed. Still, we would like to observe which form of the system can be solved the fastest given optimal preconditioning parameters. The system of equations for both the 1 and 2 mm resolution realistic head models were deflated, Jacobi preconditioned, and solved with optimal spectral bound parameters (determined in previous trials) and various degrees of polynomial preconditioning m. The amount of time required to reach convergence was recorded in each case and compared to the solve time of the undeflated equivalent system. Solutions obtained from undeflated processes were examined to

ensure uniqueness relative to a defined reference node potential.

All timing and optimization experiments were run on the UltraSparc II 296 MHz processor with 1.2 GB RAM.

III. Results

A. Jacobi Preconditioning

As mentioned in Section II-B3a, it can be shown that the eigenvalues of a Jacobi-preconditioned FVM coefficient matrix will always lie within the interval [0, 2]. For both sizes of the realistic FVM head model used in this work, application of Jacobi preconditioning brings the upper spectral bound of **A** from the order of 10^{-2} (depending on the magnitude of coefficients in the matrix) to exactly 2.0, as expected. Eigenvalues were estimated using the MATLAB built-in function 'eigs'. Since **A** is known to be positive semidefinite, and Jacobi preconditioning does not alter this property, we know that the lower spectral bound of $\tilde{\mathbf{A}} = \mathbf{JAJ}$ is zero. Thus, in the case of the singular FVM system, the condition number is not actually improved. Nevertheless, experiments were run in which the CGM solver routine (with polynomial preconditioning) was applied to the same FVM systems *with and without* the Jacobi preconditioning. These procedures confirmed that Jacobi preconditioning is of benefit when applied to both **A** and $\mathbf{A}_d$.

For the trials without Jacobi preconditioning, polynomial preconditioning spectral bound input parameters, λ_{max} and λ_{min}, were chosen empirically to yield the shortest solution time possible. For the 2 mm resolution model, these turned out to be λ_{max} = 0.0343 (actually the highest eigenvalue of **A** and $\mathbf{A}_d$) and $\lambda_{min} = 5\times10^{-5}$. With these parameter values, the iterative process typically required 1.25 times the number of

iterations than when Jacobi preconditioning was used with the same degree m, and spent the same amount of time (on average) per iteration. More iterations were required for $\lambda_{min} > 5\times10^{-5}$ and convergence was not achieved with $\lambda_{min} < 5\times10^{-5}$. This trend also held true when $\mathbf{A}$ was deflated and the experiment was performed on the positive definite system $\mathbf{A}_d \cdot \mathbf{v}_d = \mathbf{b}_d$.

B. Polynomial Preconditioning

1) Polynomial Degree: Figure 3-3 shows that, with the best choice of spectral bound parameters, the optimal degree of polynomial preconditioning is m = 10 (at 2 hours, 8 minutes solve time) for the high resolution head model and m = 9 (at 7 minutes, 57 seconds solve time) for the 2 mm resolution model. The graphs also show that, in both cases, there was not much variation in total solve time for degrees 8 through 10. This observation indicates that for any FVM model, a choice of m in that range will result in an iterative solution process that is more-or-less optimal. However, it should be noted that convergence was not achieved at degree 10 for the smallest λ_{min}, indicating that an appropriate choice of spectral bound parameters is of some importance, as discussed in the next section.

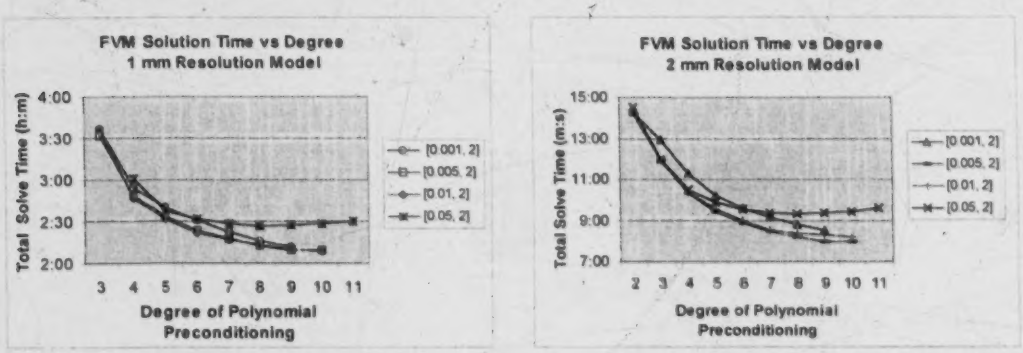

Figure 3-3: Total time to reach solution convergence for 1 and 2 mm resolution head models with various degrees (m) of polynomial preconditioning, and four different lower spectral bound input parameters (legends indicate [λ_{min}, λ_{max}]). Ends of each data line indicate that convergence was not achieved for higher or lower m.

Figure 3-4 shows that the number of iterations required for convergence decreases monotonically with m, as expected, although the savings effect is lessened with increasing degree. Iterations appear to be minimized around m = 10 or 11, where higher order polynomial preconditioning offers little or no improvement in CGM solution speed. The solution time spent per iteration is linearly related to m, and is approximately equal for all spectral bound parameters. This result makes sense because each term in the left preconditioner matrix, $\mathbf{C}_L$ (13), introduces one additional step in the CGM algorithm. The values of the polynomial coefficients, α_n, which depend on λ_{min} and λ_{max}, do not affect the time to implement preconditioning at each iteration.

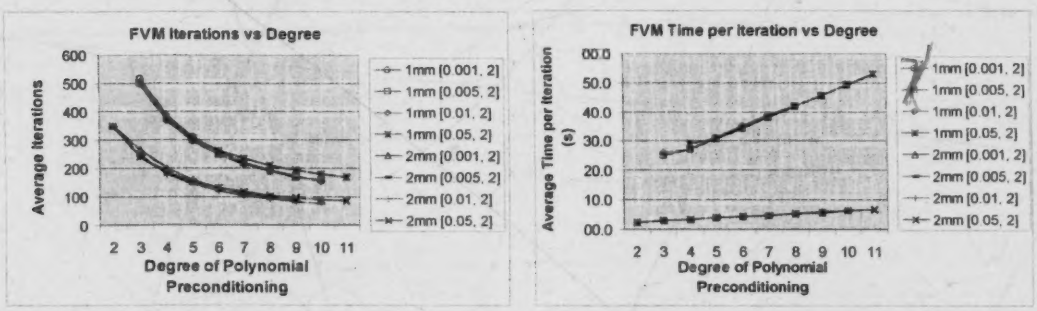

Figure 3-4: Number of iterations to reach solution convergence (left) and average time per iteration (right) for 1 and 2 mm resolution head models with various degrees (m) of polynomial preconditioning, and four different lower spectral bound input parameters (legends indicate *model* - [λ_{min}, λ_{max}]). Ends of each data line indicate that convergence was not achieved for higher or lower m.

2) Spectral Bound Parameters: As noted in Section III-A, the smallest eigenvalue of a FVM coefficient matrix after Jacobi preconditioning is known to be zero, while the largest is estimated at 2.0, in agreement with theory. To investigate the effect of spectral bound input parameters on polynomial preconditioned CGM execution time, the upper bound was first set as λ_{max} = 2.0, and the lower bound parameter was varied between 0.001, 0.005, 0.01, and 0.05. Figure 3-3 shows that for both model sizes, there is very little variation of total execution time over different values of λ_{min}, except when it is greater than 0.01. In the case that λ_{min} = 0.05, at higher degrees of polynomial preconditioning ($m > 7$), solution times are significantly longer than for $\lambda_{min} \leq 0.01$.

For the 1 mm resolution head model, λ_{min} = 0.01 gives the overall shortest time required for solution convergence (at m = 10), whereas λ_{min} = 0.005 results in the fastest solve time for the lower resolution model (at m = 9). As mentioned, however, for a given degree, m, there was very little variation in total solution time for $\lambda_{min} \leq 0.01$. Therefore, λ_{min} = 0.01 is a suitable choice of polynomial preconditioning input parameter

for solution of any FVM model, though a smaller value might be used to solve systems of much smaller dimension.

For the next trials, λ_{max} was adjusted keeping the lower spectral bound and m constant at optimal values (as determined above, independently for each system). λ_{max} was varied from 2.0 by increments of ±0.001 until a pattern of solve time versus λ_{max} was obtained. In the 1 mm resolution case, time required for solution was constant at 2 hours, 8 minutes for $1.999 \leq \lambda_{max} \leq 2.001$, and increased by about 2 minutes for λ_{max} on either side of that range. For the 2 mm resolution model, time required for solution was constant at 7 minutes, 57 seconds for $2.000 \leq \lambda_{max} \leq 2.003$, increased by about 6 minutes for λ_{max} = 1.999, and by about 3 minutes for λ_{max} = 2.004. In both models, the greater solve time was due to an increased in the number of required iterations. Time per iteration was constant.

Polynomial preconditioning is much less sensitive to the input parameters λ_{min} and m than it is to λ_{max}. That is because the parameter λ_{max} specifies the shape of $\mathbf{C}_L(\lambda)\lambda$ in the region of $\lambda = \lambda_{max}$. That is, it determines the effect polynomial preconditioning will have on the largest eigenvalues in the system. Fortunately, with Jacobi preconditioning we know without estimation that the upper spectral bound of $\tilde{\mathbf{A}} = \mathbf{JAJ}$ is 2.0 (or slightly less for systems of *very* small dimension). Thus, λ_{max} = 2.0 is clearly the best choice for Jacobi-preconditioned FVM systems.

3) To Deflate or Not to Deflate: The highest eigenvalue in a deflated FVM coefficient matrix, $\tilde{\mathbf{A}}_d = \mathbf{JA}_d\mathbf{J}$, is 2.0, as in the undeflated matrix $\tilde{\mathbf{A}} = \mathbf{JAJ}$. Unlike $\tilde{\mathbf{A}}$ however, the lowest eigenvalue of $\tilde{\mathbf{A}}_d$ is finite, though very small ($<10^{-6}$), and difficult to

estimate accurately. As discussed, precise knowledge of the lower spectral bound is unnecessary because λ_{max} and λ_{min} parameters provided to the polynomial preconditioned CGM that are optimal in terms of convergence time are not necessarily the *actual* spectral bounds of the system to be solved [25]. It was determined in the previous section that the best such parameters applied to $\tilde{\mathbf{A}}$ are $\lambda_{max} = 2.0$ and about $\lambda_{min} = 0.01$ and $\lambda_{min} = 0.005$, for the high and low resolution realistic FVM head models, respectively. Since the actual lower spectral bound of $\tilde{\mathbf{A}}_d$ is much smaller than 0.005, we assume that those are also a suitable parameters for solution of $\tilde{\mathbf{A}}_d \cdot \tilde{\mathbf{v}}_d = \tilde{\mathbf{b}}_d$. Given identical λ_{max} and λ_{min}, time required for solution convergence were compared for both sizes of deflated and undeflated models using various degrees of polynomial preconditioning, m.

Figure 3-5 shows the timing results for solution of deflated versus undeflated FVM systems. Interestingly, the results of this comparison were dramatically disparate for the two models of different size. In the 1 mm resolution case, deflation of the system matrix prior to Jacobi preconditioning offered a very slight solution speed improvement over its undeflated counterpart. For each value m, the number of iterations required to reach convergence were exactly the same, but time per iteration decreased by about 1 second per iteration. It is questionable whether or not the solution time savings (3 minutes, at best) gained by deflation would be lost during the pre-processing operations that are necessary to implement matrix deflation.

For solution of the 2 mm model system of equations, deflation caused the iterative process to take significantly *more* time to solve (5 minutes at best, over 7 minutes longer at worst). The deflated system consistently required 58% more iterations to reach convergence, at 0.1 to 0.2 more seconds per iteration. It is assumed that deflation could

yield a marginal saving of execution time (similar to the high resolution model) if the polynomial preconditioning parameters were carefully optimized for the new spectral properties of the deflated system.

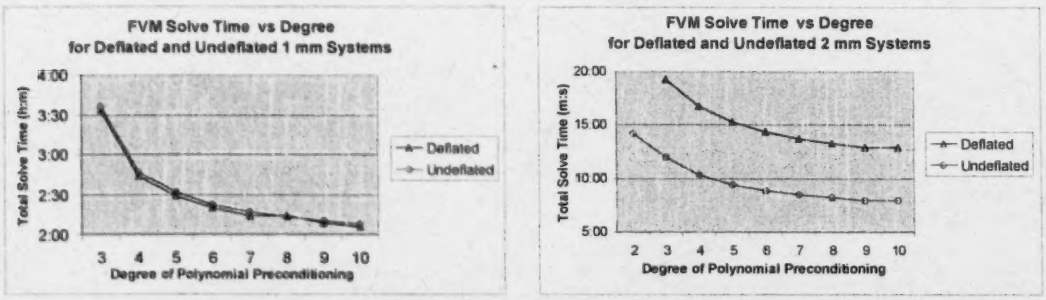

Figure 3-5: Total time to reach solution convergence for deflated and undeflated systems of 1 and 2 mm resolution head models with various degrees (m) of polynomial preconditioning. Left: $[\lambda_{min}, \lambda_{max}] = [0.01, 2]$. Right: $[\lambda_{min}, \lambda_{max}] = [0.005, 2]$. Ends of each data line indicate that convergence was not achieved for higher or lower m.

A solution vector $\tilde{\mathbf{v}}$ obtained from solving the singular system $\tilde{\mathbf{A}} \cdot \tilde{\mathbf{v}} = \tilde{\mathbf{b}}$ was adjusted to account for Jacobi preconditioning, $\mathbf{v} = \mathbf{J}\tilde{\mathbf{v}}$. Then a constant value was subtracted from all of $\mathbf{v}$ such that the potential of the reference node (the node removed from the deflated matrix $\tilde{\mathbf{A}}_d$) was zero. A solution vector $\tilde{\mathbf{v}}_d$ calculated by solution of the deflated system $\tilde{\mathbf{A}}_d \cdot \tilde{\mathbf{v}}_d = \tilde{\mathbf{b}}_d$ was also adjusted for Jacobi, $\mathbf{v}_d = \mathbf{J}\tilde{\mathbf{v}}_d$. To verify that the solution of the undeflated system is reliable, the non-reference values of $\mathbf{v}$ were compared to $\mathbf{v}_d$ and found to be identical within 2.0×10^{-4}% in the 1 mm resolution model, and 1.5×10^{-6}% for the 2 mm resolution head (L_1 norms). Thus it was proved that deflation of an FVM system of equation is not necessary for solution by the CGM.

IV. Discussion

In other work [23] it was shown that an accurate computer model for EEG source localization can be implemented based on the Finite Volume Method (FVM), using lead field analysis to solve the inverse problem in EEG. Localization experiments performed using a very high resolution FVM demonstrate that applied to a realistic head volume, it is an excellent candidate for use in clinical EEG source localization.

Preconditioning with Chebyshev polynomials during the Conjugate Gradient Method iterative solution algorithm is readily applicable to the FVM linear system of equations. Based on the results presented in this work, we confirm that Jacobi preconditioning decreases the number of iterations required by the polynomial preconditioned CGM for solution of an FVM system of equations by a factor of 1.25, for a numerical model of this particular conductivity distribution. In the 1 mm resolution (4,079,307 voxel) case, that translates to a savings of about 30 minutes per forward solution. Any FVM system of equations (of considerable dimension) that has been treated with Jacobi preconditioning has spectral properties that allow the universal application of the parameters $[\lambda_{min}, \lambda_{max}] = [0.01, 2.0]$ and $m = 9$ for close-to-optimal polynomial preconditioning. Conveniently, the spectral bounds of the linear system need not be estimated, whereas *without* Jacobi preconditioning, the spectral properties of a system are subject to coefficient magnitudes, matrix dimensions, etc., and are difficult to estimate. Therefore, in any attempt to solve the FVM systems (3) or (6) by polynomial preconditioned CGM, the method should be supplemented with Jacobi (or some similar form of) preconditioning.

It seems that deflation of the positive semidefinite FVM system of equations is a significant detriment to the efficiency of the iterative solution process in the case of

models with about 500,000 voxels. However, it is possible that re-optimization of polynomial preconditioning parameters for the new spectral properties of the deflated system could rectify the negative effect so that deflation may offer a marginal savings in solution time. For similar systems of about 4 million variables, matrix deflation is of no real benefit (or harm) in terms of iterative solution speed and re-optimization is not an issue.

V. Conclusions

The results given in this report are intended to demonstrate the utility of Jacobi preconditioning, polynomial preconditioning and the Conjugate Gradient Method to successfully solve a FVM system of linear equations for application to the problem of EEG source localization. Specifically, it was shown that one can effectively implement such a model with very high spatial resolution using an interpretive software platform such as MATLAB. With thorough vectorization of the decomposition algorithm, a realistic head model (>4,000,000 voxels) can be prepared for forward solution in about 6 minutes on the UltraSparc II 296 MHz processor with 1.2 GB RAM. The solver program was coded in C and optimization of the polynomial preconditioning technique was explored to accelerate convergence of the solution as much as possible.

Using the methods described here and in [23], it is possible to build a complete lead field matrix (LFM), which provides all the necessary data for any voxel-based source localization algorithm, in a clinically acceptable time frame. The overall clock time required for this source localization method can be further decreased using parallel computing [32]. Generation of the LFM is a repetitive process where a forward solution

is calculated for each electrode lead using a single system coefficient matrix. The forward solutions could easily be obtained simultaneously by distributing the equations to an array of parallel processors. This would allow source localization results to be available for patients within half a day from the time medical images of the patient's head are acquired. Once the LFM is compiled, the speed of source localization will depend entirely on the inverse algorithm used [23].

References

[1] J. S. Ebersole, "Defining epileptogenic foci: past, present, and future," J. Clin. Neurophysiol., vol. 14, pp. 470-83, Nov. 1997.

[2] B. J. Roth, M. Balish, A. Gorbach, and S. Sato, "How well does a three-sphere model predict positions of dipoles in a realistically shaped head?", Electroencephalogr. Clin. Neurophysiol., vol. 87, pp. 175-84, Oct. 1993.

[3] B. N. Cuffin, D. L. Schomer, J. R. Ives, and H. Blume, "Experimental tests of EEG source localization accuracy in spherical head models," Clin. Neurophysiol., vol. 112, pp. 46-51, Jan. 2001.

[4] M. Hämäläinen, "Anatomical correlates for magnetoencephalography: integration with magnetic resonance images," Clin. Phys. Physiol. Meas., vol. 12 (Suppl. A), pp. 29-32, 1991.

[5] V. L. Towle, R. Cakmur, Y. Cao, M. Brigell, and L. Parmeggiani, "Locating VEP equivalent dipoles in magnetic resonance images," Int. J. Neurosci., vol. 80, pp. 105-16, 1995.

[6] T. Krings, K. H. Chiappa, B. N. Cuffin, J. I. Cochius, S. Connolly, and G. R. Cosgrove, "Accuracy of EEG dipole source localization using implanted sources in the human brain," Clin. Neurophysiol., vol. 110:106, pp. 106-14, Jan. 1999.

[7] R. J. Sclabassi, M. Sonmez, and M. Sun, "EEG source localization: a neural network approach," Neurol. Res., vol. 23, pp. 457-64, July 2001.

[8] L. Spinelli, S. G. Andino, G. Lantz, M. Seeck, and C. M. Michel, "Electromagnetic inverse solutions in anatomically constrained spherical head models," Brain Topogr., vol. 13, pp. 115-25, Winter 2000.

[9] C. M. Phillips, "Source estimation in EEG – combining anatomical and functional constraints," Sc.A.D thesis, Faculté des Sciences Appliquées, Université de Liège – Liège, 2001.

[10] K. A. Awada, D. R. Jackson, J. T. Williams, D. R. Wilton, S. B. Baumann, and A. C. Papanicolaou, "Computational aspects of finite element modeling in EEG source localization," IEEE Trans. Biomed. Eng., vol. 44, pp. 736-52, Aug. 1997.

[11] B. N. Cuffin, D. L. Schomer, J. R. Ives, and H. Blume, "Experimental tests of EEG source localization accuracy in realistically shaped head models," Clin. Neurophysiol., vol. 112, pp. 2288-92, Dec. 2001.

[12] M. Fuchs, M. Wagner, and J. Kastner, "Boundary element method volume conductor models for source reconstruction," Clin. Neurophysiol., vol. 112, pp. 1400-7, Aug. 2001.

[13] H. Buchner, G. Knoll, M. Fuchs, A. Rienäcker, R. Beckmann, M. Wagner, J. Silny, and J. Pesch, "Inverse localization of electric dipole current sources in finite element models of the human head," Electroencephalogr. Clin. Neurophysiol., vol. 102, pp. 267-78, Apr. 1997.

[14] V. E. Agapov, "Numerical solution of the forward problem in electroencephalography," Ph.D. thesis, Department of Mathematical Sciences, University of Alberta – Edmonton, 2001.

[15] J. S. Ebersole, "Noninvasive localization of epileptogenic foci by EEG source modeling," Epilepsia, vol. 41 (Suppl. 3), pp. S24-S33, 2000.

[16] P. H. Schimpf, C. Ramon, and J. Haueisen, "Dipole models for the EEG and MEG," IEEE Trans. Biomed. Eng., vol. 49, pp. 409-18, May 2002.

[17] Z. J. Koles, J. C. Lind, and A. C. K. Soong, "Spatio-tempral decomposition of the EEG: a general approach to the isolation and localization of sources," Electroencephalogr. Clin. Neurophysiol., vol. 95, pp. 219-30, Oct. 1995.

[18] Z. J. Koles and A. C. K. Soong, "EEG source localization: implementing the spatio-temporal decomposition approach," Electroencephalogr. Clin. Neurophysiol., vol. 107, pp. 343-52, Nov. 1998.

[19] C. Uhl, F. Kruggle, B. Opitz, and D. Yves von Cramon, "A new concept of EEG/MEG signal analysis: detection of interacting spatial modes," Hum. Brain Mapp., vol. 6, pp. 137-49, 1998.

[20] H. M. Huizenga, J. C. de Munck, L. J. Waldorp, and R. P. Grasman, "Spatiotemporal EEG/MEG source analysis based on a parametric noise covariance model," IEEE Trans. Biomed. Eng., vol. 49, pp. 533-9, June 2002.

[21] M. Rosenfeld, R. Tanami, and S. Abboud, "Numerical solution of the potential due to sources in volume conductors with arbitrary geometry and conductivity," IEEE Trans. Biomed. Eng., vol. 43, pp. 679-89, July 1996.

[22] L. Lemieux, A. McBride, and J. W. Hand, "Calculation of electrical potentials on the surface of a realistic head model by finite differences," Phys. Med. Biol., vol. 41, pp. 1079-91, July 1996.

[23] L. A. Neilson, Z. J. Koles, "The finite volume head model for EEG source localization," University of Alberta – Edmonton, 2002.

[24] J. R. Shewchuk, *An Introduction to the Conjugate Gradient Method Without the Agonizing Pain.* School of Computer Science, Carnegie Mellon University – Pittsburgh, 1994. http://www-2.cs.cmu.edu/~jrs/jrspapers.html

[25] Y. Saad, *Iterative Methods for Sparse Linear Systems*. Boston, MA: PWS-Kent., 1996.

[26] A. M. Bruaset, *A survey of preconditioned iterative methods*. Longman Scientific & Technical, 1995.

[27] L. A. Neilson, "Anisotropic Expansion of the Finite Volume Method - Application of Diffusion Tensor Imaging to Realistic Head Modeling for EEG Source Localization," University of Alberta – Edmonton, 2003.

[28] R. Barrett, M. Berry, T. F. Chan, J. Demmel, J. Donato, J. Dongarra, V. Eijkhout, R. Pozo, C. Romine, and H. Van der Vorst, *Templates for the Solution of Linear Systems: Building Blocks for Iterative Methods*, 2nd ed. Philadelphia, PA: SIAM, 1994.

[29] P. L. Chebyshev, *Collected Works,* pp. 23-5. Moscow-Leningrad, 1947.

[30] S. F. Ashby, "Minimax polynomial preconditioning for Hermitian linear systems," SIAM J. Matrix Anal., vol. 12, pp. 766-89, 1991.

[31] E. K. Blum, *Numerical Analysis. Theory and Practice*. Addison-Wesley, 1972.

[32] S. Abboud, Y. Eshel, S. Levy, and M. Rosenfeld, "Numerical calculation of the potential distribution due to dipole sources in a spherical model of the head, "Comput. Biomed. Res., vol. 27, pp. 441-55, Dec. 1994.

SUMMARY

The FVM approach to the forward problem in EEG can accommodate realistic head geometry, as well as tissue discontinuities and inhomogeneity. Any type of inverse solution with focal or distributed source configurations can be applied to the resulting lead field data by modeling equivalent current dipoles, or volume current densities. Single dipole localization experiments were performed on an inhomogeneous (3-shelled) spherical conductor model, verifying the accuracy of the FVM modeling technique. It was also demonstrated that, under ideal conditions, models of higher spatial resolution allow for better source estimation. Results were obtained for several dipole sources located at regular intervals along three Cartesian axes in both radial and tangential orientations. One standard electrode configuration consisting of 25 leads was used for the analysis. The less-refined finite volume model (1.84 mm resolution, based on a 92 mm spherical head radius) achieved average displacement accuracy of 2.35 (0.00 – 4.11) mm. The highly discretized model (0.92 mm resolution) achieved an average displacement accuracy of 1.03 (0.00 – 3.32) mm. Similar dipole estimation techniques were applied to a realistic FVM head model, verifying that head geometry has a significant effect on the accuracy of source localization. Experiments performed demonstrated that, applied to a realistic head volume, the FVM is an excellent candidate for use in clinical EEG source localization.

The FVM volume conductor model was extended to incorporate generalized tissue anisotropy. The expanded system of linear equations is symmetric, so the reciprocal nature of the FVM input-output relationship is preserved, but many extra variables are required to account for conductivity tensors at each voxel. The anisotropic model was

verified against a known analytic solution to Laplace's equation with excellent agreement, less than 0.08% maximum error for a homogeneous volume, and less than 0.16% for an inhomogeneous volume.

Diffusion weighted MRI is used to quantify voxel-based diffusion tensors, which can be approximately linearly related to conductivity tensors of each voxel in a patient-specific head model. Single dipole source estimation experiments were performed on two-dimensional head models generated using diffusion tensor data acquired from a human subject. An anisotropic head model (the control model) was created using the available conductivity tensor data. A second isotropic version of the conductor model was generated using the tensor trace (average of the eigenvalues of each tensor) as the conductivity at every voxel. A third isotropic model was built by tissue-type segmentation, assigning characteristic conductivities to the tissue groups. The average difference in conductivity values between the two non-segmented models (magnitude of principal direction versus trace) was approximately 10% for gray matter voxels, and 30% for white matter.

Simulated EEG measurements were generated by placing 24 dipole current sources at cortical locations throughout the axial head slice. L_2 error norms of the scalp potential vectors induced in the isotropic models (with respect to the control model) averaged over the 24 sources were 10% (trace model) and 23% (segmented model). The simulated potentials from the scalp of the anisotropic conductor were used to localize those dipole sources within the simplified isotropic head models. The average displacement error of the estimated dipoles were 4.9 mm (trace model) and 7.7 mm (segmented model).

A very high resolution realistic FVM model of the human head was implemented to examine various computational aspects of solving of large, sparse linear systems of equations. Along with Jacobi preconditioning, an integrated algorithm that combines polynomial preconditioning with the Conjugate Gradient Method (CGM) makes it possible to solve the forward problem relatively quickly. Optimization of polynomial preconditioning input parameters was explored in detail. Given the best such parameters, a linear system of equations for a 2 mm resolution realistic head model (523,665 variables) was solved in about 8 minutes. A highly discretized model (1 mm resolution) has a system of 4,079,307 equations that is solvable in about 2 hours, using UltraSparc II 296 MHz processor with 1.2 GB RAM. Specifics of the fastest solver arrangement and optimal parameters were found to be conveniently universal for any size of FVM model. With the benefit of this solution method, clinical application of FVM modeling method is possible in a reasonable amount of time.